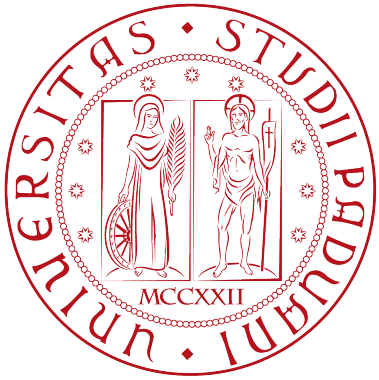

Università degli Studi di Padova

Dipartimento di Fisica e Astronomia
"Galileo Galilei"

Corso di Laurea Magistrale in Astronomia

Analysis of the Balmer Emission along the Quasar Main Sequence

Laureando:
Alan Andrés García López

Relatore:
Prof. Mauro D'Onofrio
Correlatore:
Dr.ssa Paola Marziani

Anno accademico 2016/2017

Contents

Acknowledgements

To my parents, Gustavo and Maria, for their unconditional support through all my life, specially in the difficult moments.

To Paola, for all the support over my whole stay in Padova and for her patient and kindness whenever she was guiding me along this research project.

Foreword

In this thesis we devoted the first four chapters to present a review of the concepts behind the spectra we have analyzed. This first chapter is an introduction to the quasar phenomenology: we describe briefly how we can observe quasars and AGNs with different electromagnetic windows and how astronomical surveys provide us with large samples of quasars.

Then, we proceed (Chapter 2) with a short overview of 4-dimensional eigenvector 1 (4DE1) parameter space and its optical plane which help us to organize quasars using the broad line spectral characteristics and select certain particular objects inside the optical plane for particular objectives, for example, using quasars as standard candles (Chapter 3).

Chapter 4 is a brief description of the line profiles used to model the broad lines in our spectra. The last two chapters (5, 6) are the core of this thesis because we show the spectral analysis of the Hβ emission across the whole optical plane of 4DE1 in a systematic way, and we mean systematic as building and fitting composite spectra of ΔFWHM(Hβ) = 1000 km s^{-1}. For the fifth chapter, we employed the models to reaffirm the abrupt change in profile at FWHM (Hβ) = 4000 km s^{-1} , between Population A / B quasars. Finally, in the sixth chapter, we employed the FWHM(Hβ) of highly accreting quasars as virial broadening estimator to determine the bolometric luminosity and found out that the composite spectra constructed by a higher number of quasars have a luminosity in agreement with the one observed and computed employing concordance cosmology. Chapter 7 summarizes the results, and Chapter 8 (as an Appendix) provides Figures with the full analysis.

Chapter 1

Introduction

1.1 The discovery of quasars

At the end of the fifties, the 3C and 3CR radio surveys were released. Many of the identified radio sources could be associated to nearby optical galaxies but others were coincident with "stellar like" optical sources. At that time, these sources represented a mystery due to their complex optical spectra different from the stellar ones. They were called "quasi-stellar radio sources", expression where the acronym quasars comes from.

In 1963, two milestones for the discovery of quasars occurred. Thomas Matthews and Allan Sandage identified the object 3C48 as a point source that showed an optical spectrum consisting of a blue continuum and strong, broad emission lines that could not be assigned to any atomic transition. More importantly, in the case of 3C273, Martin Schmidt could solve the unidentified lines problem by matching lines of the Balmer series at an "extremely high" redshift of $z = 0.158$. By the Hubble law, this implied a distance around 500 Mpc and a luminosity 100 times greater than normal galaxies. Nowadays, many quasars have been identified up to redshift $z = 7.085$ (or 12.9 billion years ago, when the Universe was 0.77 billions years old, Mortlock et al. 2011 using a variety of techniques across the electromagnetic spectrum.

Even though the discovery of quasars was made by radio observations, it was found very soon that the majority of quasars do not present strong radio emission, this means they are radio-quiet quasars. Radio-quiet (RQ) quasars were identified on the basis of a color-color (U-B, B-V) diagram where their locus is bluer than the one of stars (Sandage 1965) . Several UV excess surveys, such as the Bright Quasar Survey (BQS), were carried

out after the realization that 90% of the quasars are radio-quiet (Katgert et al. 1973). These surveys identified objects which appeared brighter in the U band than in the B band.

Based on a color-color criteria to identify quasars, the Sloan Digital Sky Survey employs the CCD technology and a dedicated 2.5-meter wide-field telescope to cover 14,555 square degrees on the sky. The SDSS system is a color-color system based on five photometric bands u (0.35μm), g (0.48μm), r (0.62μm), i (0.76μm) and z (0.91μm). In this case, the quasar candidates are all the objects that lie significantly off the stellar locus in multicolor phase. The spectrum of high redshift quasars gets redder and the quasars colors resembles the colors of stars. For that reason, a five color system is needed in place of a two color system. This method has a completeness to a level of 90 percent and it has allowed us to discover more than a 300,000 AGN. (Pâris et al. 2017).

1.2 Spectral energy distribution (SED)

Quasars, and specially the radio loud ones, were described as following a power law in the form $S_\nu \propto \nu^{-\alpha}$ with $\alpha = 1$ where α is the spectral index. However, the quasar SED differs markedly over smaller frequency ranges. See Figure 1 for an illustration of the SED in a frequency range of $10^9 - 10^{20}$ Hz.

As it can be seen in Figure 1, the continuum spectrum shows an increase towards UV wavelengths up to the limit of observable wavelengths, $\lambda \sim 1000$ Å. This spectral feature is known as the big blue bump (BBB). At wavelengths $\lambda \leq 912$ Å, photoelectric absorption by neutral hydrogen in the interstellar medium of the galaxy sets in, so that the Milky Way is opaque for this radiation. Only at considerably higher frequencies the extragalactic sky become observable again.

The UV and optical continuum are produced by the thermal emission of the accretion disk: the radial temperature profile of the virialized disk produces a broad spectrum with its maximum in the UV for typical black hole mass of $10^8 M_\odot$ (Peterson 1997).

The X-ray spectrum in the 2-20 keV range is characterized by the power law with mean slope $\alpha \sim 1$. There is a trend that the slope is somewhat steeper for radio-quiet quasar and flatter for radio-loud ones. The X-ray emission extends up to energies of $\sim$ 100 KeV, beyond which there is a spectral cut-off for RQ quasars. If we consider in more detail energies larger than 2 KeV, the spectrum usually shows a very simple power law shape with

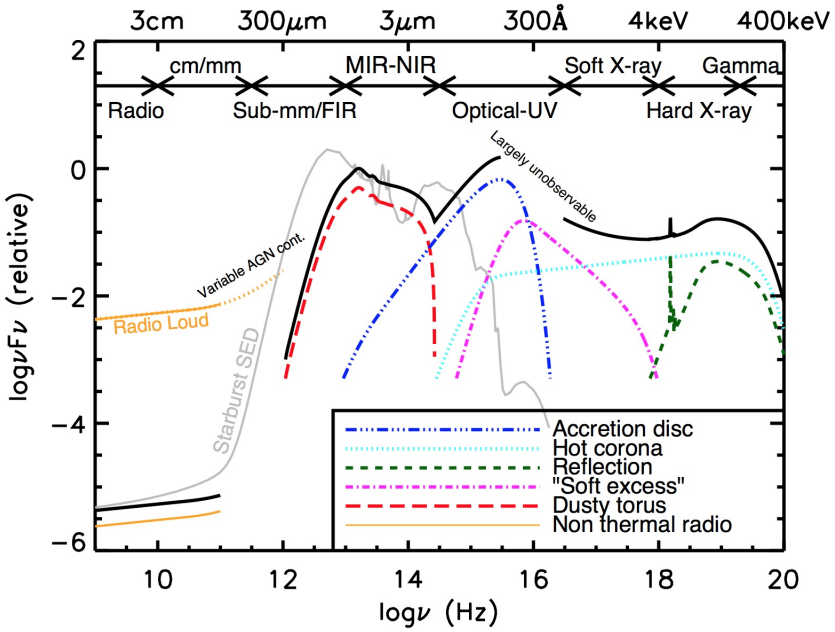

Figure 1: A schematic representation of an AGN SED based on the observed SEDs of radio-quiet quasars. The black solid curve represents the total SED and the various coloured curves represent the individual components. The primary emission from the AGN accretion disk peaks in the UV region. Radio-loud AGN have radio emission that can be several orders of magnitude higher than radio-quiet AGN (shown with the labelled orange line). Also shown is an example radio-UV SED of a starburst galaxy. (http://astro.dur.ac.uk/ cpnc25/research.html)

$\alpha \sim 0.7$. At lower energies (0.1-2 keV) the spectral flux can be higher than predicted by the extrapolation of the 2-20 keV power law. This could be interpreted as an additional source of X-ray emission, the soft X-ray excess, producing a power-law component at lower energies, probably due to the optically thick part of the X-ray emitting corona. It may be possible that the thermal emission of the innermost region of the disk is visible in the form of the soft X-ray excess (Done et al. 2012).

The continuum spectrum in X-rays is subdivided in a soft excess, a power law and a Compton hump, as it is illustrated in Figure 1. The gas in the corona is so dilute that it cannot cool efficiently and its temperature is much higher than that of the disk in order to maintain the virial equilibrium. Blackbody photons from the accretion disk propagate through the corona and may scatter off the hot electron distribution. Then, there is an inverse Compton process that increases the energy of the photons from the disk which ultimately produce the power law. The Compton hump comes from the scattering of photons of the corona towards the disk. The high energy photons are scattered down since the energy of electrons is very low in comparison with the corona. An important feature

that results from this scattering is the 6.4 keV iron line. The Compton hump and the Fe Kα line are visible in Figure 1.

At the limit between the optical and infrared spectrum (1μm) there is a minimum of emission where the features from the hot accretion disk and the cooler dust meet, see figure 2. The SED rises to a maximum in the mid-infrared associated to thermal emission of warm dust, at temperatures between T = 1100 – 1700 K, which are typical values of dust sublimation temperature for most astrophysical grain compositions (Landt et al. 2011). The corresponding source component, as observations have pointed out, is a dusty torus that absorbs part of the UV radiation and reemits it in the mid-infrared. High resolution infrared observations show that the outer radius of the emission region in the torus has a value between 1 pc to 17 pc (Elitzur 2005).

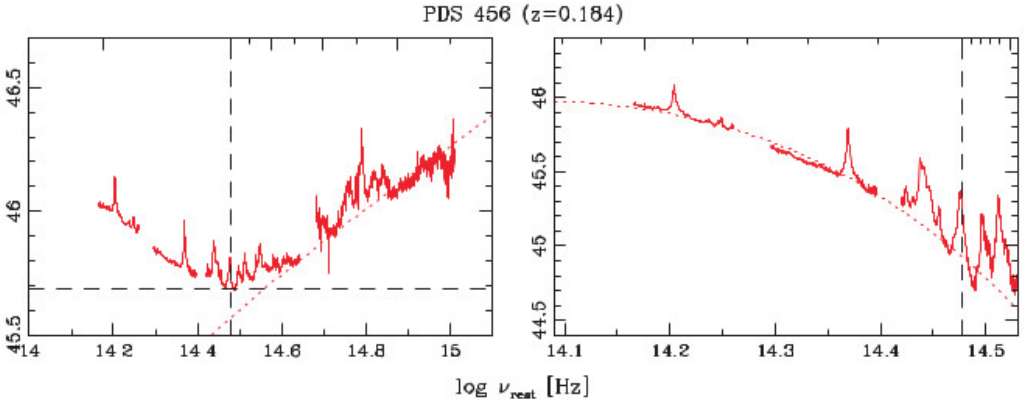

Figure 2: The left panel shows the quasar host galaxy subtracted SED at 1μm. The dotted line indicates the accretion disc spectrum that approximates best the continuum bluewards of ~ 1 μm. Right panel, as in left-hand panel with the accretion disc spectrum subtracted. The dotted line shows the blackbody spectrum fitted to the continuum redwards of ~1 μm(Landt et al. 2011).

Survey spectra, such as the SDSS ones, are often contaminated by emission or absorption far from the active nucleus. The origin of this emission is the quiescent galaxy host and circumnuclear star formation (Nolan et al. 2001). For example, the host galaxy contamination to the SED in the optical was subtracted in order to get a spectrum as the one shown in figures 2. The host galaxy flux is the one coming from the stellar populations present in the galaxy. Absorption features of the H and K of ionized Ca doublet and Hβ, among others, are observed in this spectrum (See Figure 3).

At longer wavelengths there is a clear dichotomy in the radio observation and it is defined

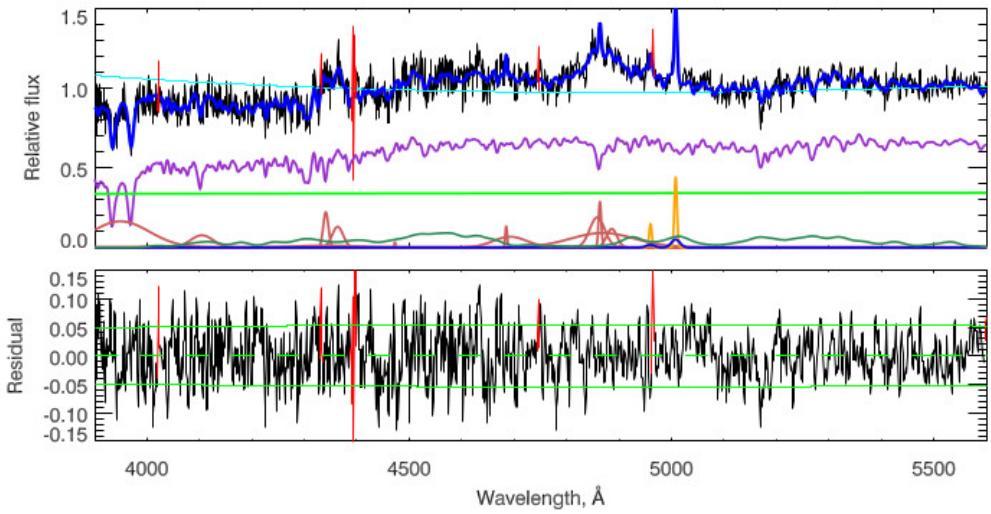

Figure 3: Influence of the host galaxy on quasar spectra. From top to bottom, the observed quasar spectra in black line, the model of the spectra in blue, host galaxy spectra in the purple line and the fitting of the spectral features of the quasars in different colors (Bon et al. in preparation). The lower panel shows the residuals between the model and the observation.

by the radio-loudness parameter R_K. R_K is the ratio of radio at 5 GHz to optical B-band monochromatic luminosity. Originally, the limit between radio-quiet (RQ) and radio-loud (RL) quasars has been set at R_K = 10 (Kellermann et al. 1989). With this definition it has been found that 10 percent of the sources are radio loud. Xu et al. (1999) showed that there is a luminosity dependence in the value of R_K. They found that the dividing line which separates the two populations follows $L_{5GHz} \propto L_{[OIII]}^{0.5}$, indicating that R_K increases towards low luminosities. Xu et al. suggests the use of $R_K \propto L^{-0.5}$. However, Padovani (2016) states that it is not worth it to look for a bimodality in R_K, then the RQ-RL classification is obsolete. The presence or lack of strong relativistic jets is the main difference between the two groups, his suggestion is to use instead a jetted-not jetted classification.

The radio-morphology of a quasar depends on the observed frequency. It usually shows a compact central component and possibly one or more extended components. In some cases, the extended components are observed in the form of two radio lobes situated more or less symmetrically around the optical position of the quasar. These lobes are frequently connected to the central core by jets, which are thin emission structures probably related to the energy transport from the core into the lobes. For radio-loud quasars, we distinguish between a core-dominated and lobe-dominated radio structure.

As mentioned earlier, the radio spectrum of quasars follows a power law. Sources with $\alpha < 0.5$ are described as flat-spectrum and we associate them with core-dominated RL quasars. If $\alpha > 0.5$, sources are called steep spectrum and we relate them with lobe-dominated structures. The spectral energy distribution is such that the radio emission is interpreted as synchrotron radiation emitted by relativistic electrons.

In practice, to identify sources that are "jetted" following Padovani (2016), Zamfir et al. (2008) suggested to consider a minimum log $R_K \approx 1.8$. Sources in between log R_K 1 and 1.88, are considered radio-intermediate by these authors. Radio intermediate sources are distributed in a way consistent with the distribution of RQ sources in the optical plane of the Eigenvector 1 main sequence, described in Chapter 2. Bonzini et al. (2015) distinguish between RL and RQ sources relying on the fact that RL sources don't follow the FIR-radio correlation that star forming systems and RQ quasars do. This criterion may become extremely useful to distinguish between RL AGN and other sources now that the flux limits of radio surveys have been improved down to the micro-Jansky level (check on the eVLA site). With the improved sensitivity, thermal sources (i.e., starforming) will become the wide majority of detections, at variance with the brightest radio sources in the sky – detected since the earliest stages of radio astronomy – that are all powerful RL AGNs.

1.3 Optical and Ultraviolet spectra

The UV and optical spectra of quasars feature strong and very broad emission lines. Typically, we observe lines of the Balmer series and Lyα of hydrogen, and metal lines of ions like MgII, CIII and CIV. See Figure 4 for a representative UV and optical spectrum where the main features are labeled. The variety of emission lines in quasars allows us to infer a large amount of physical properties as electron density n_e, temperature T, column density N_c and ionization level. There are many different ways to classify emission lines depending on their probability to be present deduced from the quantum mechanical rules, the degree of ionization of the atom or the width of the line profile. For a more detailed view of the composite spectra see Figure 5.

Concerning the width of the line profile, we identify two different regions in quasars: a Broad line region (BLR) and a Narrow line region (NLR) (Khachikian and Weedman 1974). The BLR produce emission from permitted transitions usually characterized by broad lines.

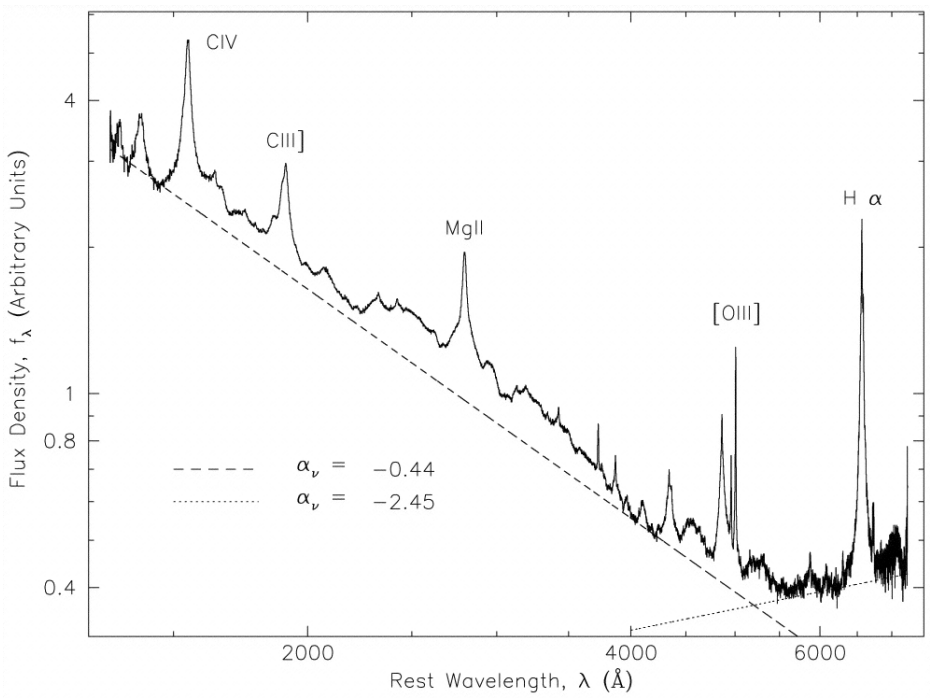

Figure 4: Geometric mean composite spectra of over 2200 individual quasar spectra from the SDSS. The main features are labeled and a two-power law continuum is shown in dashed lines (Vanden Berk et al. 2001).

They have a range FWHM $\approx 1000 - 15,000$ km s^{-1} (Osterbrock and Mathews 1986; Sulentic et al. 2000).

The density of the BLR can be estimated from the presence of semi-forbidden lines and its value ($n_e \gtrsim 10^{9.5}$ cm^{-3}) is high for nebular standards. The absence of forbidden lines is used to derive a lower limit for the gas density. For example, the absence of [OIII] λ5007 indicates that collisional de-excitation takes place which, in turn, implies $n_e \geq 10^8$ cm^{-3} (Pradhan & Nahar 2015). This said, the determination of the density of the BLR has been a thorny issue that has been around since the early times after the discovery of quasars (Osterbrock 1970). On the one hand, the strength of the line CIII] λ1909 suggests an upper limit to the density of the gas $n_e \lesssim 10^{10}$ cm^{-3}. On the other, the strength of several lines indicate higher density. For instance the CaII triplet intensity with respect to Paschen lines and Balmer lines indicates a lower limit of $n_e \gtrsim 10^{10.5}$ cm^{-3} (Matsuoka et al. 2008; Martínez-Aldama et al. 2015). Very high density is also implied by reverberation mapping results: for the BLR radii derived from reverberation mapping, the density has to be high to allow for a reasonable value of the ionization parameter (Peterson & Wandel 1999; Negrete et al. 2013). These apparently contracting lines of evidence indicate the occurrence of a

range of densities in the BLR of at least most quasars which can be associated with a stratification in the physical properties of the BLR. Only in the special class of "extremely accreting quasars" (described in Chapter 2 and 3) the BLR appears to become relatively homogeneous with n_e that may be in excess of $\approx 10^{12}$ cm^{-3} (Negrete et al. 2012). The CIII] line is very weak or even absent in the spectra of these sources.

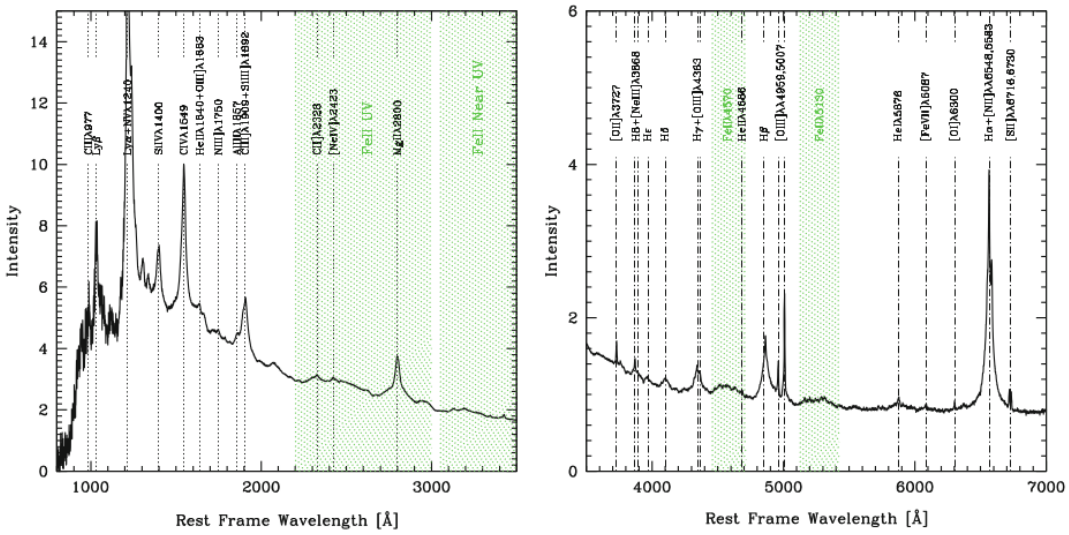

Figure 5: A more detailed view of the optical and UV composite spectra from SDSS observations. The dotted lines indicates the position of the prominent emission features and the green shaded area covers the FeII emission (Chapter 3, D'Onofrio et al. (2012)).

The spectral lines together with the continuum emission from the central source enable us to determine physical parameters as the size of the BLR r_{BLR} by means of the reverberation mapping technique. The principle of this technique is the flux variability in continuum emission and the response of the spectral line emission. The heating and the ionization of the gas surrounding the black hole is produced by the continuum emission. Since the UV radiation varies, we expect the corresponding variation in the physical conditions of the BLR. Then, a decreasing continuum flux should lead to a decreasing line flux. Due to the finite size of the BLR, the observed variability in the lines will be delayed in time compared to the ionizing continuum. This variability can be also observed in other frequency bands as IR emission (Hönig et al. 2014) and X-rays. See Figure 6 for an example of delay in the near IR light curve. Kaspi et al. (2000) provides values $R_{BLR} \sim 100$ light-days for the BLR. An important relation from the latter study is $R_{BLR} \propto L^{0.5}$ which is the so-called Kaspi Law. This law tells us that in other words, BLR in a quasar is typically hundred times

larger than the one in a Seyfert galaxy. More important, this means the size of the Broad line region could be use as a redshift independent method to determine luminosity and we give more details on the cosmological application in Chapter 3.

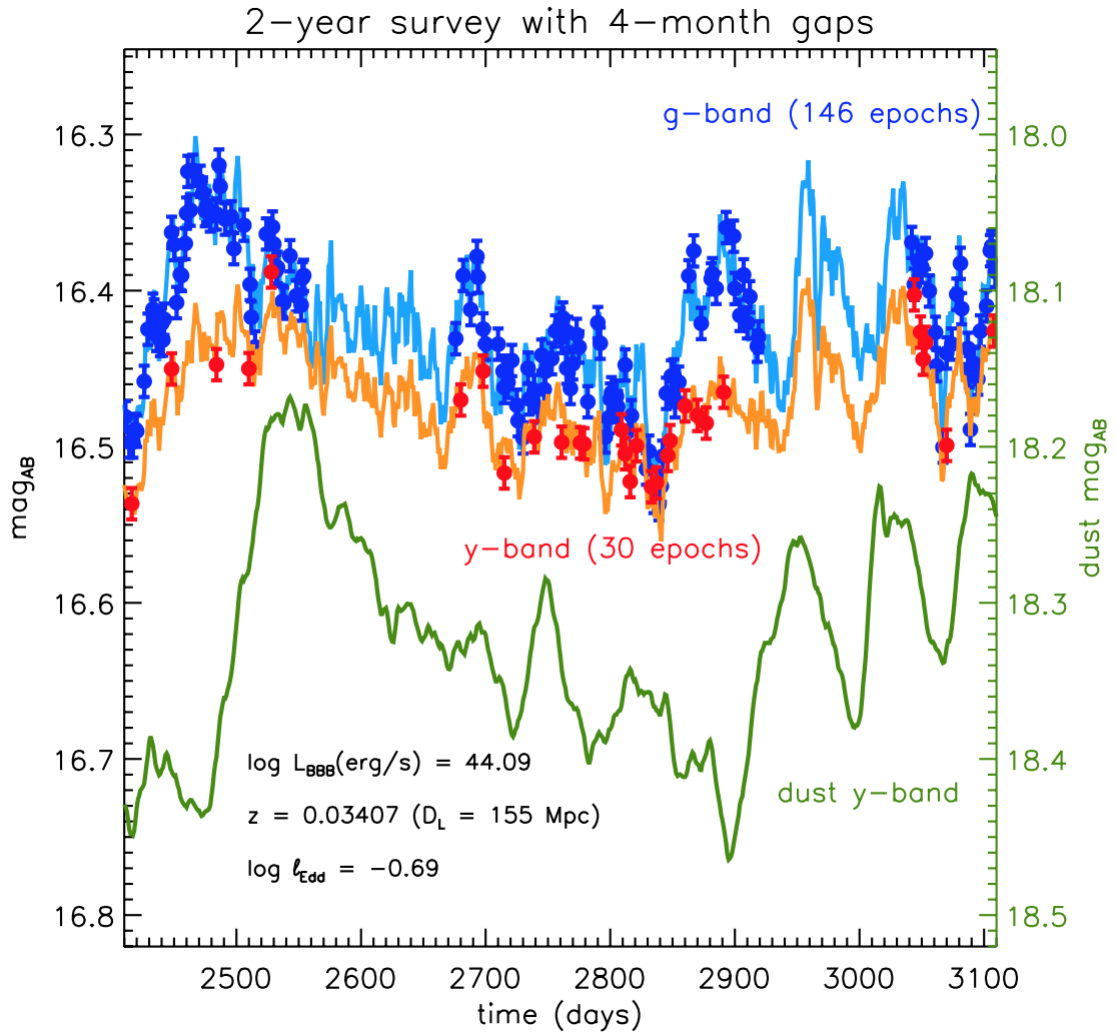

Figure 6: Simulated AGN variability curve in the optical g-band for the central source and in the IR y-band for the dusty torus as it is expected to be seen with the LSST telescope. Hnig et al. 2014 proposes reverberation mapping of the emission in the dusty torus to infers its size and sublimation radius, as well as, the use of this measaurement to define a standard candle.

There is one distinction in the BLR concerning the ionization potential of the atom that produces emission. High ionization lines (HIL) are produced by ions with ionization potential $\geq$ 50 eV, between the broad features we observe are CIV λ1549 and HeII, and the narrow [OIII]$\lambda\lambda$4959, 5007, HeII, NeIII. Conversely, low ionization lines come from ions with ionization potential $\leq$ 20 eV. Some examples are are Balmer, FeII, MgIIλ2800 and CaII triplet with broad profiles and [OI]λ6300, [SII]$\lambda\lambda$6716 with narrow profiles.

Table 1.1: High ionization lines (HIL) and Low ionization lines (LIL) in quasar spectra.

Ionization	**Width**	*Broad*	*Narrow*
High (~ 50 eV)		CIVλ1549, HeII	[OIII]$\lambda\lambda$4959,5007, HeII, NeIII
Low (<20 eV)		Balmer(Hβ), FeII, MgIIλ2800, CaII IR Triplet	Balmer, [OI]λ6300, [SII]$\lambda\lambda$6716,6731

The HIL-LIL distinction is useful because the region where the emission comes from depends on the ionization level (See table 1.1). Collin-Souffrin et al. (1988) proposed that low-pressure optically thin clouds illuminated by relatively soft continuum radiation emit the high ionization broad lines. For instance, CIV λ1549 is the result of the interaction with ultraviolet photons of the central source and the C^{+3} ion located in an environment with relative low pressure and relatively large ionization parameter U. The analysis of its asymmetrically blue profile suggests that the origin of this line is a wind/outflow from the accretion disk. LIL are emitted by high-pressure optically thick medium, illuminated mainly by hard X-rays, possibly in the outer region of the an accretion disk. The most representative of LIL is the Hβ emission, which is the main focus of this study due to its convenient location in the optical part of the spectrum and the fact that its profile is not strongly affected by other features neither is blended with another prominent line.

The optical and UV spectra also provide us with physical information of the more extended NLR. In this region the lines have typical widths ~ 200-2000 km s^{-1} and they dominated by forbidden lines as [OIII] and [NII]. Contrary to the BLR, the narrow line region can be resolved and its size is approximately 3 kpc for a very luminous quasar (Chapter 7, Netzer 2013. The most prominent optical emission lines of the NLR are [O III] λ5007 and Hα+[N II] $\lambda\lambda$6548, 6584. No line variability is observed in the NLR. Bennert et al. (2002) correlates the size of the NLR as $R_{NLR} \propto L^{0.52}_{[0III]}$. In the case of the electron density, the line ratios of forbidden lines yield n_e ~ 10^4 cm^{-3} in the BLR. This density is determined by measuring the intensity ratio of two lines from a single ion assuming a balance between the depopulation rate by collisions and spontaneous emission of the higher energy state and the excitation collisional rate of the lower level. A well-known example is the doublet [SII] $\lambda\lambda$6716, 6731 which is consistent with a density span from 10^2 to 10^4

cm^{-3} (Peterson 1997).

1.4 Optical Surveys

In this section I try to present a quick look on the optical surveys that have been developed since the discovery of quasars to nowadays, in other words from early surveys as Palomar Sky Survey (PGS) to the current Sloan Digital Sky Survey (SDSS).

Firstly, the radio surveys, as we have mentioned before, represent the starting point of quasars such as 3C, 4C, Tonantzintla, Ohio and Parkes. Afterwards, the optical studies of quasars initiates with the Bright Quasar Survey (or also called Palomar-Green PG survey). This survey works under the UV excess technique: the object identified as quasar is brighter through an ultraviolet filter than through a blue filter.

The PG survey was supposed to find all objects in a 10,668 square degree region in the north galactic cap, having B magnitudes brighter than 16.16 and $U - B$ colors bluer than −0.46. The objects with UV excess were observed spectroscopically to classify them. The final result were 114 quasars from which 88 quasars have redshift $z < 0.5$ and the range in absolute magnitude were M_B = −20.75 to −27.09. The limiting magnitude in average was B = 16.16 and corresponds to an absolute magnitude M_B = −26.09 at a redshift $z < 0.5$.

The low-redshift sample, called active galactic nuclei, 21 were classified as Seyfert galaxies and 67 as quasars, where the criteria is the appearance on the photographic plate (stellar or fuzzy galaxies) but it is not a quantitative criteria.

1.5 Sloan Digital Sky Survey

Table 1.2: SDSS main properties

Feature	SDSS	BOSS
Fibers per plate	640	1,000
Fiber diameter	3 arcsec (180 μ m)	2 arcsec (120 μm)
Wavelength coverage	3800-9200 Å	3650-10,400 Å
Resolution	1500 at 3800 Å	2500 at 9000 Å
Pixel spacing	log-wavelength (10^{-4} dex)	
Units	10^{-17} erg cm^{-2} s^{-1} $Å^{-1}$	
Wavelength calibration	< 5 km/s	

The SDSS began regular survey operations in 2000. It involved several phases, SDSS-I (2000-2005), SDSS-II (2005-2008). SDSS-III (2008-2014), and SDSS-IV (2014-), for a total of 14 Data releases. Data Release 14 includes the complete dataset of optical single-fibre spectroscopy of the Sloan Digital Sky Survey through July 2016 more than four million spectra comprising extra-galactic and galactic spectra. The SDSS-IV provides spectra for about 500,000 quasars in DR 14. Each of these phases has involved more than one survey. The four phases were designed according to different science goals. The Legacy Survey included SDSS-I/II, while Baryon Oscillation Spectroscopic Survey (BOSS) (SDSS-III) and the extended-BOSS (eBOSS) spanned SDSS-III and IV.

The SDSS spectra for many objects are taken simultaneously. The spectrographs are connected by fiber optic cables to holes drilled in an aluminum plate in the telescopes focal plane. The drilled holes constitute the fiber aperture. With this arrangement any SDSS spectrum is identified with three numbers: (1) plate number, an integer indicating which SDSS plate was used to collect the spectrum; (2) the Modified Julian Date (MJD) of the observations.; (3) an integer identifying the fiber number (1 to 640 for SDSS-I/II; 1 to 1000 for BOSS).

The observations provide an image which yields 640 (SDSS) or 1000 (BOSS) spectra on each plate, each as a row in the image. The spectra are flux- and wavelength-calibrated with logarithmic wavelength grid spacing which is the same for all plates ($\log \lambda_{i+1} - \log \lambda_i = 0.0001$) but the starting wavelength differs from plate to plate. All fibers on the same plate share exactly the same grid. The SDSS wavelength scale is based on vacuum wavelengths. Important Information about SDSS and BOSS spectra is provided in Table 1.2

Especially relevant for quasar studies is the difference between SDSS-I and SDSS - II and the later phases (BOSS and eBOSS). There is a calibration issue for quasar spectra that were observed as part of the BOSS (Dawson et al. 2013), and later Phases. We describe the problem following Punsly et al. (2016). Specifically, in order to increase spectral sensitivity for quasars, the hole drilled in the plate over the fiber is centered on the displacement associated with 4000 Å. However, the calibration of the star has a hole centered about the displacement associated with 5400Å. Due to atmospheric differential refraction (ADR), this inconsistency artificially raises the flux level in the blue for the quasar and underestimates the flux density of the standard star at 4000 Å. The calibration standard star was observed with the fiber at a displacement centered at 5400 Å and there is significant displacement

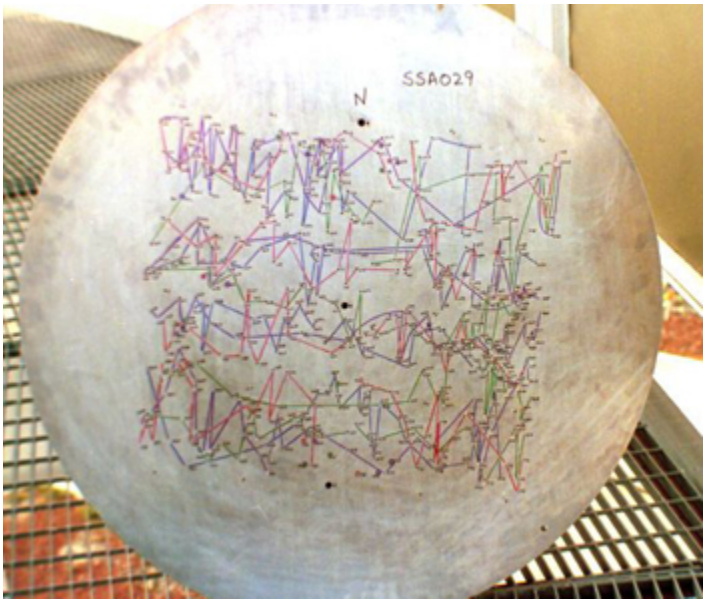

Figure 7: A plate used for the collection of the SDSS spectra.

from the center of the fiber at 3900 Å, and these fluxes are significantly underestimated. These effects can enhance the detected quasar blue flux by more than 15%, and significantly distort the SED on the blue side of Hβ. A picture of one plate is shown in Fig. 7 and a discussion of this circumstance can be found in (Dawson et al. 2013).

The image of Fig. 8 shows previews of 12 typical SDSS spectra. Individually most of these spectra are too noisy (typically $S/N < 5$ in the continuum near the two lines) to yield good measures. We think that the best path to overcome the low-S/N of individual spectra involves generating median composite spectra in the 4DE1 context (Sulentic et al. 2002, §2.1). The composites can provide very high S/N line profiles from which more accurate measures can be obtained. Table 1.2 summarizes the main properties of the SDSS.

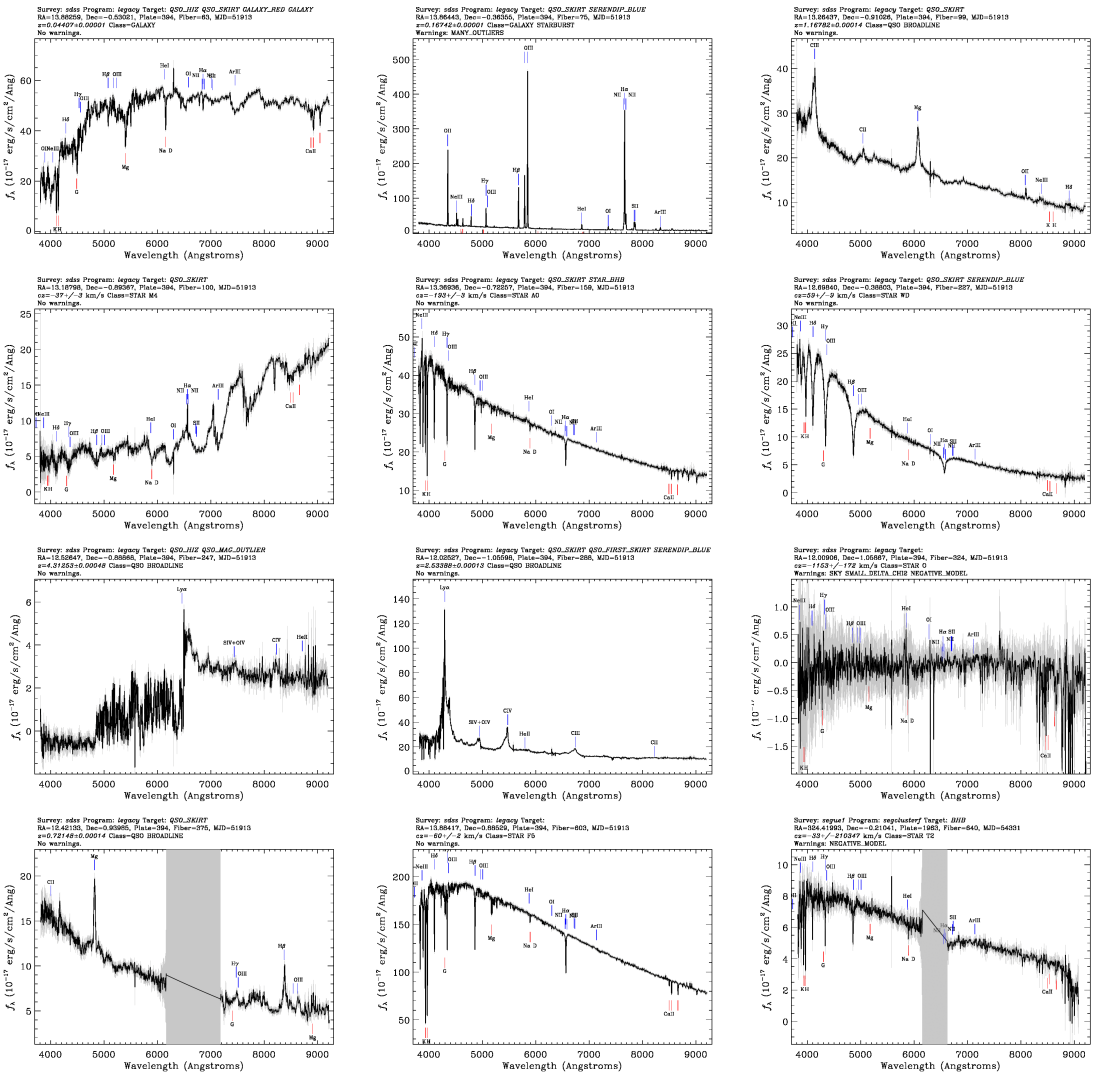

Figure 8: 12 spectra obtained with a single exposure through the drilled plate.

Bibliography

Abramowicz, M. A., Czerny, B., Lasota, J. P., & Szuszkiewicz, E. 1988, *Ap. J.*, 332, 646

Antonucci, R. R. J. & Miller, J. S. 1985, *Ap. J.*, 297, 621

Bachev, R., Marziani, P., Sulentic, J. W., et al. 2004, ApJ, 617, 171

Baldwin, J. A., Burke, W. L., Gaskell, C. M., & Wampler, E. J. 1978, *Nature*, 273, 431

Baldwin, J. A., Ferland, G. J., Korista, K. T., et al. 1996, *Ap. J.*, 461, 664

Bennert, N., Falcke, H., Schulz, H., Wilson, A. S., & Wills, B. J. 2002, *Ap. J. Lett.*, 574, L105

Bensch, K., del Olmo, A., Sulentic, J., Perea, J., & Marziani, P. 2015, Journal of Astrophysics and Astronomy, 36, 467

Bentz, M. C., Denney, K. D., Grier, C. J., et al. 2013, *Ap. J.*, 767, 149

Bian, W.-H., Fang, L.-L., Huang, K.-L., & Wang, J.-M. 2012, *MNRAS*, 427, 2881

Boller, T., Brandt, W. N., & Fink, H. 1996, *Astr. Astroph.*, 305, 53

Bon, E., Marziani, P., & Bon, N. 2017, in IAU Symposium, Vol. 324, IAU Symposium, 176–179

Bon, E., Popović, L. Č., Gavrilović, N., Mura, G. L., & Mediavilla, E. 2009, *MNRAS*, 400, 924

Bon, N., Bon, E., Marziani, P., & Jovanović, P. 2015, *ApSS*, 360, 7

Bonzini, M., Mainieri, V., Padovani, P., et al. 2015, *MNRAS*, 453, 1079

Boroson, T. A. & Green, R. F. 1992, ApJS, 80, 109

Brotherton, M. S., Runnoe, J. C., Shang, Z., & DiPompeo, M. A. 2015, *MNRAS*, 451, 1290

Campbell, H., D'Andrea, C. B., Nichol, R. C., et al. 2013, *Ap. J.*, 763, 88

Chelouche, D., Daniel, E., & Kaspi, S. 2012, ApJL, 750, L43

Coatman, L., Hewett, P. C., Banerji, M., & Richards, G. T. 2016, *MNRAS*, 461, 647

Collin, S., Kawaguchi, T., Peterson, B. M., & Vestergaard, M. 2006, A&Ap, 456, 75

Collin-Souffrin, S., Dyson, J. E., McDowell, J. C., & Perry, J. J. 1988, MNRAS, 232, 539

Conley, A., Guy, J., Sullivan, M., et al. 2011, *Ap. J. Suppl.*, 192, 1

Corbin, M. R. 1995, *Ap. J.*, 447, 496

Cracco, V., Ciroi, S., Berton, M., et al. 2016, *MNRAS*, 462, 1256

Czerny, B., Hryniewicz, K., Maity, I., et al. 2012, ArXiv e-prints

Davidson, K. 1972, *Ap. J.*, 171, 213

Davis, S. W. & Laor, A. 2011, *Ap. J.*, 728, 98

Dawson, K. S., Schlegel, D. J., Ahn, C. P., et al. 2013, *A. J.*, 145, 10

Diamond-Stanic, A. M., Fan, X., Brandt, W. N., et al. 2009, *Ap. J.*, 699, 782

Diaz, A. I., Terlevich, E., & Terlevich, R. 1989, *MNRAS*, 239, 325

Dietrich, M., Hamann, F., Shields, J. C., et al. 2002, *Ap. J.*, 581, 912

Done, C., Davis, S. W., Jin, C., Blaes, O., & Ward, M. 2012, *MNRAS*, 420, 1848

D'Onofrio, M. & Burigana, C. 2009, Questions of Modern Cosmology: Galileo's Legacy

D'Onofrio, M., Marziani, P., & Sulentic, J. W., eds. 2012, Astrophysics and Space Science Library, Vol. 386, Fifty Years of Quasars From Early Observations and Ideas to Future Research (Springer Verlag, Berlin-Heidelberg)

Du, P., Lu, K.-X., Hu, C., et al. 2016, *Ap. J.*, 820, 27

Dultzin-Hacyan, D., Krongold, Y., Fuentes-Guridi, I., & Marziani, P. 1999, ApJ, 513, L111

Elitzur, M. 2005, ArXiv Astrophysics e-prints

Elvis, M. 2000, *Ap. J.*, 545, 63

Elvis, M. & Karovska, M. 2002, *Ap. J. Lett.*, 581, L67

Emmering, R. T., Blandford, R. D., & Shlosman, I. 1992, *Ap. J.*, 385, 460

Eun, D.-i., Woo, J.-H., & Bae, H.-J. 2017, *Ap. J.*, 842, 5

Flohic, H. M. L. G., Eracleous, M., & Bogdanović, T. 2012, ApJ, 753, 133

Folatelli, G., Phillips, M. M., Burns, C. R., et al. 2010, *A. J.*, 139, 120

Fontanot, F., De Lucia, G., Monaco, P., Somerville, R. S., & Santini, P. 2009, *MNRAS*, 397, 1776

Fraix-Burnet, D., Marziani, P., D'Onofrio, M., & Dultzin, D. 2017, Frontiers in Astronomy and Space Sciences, 4, 1

Frank, J., King, A., & Raine, D. J. 2002, Accretion Power in Astrophysics: Third Edition, iii edition edn. (Cambridge: Cambridge University Press)

Grupe, D. 2004, *A. J.*, 127, 1799

Hirschmann, M., Dolag, K., Saro, A., et al. 2014, *MNRAS*, 442, 2304

Hönig, S. F., Watson, D., Kishimoto, M., & Hjorth, J. 2014, *Nature*, 515, 528

Hook, I. M. 2013, Royal Society of London Philosophical Transactions Series A, 371, 20282

Jacoby, G. H., Branch, D., Ciardullo, R., et al. 1992, PASP, 104, 599

Jarvis, M. J. & McLure, R. J. 2006, *MNRAS*, 369, 182

Joly, M., Véron-Cetty, M., & Véron, P. 2008, in Revista Mexicana de Astronomia y Astrofisica Conference Series, Vol. 32, 59–61

Kaspi, S., Brandt, W. N., Maoz, D., et al. 2007, *Ap. J.*, 659, 997

Kaspi, S., Maoz, D., Netzer, H., et al. 2005, ApJ, 629, 61

Kaspi, S., Smith, P. S., Netzer, H., et al. 2000, *Ap. J.*, 533, 631

Katgert, P., Katgert-Merkelijn, J. K., Le Poole, R. S., & van der Laan, H. 1973, *Astr. Astroph.*, 23, 171

Kellermann, K. I., Sramek, R., Schmidt, M., Shaffer, D. B., & Green, R. 1989, *A. J.*, 98, 1195

Kelly, B. C., Vestergaard, M., Fan, X., et al. 2010, *Ap. J.*, 719, 1315

Khachikian, E. Y. & Weedman, D. W. 1974, *Ap. J.*, 192, 581

Kirshner, R. P. 1999, Proceedings of the National Academy of Science, 96, 4224

Kollatschny, W. & Zetzl, M. 2011, *Nature*, 470, 366

Krolik, J. H. & McKee, C. F. 1978, *Ap. J. Suppl.*, 37, 459

Kruczek, N. E., Richards, G. T., Gallagher, S. C., et al. 2011, *A. J.*, 142, 130

La Franca, F., Bianchi, S., Ponti, G., Branchini, E., & Matt, G. 2014, *Ap. J. Lett.*, 787, L12

Landt, H., Elvis, M., Ward, M. J., et al. 2011, *MNRAS*, 414, 218

Laor, A. 2000, *Ap. J. Lett.*, 543, L111

Laor, A. 2006, *Ap. J.*, 643, 112

Lynden-Bell, D. 1969, *Nature*, 223, 690

Marinucci, A., Bianchi, S., Nicastro, F., Matt, G., & Goulding, A. D. 2012, The Astrophysical Journal, 748, 130

Martínez-Aldama, M. L., Dultzin, D., Marziani, P., et al. 2015, ApJS, 217, 3

Marziani, P., Dultzin-Hacyan, D., D'Onofrio, M., & Sulentic, J. W. 2003a, AJ, 125, 1897

Marziani, P., Dultzin-Hacyan, D., & Sulentic, J. W. 2006, in New Developments in Black Hole Research, ed. P. V. Kreitler (Nova Press, New York), 123

Marziani, P., Negrete, C. A., Dultzin, D., et al. 2017, in IAU Symposium, Vol. 324, IAU Symposium, 245–246

Marziani, P. & Sulentic, J. W. 2012, NARev, 56, 49

Marziani, P. & Sulentic, J. W. 2013, ArXiv e-prints

Marziani, P. & Sulentic, J. W. 2014, *MNRAS*, 442, 1211

Marziani, P., Sulentic, J. W., Dultzin-Hacyan, D., Calvani, M., & Moles, M. 1996, ApJS, 104, 37

Marziani, P., Sulentic, J. W., Negrete, C. A., et al. 2014, The Astronomical Review, 9, 6

Marziani, P., Sulentic, J. W., Negrete, C. A., et al. 2010, *MNRAS*, 409, 1033

Marziani, P., Sulentic, J. W., Plauchu-Frayn, I., & del Olmo, A. 2013a, AAp, 555, 89, 16pp

Marziani, P., Sulentic, J. W., Plauchu-Frayn, I., & del Olmo, A. 2013b, ApJ, 764

Marziani, P., Sulentic, J. W., Zwitter, T., Dultzin-Hacyan, D., & Calvani, M. 2001, ApJ, 558, 553

Marziani, P., Zamanov, R. K., Sulentic, J. W., & Calvani, M. 2003b, MNRAS, 345, 1133

Mathur, S. 2000, *MNRAS*, 314, L17

Matsuoka, Y., Kawara, K., & Oyabu, S. 2008, ApJ, 673, 62

Mineshige, S., Kawaguchi, T., Takeuchi, M., & Hayashida, K. 2000, *PASJ*, 52, 499

Mortlock, D. J., Warren, S. J., Venemans, B. P., et al. 2011, *Nature*, 474, 616

Murray, N., Chiang, J., Grossman, S. A., & Voit, G. M. 1995, *Ap. J.*, 451, 498

Nagao, T., Marconi, A., & Maiolino, R. 2006, A&Ap, 447, 157

Negrete, A., Dultzin, D., Marziani, P., & Sulentic, J. 2012, ApJ, 757, 62

Negrete, C. A. 2011, PhD thesis, UNAM, Mexico, (2011)

Negrete, C. A., Dultzin, D., Marziani, P., & et al. 2017, in preparation

Negrete, C. A., Dultzin, D., Marziani, P., & Sulentic, J. W. 2013, *Ap. J.*, 771, 31

Negrete, C. A., Dultzin, D., Marziani, P., & Sulentic, J. W. 2014, *Ap. J.*, 794, 95

Netzer, H. 1990, in Active Galactic Nuclei, ed. R. D. Blandford, H. Netzer, L. Woltjer, T. J.-L. Courvoisier, & M. Mayor, 57–160

Netzer, H. 2013, The Physics and Evolution of Active Galactic Nuclei (Cambridge University Press)

Nolan, L. A., Dunlop, J. S., Kukula, M. J., et al. 2001, *MNRAS*, 323, 308

Osterbrock, D. E. & Pogge, R. W. 1985, *Ap. J.*, 297, 166

Padovani, P. 2016, AApR, 24, 13

Padovani, P., Burg, R., & Edelson, R. A. 1990, *Ap. J.*, 353, 438

Padovani, P. & Rafanelli, P. 1988, *Astr. Astroph.*, 205, 53

Pâris, I., Petitjean, P., Ross, N. P., et al. 2017, *Astr. Astroph.*, 597, A79

Perlmutter, S., Aldering, G., Goldhaber, G., et al. 1999, *Ap. J.*, 517, 565

Perlmutter, S., Gabi, S., Goldhaber, G., et al. 1997, *Ap. J.*, 483, 565

Peterson, B. M. 1997, An Introduction to Active Galactic Nuclei (Cambridge University Press)

Peterson, B. M. & Wandel, A. 1999, *Ap. J. Lett.*, 521, L95

Pradhan, A. K. & Nahar, S. N. 2015, Atomic Astrophysics and Spectroscopy (Cambridge University Press)

Punsly, B., Marziani, P., Zhang, S., Muzahid, S., & O'Dea, C. P. 2016, *Ap. J.*, 830, 104

Reviglio, P. M. & Helfand, D. J. 2009, ArXiv e-prints

Richards, G. T., Kruczek, N. E., Gallagher, S. C., et al. 2011, *A. J.*, 141, 167

Risaliti, G. & Lusso, E. 2015, *Ap. J.*, 815, 33

Rokaki, E., Lawrence, A., Economou, F., & Mastichiadis, A. 2003, *MNRAS*, 340, 1298

Runnoe, J. C., Brotherton, M. S., DiPompeo, M. A., & Shang, Z. 2014, *MNRAS*, 438, 3263

Sandage, A. 1965, *Ap. J.*, 141, 1560

Sądowski, A., Narayan, R., McKinney, J. C., & Tchekhovskoy, A. 2014, *MNRAS*, 439, 503

Schechter, P. L. 2005, in IAU Symposium, Vol. 201, New Cosmological Data and the Values of the Fundamental Parameters, ed. A. N. Lasenby & A. Wilkinson, 209

Schneider, D. P., Richards, G. T., Hall, P. B., et al. 2010, *A. J.*, 139, 2360

Shang, Z., Wills, B. J., Wills, D., & Brotherton, M. S. 2007, AJ, 134, 294

Shemmer, O., Trakhtenbrot, B., Anderson, S. F., et al. 2010, *Ap. J. Lett.*, 722, L152

Shen, Y. 2013, Bulletin of the Astronomical Society of India, 41, 61

Shen, Y. & Ho, L. C. 2014, *Nature*, 513, 210

Shen, Y., Richards, G. T., Strauss, M. A., et al. 2011, *Ap. J. Suppl.*, 194, 45

Sulentic, J., Marziani, P., & Zamfir, S. 2011, Baltic Astronomy, 20, 427

Sulentic, J. W., Bachev, R., Marziani, P., Negrete, C. A., & Dultzin, D. 2007, ApJ, 666, 757

Sulentic, J. W., del Olmo, A., Marziani, P., et al. 2017, ArXiv e-prints

Sulentic, J. W., Marziani, P., del Olmo, A., et al. 2014, *Astr. Astroph.*, 570, A96

Sulentic, J. W., Marziani, P., & Dultzin-Hacyan, D. 2000a, ARA&A, 38, 521

Sulentic, J. W., Marziani, P., Zamanov, R., et al. 2002, ApJL, 566, L71

Sulentic, J. W., Marziani, P., Zwitter, T., Dultzin-Hacyan, D., & Calvani, M. 2000b, ApJL, 545, L15

Sulentic, J. W., Zamfir, S., Marziani, P., et al. 2003, ApJL, 597, L17

Sun, J. & Shen, Y. 2015, *Ap. J. Lett.*, 804, L15

Szuszkiewicz, E., Malkan, M. A., & Abramowicz, M. A. 1996, *Ap. J.*, 458, 474

Trevese, D., Paris, D., Stirpe, G. M., Vagnetti, F., & Zitelli, V. 2007, *Astr. Astroph.*, 470, 491

Ulrich, M.-H., Maraschi, L., & Urry, C. M. 1997, *ARAA*, 35, 445

Urry, C. M. & Padovani, P. 1995, PASP, 107, 803

Vanden Berk, D. E., Richards, G. T., Bauer, A., et al. 2001, AJ, 122, 549

Véron-Cetty, M.-P., Véron, P., & Gonçalves, A. C. 2001, AAp, 372, 730

Villarroel, B. & Korn, A. J. 2014, Nature Physics, 10, 417

Walsh, J. L., Barth, A. J., Ho, L. C., & Sarzi, M. 2013, *Ap. J.*, 770, 86

Wandel, A., Peterson, B. M., & Malkan, M. A. 1999, *Ap. J.*, 526, 579

Wang, J., Wei, J. Y., & He, X. T. 2006, *Ap. J.*, 638, 106

Wang, J.-M., Du, P., Li, Y.-R., et al. 2014, *Ap. J. Lett.*, 792, L13

Wang, J.-M., Du, P., Valls-Gabaud, D., Hu, C., & Netzer, H. 2013, Physical Review Letters, 110, 081301

Wang, T., Brinkmann, W., & Bergeron, J. 1996, A&Ap, 309, 81

Watson, D., Denney, K. D., Vestergaard, M., & Davis, T. M. 2011, *Ap. J. Lett.*, 740, L49

Wills, B. J. & Browne, I. W. A. 1986, *Ap. J.*, 302, 56

Wills, B. J., Laor, A., Brotherton, M. S., et al. 1999, *Ap. J. Lett.*, 515, L53

Woo, S. C., Turnshek, D. A., Badenes, C., & Bickerton, S. 2013, ArXiv e-prints

Xu, C., Livio, M., & Baum, S. 1999, *A. J.*, 118, 1169

Yip, C. W., Connolly, A. J., Vanden Berk, D. E., et al. 2004, *A. J.*, 128, 2603

Zamanov, R., Marziani, P., Sulentic, J. W., et al. 2002, ApJL, 576, L9

Zamfir, S., Sulentic, J. W., & Marziani, P. 2008, MNRAS, 387, 856

Zamfir, S., Sulentic, J. W., Marziani, P., & Dultzin, D. 2010, *MNRAS*, 403, 1759

Zhang, K., Wang, T.-G., Gaskell, C. M., & Dong, X.-B. 2013, *Ap. J.*, 762, 51

Chapter 2

Quasars classification

The main advantage of composite spectra such as the SDSS one in Fig. 5 (Vanden Berk et al. 2001) is that S/N is so high that identification of many faint features that remain invisible in individual spectra becomes possible. Beyond line identification and some basic information a composite spectrum computed over all type-1 sources can yield deceptive results: spectral properties of type 1 quasars do not scatter randomly with reasonable dispersion around the median, as we will see in this Chapter. Marziani et al. (2006) remarked that the use of average line ratios from composite survey spectra has led to an impasse in the attempt of reproducing the observations through simple photoionization models (see e.g., Netzer 1990, and references therein). High quality data (Shang et al. 2007) with nearly simultaneous FUSE, HST and optical observations emphasize the quasar diversity in terms of emission line and continuum spectrophotometric properties.

2.1 Unification schemes

Unification is a potentially powerful framework within which to organize various aspects of quasar phenomenology. Orientation unification is a special challenge faced by quasar (but not stellar) astronomers: stars are, at a first approximation endowed by spherical symmetry. *Unification of fundamentally identical but apparently disparate classes is an essential precursor to understanding the underlying physical, intrinsic properties of AGNs.* (Paolo Padovani in Chapter 3 of D'Onofrio et al. 2012). The sketch of Fig. 9 shows in a schematic way the three principal physical drivers of unification:

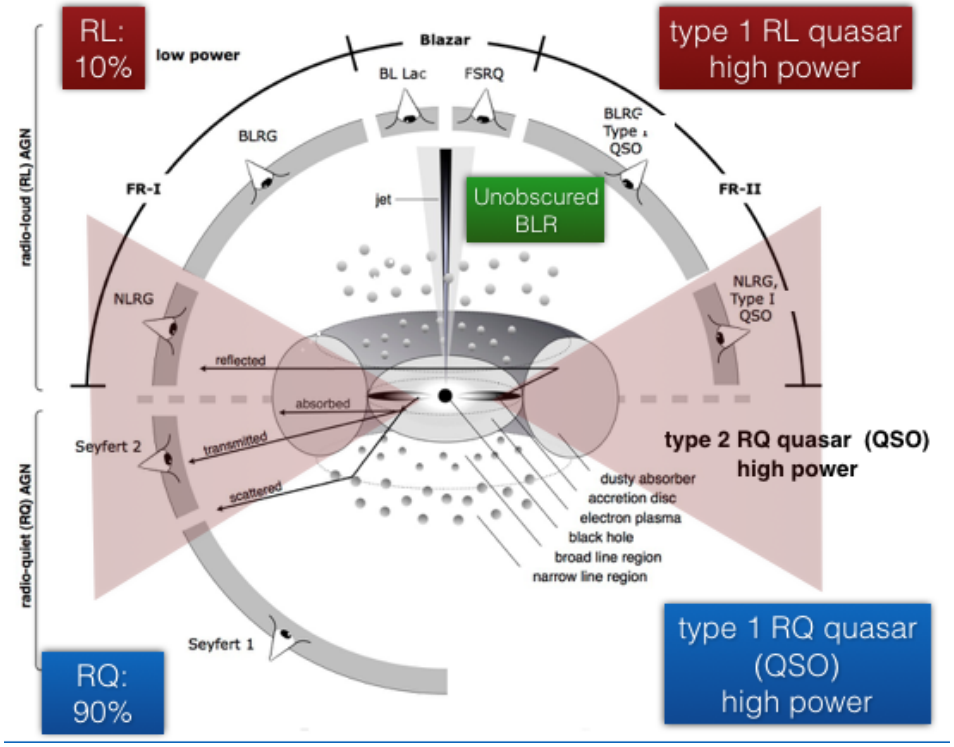

Figure 9: A synthetic sketch illustrating the Unification scheme for RL and RQ AGN. From

- luminosity; the first "unification" is in luminosity: Seyfert galaxies and quasars are nowadays considered to be the low- and high-luminosity segments of the same physical process, accretion on a supermassive BH. They are low- and high-luminosity AGN, respectively. We will extensively use the term quasar to indicate high-luminosity type-1 AGN.

- obscuration due to viewing angle of the central engine by a thick structure (a dense molecular torus), that gives rise to the distinction between type-II and type-I AGNs (Khachikian & Weedman 1974; Antonucci & Miller 1985). We expect strong signatures of the hot dust emission in the mid- and far-IR. The circumnuclear dust predicted by the model is illuminated by the intense radiant field of the nuclear source, absorbs the UV photons emitted in the direction of the torus, heats up, and then reradiates this absorbed energy like a blackbody process at the grain equilibrium temperature (A. Franceschini in Chapter 3 of D'Onofrio et al. 2012). Infrared observations have basically confirmed this scenario.

- relativistic Doppler boosting, that operates in RL AGN, where relativistic ejections are observed in the radio domain (Urry & Padovani 1995, and references therein). For RL quasars there is a distinctive radio morphology difference at low- and high-luminosity. Low-luminosity (so-called Fanaroff-Riley type I [FR I]) and high- luminosity (FR II) radio galaxies have been unified with BL Lacs and radio quasars, respectively. I BL Lacs are thought to be FR I radio galaxies with their jets at relatively small ($\lesssim$ 20–30 deg) angles with respect to the line of sight. Flat-spectrum radio quasars (FSRQs), defined by their radio spectral index at a few GHz close to 0, are FR II radio galaxies oriented at small (< 15) angles, while steep spectrum radio quasars (spectra index above 0.5) should be at angles in between those of FSRQ and FR IIs. Blazars include BL Lacs and FSRQs show absence of strong, broad lines, are and then should have their jets closely oriented toward the observer.

Unification schemes have provided a powerful conceptual framework suitable for organizing the analysis of AGN. The precursor distinction between type 1 and 2 Seyfert (Khachikian & Weedman 1974) gained a convincing interpretation when Antonucci & Miller (1985) reported the discovery of a broad line component visible in the polarized spectrum of Seyfert 2 nuclei but invisible in natural light: the broad line region is hidden from view by a geometrically thick-structure and only photons scattered by hot electrons toward our line of sight are received by the observer. This explanation remains widely accepted today (e.g., Eun et al. 2017), even if we now know that is only a part of the story: type-2 AGN differ for environmental properties (Dultzin-Hacyan et al. 1999; Villarroel & Korn 2014), may intrinsically lack a BLR (Laor 2000) at very low accretion rates, or may even be unobscured normal type-1 under special conditions (Marinucci et al. 2012). The point here is that unification models of RQ AGN make no prediction on unobscured type 1 AGN. Orientation effects are expected also for unobscured type-1s, as we should observe them in the range of angles $0 \lesssim \theta \lesssim 45 - 60$ between the line of sight and the symmetry axis (i.e., the spin axis of the black hole or the angular momentum vector of the inner accretion disk). There is little doubt that line width is affected by orientation, especially for RL sources (e.g., Wills & Browne 1986; Rokaki et al. 2003; Sulentic et al. 2003; Jarvis & McLure 2006; Runnoe et al. 2014). For RQ objects, the evidence is not obvious and an estimate of θ remains an unsolved problem at the time of writing.

We will not further considering RL sources nor type-II AGN in the following, as our

thesis is focused exclusively on type-I quasars.

2.2 Type-I AGN

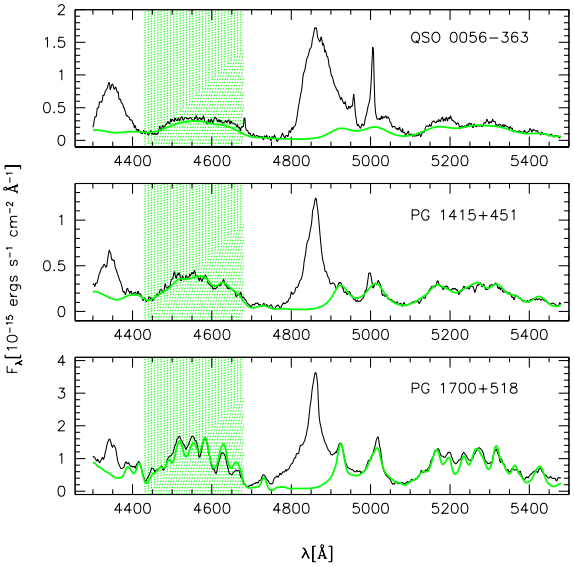

Figure 10: Three type-1 quasars. The green line represents the FeII emission template, scaled and broadened to fit the observed FeII emission. The shaded area between 4340 and 4680 Å covers the wavelength range used to compute the total intensity of the blended emission at 4570 Å to estimate the relative intensity between FeII λ 4570 and Hβ i.e., the RFE parameter (§2.4.2). The three spectra show different RFE: as the intensity ratio decreases, the line width increases. Also notable is the change in profile shape of Hβ. The spectra of the three quasars are exemplary of general trends involving LILs observed along the quasar main sequence.

We will restrict the attention to two subtypes of type-I AGN (examples of three spectra of type-I AGN are shown in Fig. 10) which are especially relevant for our thesis work.

Seyfert 1s with relatively narrow broad lines are sometimes referred to as narrow-line Seyfert 1s (NLSy1s). The formal limit of NLSy1s is at FWHM(Hβ) = 2000 km s^{-1}(Osterbrock & Pogge 1985), but it is unlikely to be of physical meaning. NLSy1s will be discussed later in the context of Pop. A.

Since strong and broad emission lines are a hallmark of quasar opticalUV spectra, the discovery of about 50 Sloan Digital Sky Survey (SDSS) quasars at $z \sim 2.7-5.9$ with extremely weak or undetectable emission lines (hereafter WLQs). WLQs exhibit EW(Lyα+N vλ1240) < 10 Å (Diamond-Stanic et al. 2009). Since WLQs exhibit typical quasar UV continua with no signs of broad C IV absorption, they are unlikely to be dust- obscured or broad-absorption line quasars (see, e.g., Anderson et al. 2001; Collinge et al. 2005). In addition, Shemmer et al. (2010) have argued against the possibility that these sources are high-redshift galaxies with apparent quasar-like luminosities due to gravitational-lensing amplification. Shemmer et al. (2010) suggested that the two most likely interpretations for the weakness of the HILs are either a relativistically boosted continuum or, alternatively, physical suppression of the

HILs.

2.3 Evolution and luminosity effects of type-I quasars

In the following discussion, we rely on the paper by Fraix-Burnet et al. (2017). Every quasar is the direct descendant of a seed black hole. However, black holes of masses $M_{\rm BH} \lesssim 10^5$ M$_\odot$ are extremely difficult to detect if they are placed in the nuclei of external galaxies. Even if they are radiating at $L/L_{\rm Edd}\sim$ 1, their apparent V magnitude will be $\approx$ 22 at redshift $z \approx 0.3$. In flux-limited quasar samples at low-z, we detect quasars in the mass range $6 \lesssim \log M_{\rm BH} \lesssim 8$ radiating close to their Eddington limit. The masses of these sources are clearly not the masses of the fledgling seed BHs. Nonetheless, in the local Universe, the only sources radiating close to the Eddington limit are these relatively low-$M_{\rm BH}$ quasars. It is easy to see that, if the most massive black holes were nowadays radiating at their maximum radiative power per unit mass ($\approx 2\ L/L_{\rm Edd}$), they would be almost visible to the naked eye (with $M_{\rm BH} \approx 10^{10}$ M$_\odot$ at $z \approx 0.15$ it would be $m_{\rm V} \approx 6.7$!) (D'Onofrio & Burigana 2009). The absence of massive BHs radiating close to the Eddington limit is associated with the overall downsizing of the star formation and nuclear activity at recent cosmic epochs (e.g., Fontanot et al. 2009; Reviglio & Helfand 2009; Hirschmann et al. 2014). The very massive black holes that were extremely luminous mostly belong now to spent systems (Lynden-Bell 1969), accreting at a very low rate. In this respect sources like Messier 87 (a prototypical "spent" quasar which is hosting one of the most massive BHs in the local Universe, Walsh et al. 2013) are different from the quasars that we see active today (Fraix-Burnet et al. 2017).

Recent deep observations of faint quasars ($m_{\rm V} \sim 22$) obtained with GTC indicate the presence of a slowly evolving quasar Population at $z \approx 2$, not dissimilar to the one observed at low-z as far as the frequency of Pop. B sources is concerned (Sulentic et al. 2014). This result is consistent with the existence of a population of sources that were evolving on timescales much shorter than the Hubble time, then (at a cosmic age of just $\approx$ 3 Gyr) and now, and with the relatively short lifetimes expected for quasars (Kelly et al. 2010).

Fraix-Burnet et al. (2017) report that Mathur (2000) and, independently, Sulentic et al. (2000a) suggested that the local-Universe NLSy1 sources accreting at a high rate are reminiscent of the early quasars. We are still far from detecting the first population of "infant"

quasars without "adults" (a feat that may never become possible). Unfortunately, at high z it is still not possible to detect black holes of $M_{\rm BH}$~ 10^7 $M_\odot$, even if they are radiating at or slightly above $L/L_{\rm Edd}$, as there is a redshift-dependent cut-off in the detectable $L/L_{\rm Edd}$ (Sulentic et al. 2014). Our view of quasars is biased (Fig. 11 and 12).

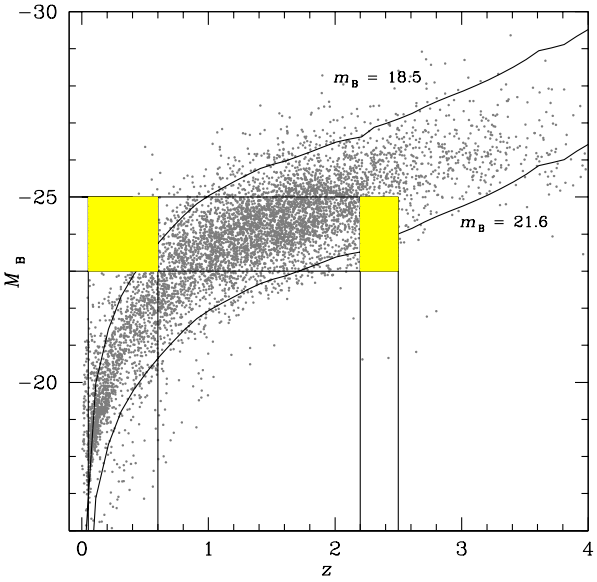

Figure 11: Absolute magnitude of quasars vs. redshift for the SDSS-based catalog of (Schneider et al. 2010). Curves are computed for two limiting (K-corrected) apparent magnitudes m_B = 18.5 and m_B = 21.6. The shaded boxes identify the loci in the $z - M_B$ planes of two volume-limited samples within the same luminosity limits: one between $2.2 \leq z \leq 2.5$ as for the sample of Sulentic et al. (2014), and a control sample at $0.05 \leq z \leq 0.6$.

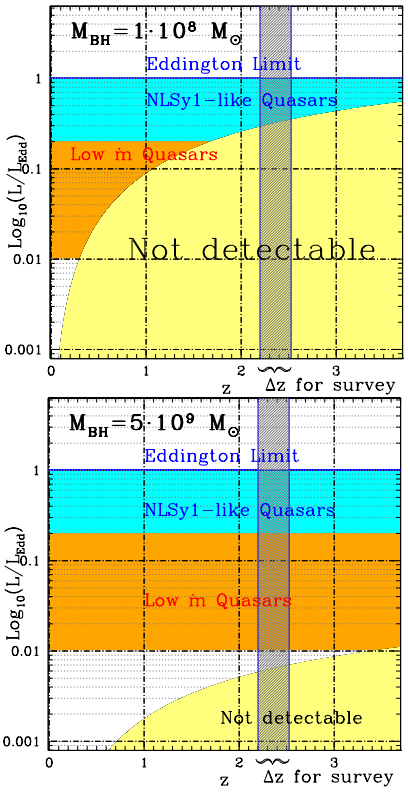

Figure 12: *Eddington ratio bias* as a function of redshift, with the area of undetectable sources below a limiting magnitude $m \approx 21.5$) in yellow, for two fixed value of the black hole mass. The redshift range of the quasar survey carried out by Sulentic et al. (2014) is identified by the dashed grey strip. Quasars radiating at higher $L/L_{\rm Edd}$ $\gtrsim$ 0.2 occupy the pale blue shaded area, while lower radiators are in the orange strip. Note that all sources above $L/L_{\rm Edd} \gtrsim 0.01$ are detected in the high mass case up to redshift 4, all lower radiators are lost for the low mass case in the redshift range of the survey.

2.4 Organization of large quasars samples

2.4.1 Principal Component Analysis

Eigenvector techniques are applied whenever many variables appear to be more or less loosely correlated without an intuitive indication of a dominant correlation or variable. A set of n objects may have m measured parameters like flux, FWHM, and equivalent widths of optical and UV emission lines, continuum shape, etc. Each set of measurement is a vector in an m-dimensional space described by orthogonal vectors $\overrightarrow{v}$, and define a matrix M of n vectors with m measurements. The *Principal Component Analysis* (PCA) searches for the best-fitting set of orthogonal axes to replace the original m axes in the space of measured parameters. The new axis set is sought by maximizing the sum of the squared projections onto each axis, i.e. $(M\overrightarrow{v})^{\mathrm{T}}(M\overrightarrow{v})$, where M^{T} denotes the transposed matrix. If the set of measurement has been previously centered subtracting the variable average, then $M^{\mathrm{T}}M$ can be thought as a variance/covariance matrix. We seek the maximum of $\overrightarrow{v}M^{\mathrm{T}}M\overrightarrow{v}$ with the condition that the norm of $\overrightarrow{v}$ is unity. We can impose the condition through a Lagrange multiplier λ, and set the first derivative to 0 to find the maximum sought: $\overrightarrow{v}^{\mathrm{T}}M^{\mathrm{T}}M\overrightarrow{v} - \lambda(\overrightarrow{v}^{\mathrm{T}}\overrightarrow{v} - 1)$, hence $2M^{\mathrm{T}}M\overrightarrow{v} - 2\lambda\overrightarrow{v} = 0$, and then $M^{\mathrm{T}}M\overrightarrow{v} = \lambda\overrightarrow{v}$. This is an eigenvalue equation, which can be solved numerically. More eigenvectors are sought through a similar procedure, with the additional constraints that the eigenvectors must be orthogonal to each other. Since the eigenvalues are a measurement of the sum of the squared projections of the original data vectors on the new normalized vectors, and since we assume to have set as a covariance matrix $M^{\mathrm{T}}M$, the eigenvalues are a measurements of the amount of variance carried in each new direction. For example, in a plane we can imagine a set of almost aligned points; their projections in the original axes may be nearly equal if they are not aligned preferentially with anyone of the two axes of the two original frame. We may think of two variables that are highly correlated. We can maximize the projections along one axis by simply operating a rotation of the reference frame. A linear combination of the two original variables (or vectors) will now constitute the one vector that is needed to account for the variance of the data. A key aspect of the power of the PCA emerges from this simple example: a problem originally treated in two dimensions was inherently one-dimensional, i.e., a PCA can restore a problem with a very large set of variables to its intrinsic dimensionality.

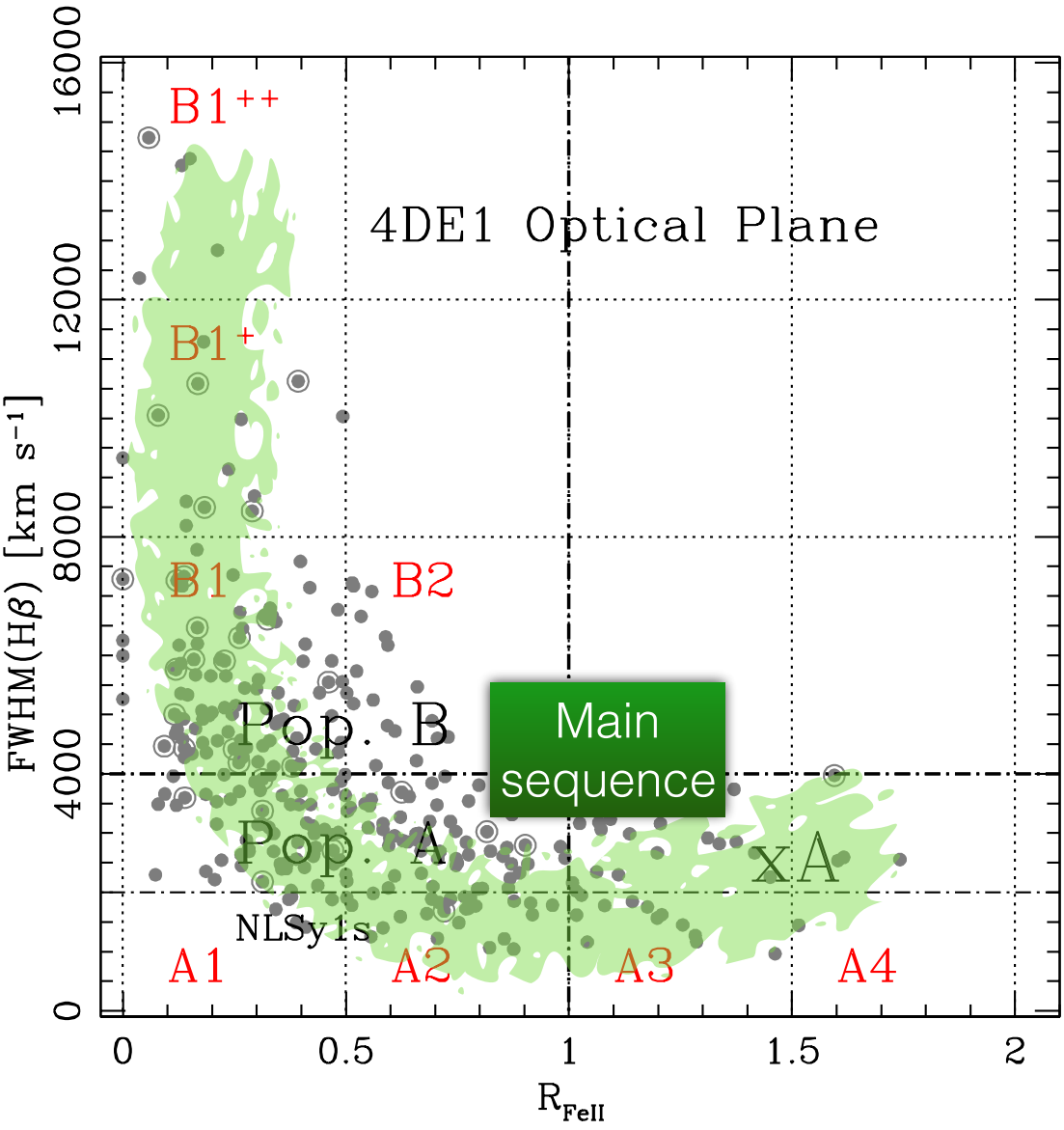

Figure 13: The optical plane of the Eigenvector 1, FWHM(Hβ) vs. R_{FeII}. The green shaded area indicatively trace the distribution of a quasar sample from Zamfir et al. (2010), defining the quasar MS. The thick horizontal dot-dashed line separates populations A and B; the thin identifies the limit of NLSy1s. The vertical dot-dashed line marks the limit for extreme Population A (xA) sources with $R_{FeII} \gtrsim 1$. Dotted lines separate spectral types, identified as explained in §2.4.2.

2.4.2 The quasar Main Sequence

At the time the Boroson & Green (1992) paper appeared, studies based on moderately sized samples (20-30 objects) were common and often reached confusing results from correlation analysis. The best example is the Baldwin effect which was found in some and then not

found in similar samples without apparent explanation. In this sense the sheer size of the Boroson & Green (1992) sample was a key improvement. The application of PCA was not unprecedented in extragalactic astronomy (e.g. Diaz et al. 1989) but was well suited to quasar data that appeared weakly correlated among themselves without providing a clear insight of which correlations were the most relevant ones.

The quasar Eigenvector 1 was originally defined by a PCA of ≈ 80 PG quasars and associated with an anti-correlation between strength of FeIIλ4570, R_{FeII} (or [OIII] 5007 peak intensity) and FWHM of Hβ. The parameter R_{FeII} is defined as the intensity of the FeIIλ4570 blend of multiplets normalized to the one of Hβ broad component:[1] R_{FeII}= I(FeIIλ4570)/I(Hβ). Since 1992, various aspects of the Eigenvector 1 (E1) of quasars involving widely different datasets as well multi-frequency parameters have been discussed. Earlier analyses have been more recently confirmed by the exploitation of SDSS-based samples (Yip et al. 2004; Wang et al. 2006; Zamfir et al. 2008; Richards et al. 2011; Kruczek et al. 2011; Marziani et al. 2013b; Shen & Ho 2014; Sun & Shen 2015; Brotherton et al. 2015).

The second eigenvector – Eigenvector 2 – was found to be proportional to luminosity, and eventually associated with the HIL Baldwin effect(s) that are the most-widely discussed luminosity effects in quasar samples (Baldwin et al. 1978; Dietrich et al. 2002; Bian et al. 2012). The smaller fraction of variance carried by the Eigenvector 2 indicates that luminosity is not the major driver of quasar diversity, especially if samples are restricted to low-z. We will not further consider HIL luminosity effects[2].

The distribution of data points in the optical plane of the Eigenvector 1 FWHM(Hβ) vs. R_{FeII} traces the quasar main sequence (MS, Fig. 13). The MS shape allows for the definition of a sequence of spectral types (Fig. 13), and motivates subdividing the 4DE1 optical plane into a grid of bins of FWHM(Hβ) and FeII emission strength. Bins A1, A2, A3, A4 are defined in terms of increasing R_{FeII} with bin size ΔR_{FeII}= 0.5, while bins B1, B1+, B1++, etc. are defined in terms of increasing FWHM(Hβ) with ΔFWHM = 4000 km s^{-1}. Sources belonging to the same spectral type show similar spectroscopic measurements (e.g., line profiles and line flux ratios). Spectral types are assumed to isolate sources with similar

[1]The term broad component without the suffix BC is used here to identify the full broad profile excluding the Hβ narrow component. In more recent times, we have distinguished between Hβ_{BC} and Hβ_{VBC}, the former being associated with the broad core of the Hβ broad line.

[2]HIL luminosity effects are subject to strong biases. It is as yet unclear whether such biases can entirely account for the weak luminosity effects observed in large samples.

broad line physics and geometry. Systematic changes are reduced within each spectral type (albeit not eliminated, if an interpretation scheme such as the one of Marziani et al. (2001) applies). If so, an additional advantage is that an individual quasar can be taken as a bona fide representative of all sources within a spectral type. The binning adopted (see Fig. 13) has been derived for low-z (< 0.7) quasars.

Developments in the analysis before late 1999 of low-z quasar spectral properties are reviewed in Sulentic et al. (2000a). Data and ideas were in place as early as in year 2000 to introduce the idea of two quasar populations, A and B: Population A with FWHM(Hβ) $\lesssim$ 4000 km s^{-1}; Population B(broader) with FWHM(Hβ) $\gtrsim$ 4000 km s^{-1} (Sulentic et al. 2000a,b). Later developments have confirmed that the two populations are two distinct quasar classes.

2.4.3 Multifrequency correlations of the quasar MS

Several correlates that have been proved especially relevant in the definition of the MS multifrequency properties.

- **Balmer emission line profile shape** There is a clear distinction between Pop. A and B in terms of Balmer line profile shapes: Pop. A sources show Lorentzian Balmer line profiles, symmetric and unshifted; Pop. B, Double Gaussian (broad + very broad component, H$\beta_{\rm BC}$ + H$\beta_{\rm VBC}$), most often redward asymmetric. While several authors described the Balmer line profiles of NLSy1s as Lorentzian (e.g., Véron-Cetty et al. 2001; Cracco et al. 2016), the transition between the profile types is apparently occurring at 4000 km s^{-1} and not at 2000 km s^{-1}, the canonical limit of NLSy1. This early result (Sulentic et al. 2002) has been confirmed by several later analyses (e.g., Zamfir et al. 2010; Marziani et al. 2013b; Negrete et al. 2017). Fig. 14 shows composite spectra in the FWHM range 2000 – 4000 and 0 – 2000 km s^{-1}: the profile shape remains the same as the line gets broader (Negrete et al. 2017). Mirroring the Paolo Padovani's prescription as enunciated at the Padova meeting (no more RL, only jetted!), we would recommend to speak of Population A and B... and no more NLSy1s! In both cases, it is not just a matter of nomenclature: inter-sample comparison will be biased if the subdivision is inappropriate.

- **UV diagnostic ratios** Major trends involve strong UV emission lines. Schematically, moving from spectral type B1++ to A4 we find: NVλ1240/Lyα: $\nearrow$; AlIIIλ1860/SiIII]λ1892: $\nearrow$ CIII]λ1909/SiIII]λ1892 $\searrow$ W(NIII]1750) $\nearrow$ W(CIVλ1549) $\searrow$. These trends can be interpreted as an increase in density and metallicity and decrease in ionization parameter toward the strongest FeII emitters at the tip the E1 sequence (Baldwin et al. 1996; Wills et al. 1999; Bachev et al. 2004; Nagao et al. 2006; Negrete et al. 2012, 2013).

- **CIVλ1549 centroid shifts** The CIV1549 centroid blueshifts are a strong function of a source location along the E1 MS, reaching maximum values in correspondence of the extreme Pop. A (xA, spectral types A3 and A4). They can be accounted for by a scaled, almost symmetric and unshifted Hβ plus an excess of blueshifted emission, corresponding to a "virialized" emitting region plus an outflow/wind component (Marziani et al. 2010). The relative prominence of the two components is a function of the location on the MS: the outflow component can dominate in xA sources , and be undetectable in sources at the other end of the MS (B1++), where the broader profiles are found. If we measure the centroid shift at half maximum $c(\frac{1}{2})$, large blueshifts are found only in Pop. A (Sulentic et al. 2007). The blue shifted excess is at the origin of a correlation between centroid shifts of CIVλ1549 and FWHM CIV (Coatman et al. 2016; Sulentic et al. 2017). This has important implications for $M_{\rm BH}$ estimates.

- **[OIII] blueshifts** The [OIII]$\lambda\lambda$4959,5007 doublet mimics the blueshift observed for CIVλ1549 with respect to the rest frame. The average blueshift amplitude increases toward the high $R_{\rm FeII}$ end of the MS (Zamanov et al. 2002; Marziani et al. 2003a; Zhang et al. 2013; Cracco et al. 2016). This is emphasized by the distribution of the "blue outliers" (BOs) in [OIII]$\lambda\lambda$4959,5007 which show blueshift at peak of amplitude $\gtrsim$ 250 km s^{-1}. Large [OIII] shifts such as the ones of the BOs are found for FWHM(Hβ)< 4000 km/s.

- **LIL blueshifts** The profile of the resonance LIL MgIIλ2800 also suggests evidence of outflow (somewhat unexpectedly, Marziani et al. 2013b,a): low ionization outflows are detected in the xA spectral types, but lower radial velocities are involved in MgII λ2800 than in CIVλ 1549 ($\sim$ 100 vs. $\sim$ 1000 km/s).

- **Radio loudness** The probability of being RL is much larger among Pop. B sources: 25%, among Pop. A $\approx 3-4\%$. Core-dominated RL sources are displaced toward Pop. A in the optical plane of the E1 because of orientation effects. Zamfir et al. (2008) suggest that RL sources should be considered as such only if very powerful with $\log P_\nu > 31.6$ [erg s^{-1} Hz^{-1}], and Kellerman's $\log R_{\rm K} > 1.8$ (Kellermann et al. 1989), in line with the distinction of jetted and non-jetted suggested by Padovani (2016) which considers as jetted only sources for which there is evidence of powerful, relativistic ejections.

- **Soft X-ray slope** The steepness of the soft X-ray continuum measured by the photon index $\Gamma_{\rm soft}$ is also dependent on the location along the MS. $\Gamma_{\rm soft}$ is the measure of the soft-X excess (0.2 - 2 KeV) above a canonical power law with $\Gamma \approx 2$. Values of $\Gamma_{\rm soft} > 2$ are mainly found for FWHM(Hβ) < 4000 km/s (Pop.A) (Boller et al. 1996; Wang et al. 1996; Sulentic et al. 2000a; Grupe 2004; Bensch et al. 2015).

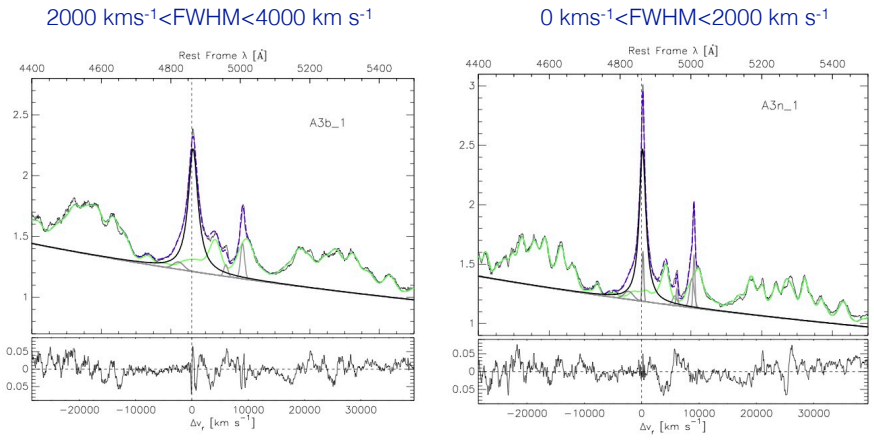

Figure 14: Fits of the A3 spectral type composites, obtained for the broader and narrow half of the spectral bin. The original spectrum (thin black line) is shown with FeII emission (pale green) superimposed to the continuum and the Hβ line with a Lorentzian profiles (thick black lines). Thin grey lines trace H$\beta_{\rm NC}$ and [OIII] emission and, on the blue side of Hβ, a faint excess emission that is not accounted for by the symmetric shape of Hβ.

Tables reporting main-sequence correlates are provided in several recent reviews and research papers (e. g. Sulentic et al. 2011; Fraix-Burnet et al. 2017), and in Chapter 3 and 6 of D'Onofrio et al. (2012).

2.4.4 Four Dimensional Eigenvector 1 (4DE1) scheme

To restrict the attention of a subset of especially significant parameters, Sulentic et al. (2000a) introduced a 4D E1 parameter space. In addition to FWHM(Hβ) and R_{FeII}, two more observationally "orthogonal" parameters, Γ_{soft} and $c(\frac{1}{2})$ CIVλ1549 are meant to help establish a connection between observations and physical properties. The 4DE1 parameters clearly support the separation of Population A (FWHM Hβ<4000 km s^{-1}) and Population B(roader) sources,[3] although the non-optical parameters are not always useful since they are MS correlates and often unavailable. The immediate interpretation of the 4DE1 parameters is summarized in Table 2. In the simplest term, the FWHM Hβ is related to the velocity dispersion in the LIL emitting part of the BLR. On the converse, $c(\frac{1}{2})$ CIV yields a measurement affected by the high-ionization outflow detected in the HIL profile. The largest $c(\frac{1}{2})$ values indicate a decoupling between the strongest HIL and LIL features, with the latter remaining symmetric and unshifted (Marziani et al. 1996). The parameter R_{FeII} is of more complex interpretation. R_{FeII} is affected by the metallicity (obviously, if [Fe/H]=0, R_{FeII}=0) but metallicity is most likely not all of the story (Joly et al. 2008), since FeII strength tends to saturate for high metallicity values. The main dependence is probably on ionization conditions, density and column density. A $\Gamma_{soft} > 2$ is usually ascribed to Compton thick soft X-ray emission, but may be even the high-energy tail of the bare accretion disk emission, if the inner disk is very hot (e.g., Done et al. 2012; Wang et al. 2014).

[3]The 4000 km/s limit is valid at low and moderate luminosity $\log L \lesssim 47$ [erg/s].

Chapter 3

Quasars and their cosmological application

3.1 Cosmology with standards candles

A standard candle needs to have a known, well-defined luminosity with a small intrinsic dispersion around an average value. Alternatively, standard candle should be based on a calibration of a measurable property that tightly correlates with luminosity. Useful standard candles in a cosmological context should be easily recognizable and intrinsically luminous. In this Chapter we will first present how the Hubble diagram can be computed, and the mention the results obtained from supernovæ. We will then introduce the topic of quasars as distance indicators.

3.1.1 The Hubble diagram

Following Perlmutter et al. (1997) the luminosity distance can be written as:

$$d_L(z;\Omega_M,\Omega_\Lambda,H_0) = \frac{c(1+z)}{H_0\sqrt{|\kappa|}} \quad S\left(\sqrt{|\kappa|}\int_0^z \left[(1+z')^2(1+\Omega_M z') - z'(2+z')\Omega_\Lambda\right]^{-\frac{1}{2}} dz'\right), \tag{3.1}$$

where Ω_M is the energy density associated to matter and Ω_Λ the energy density associated to Λ, and . If $\Omega_M + \Omega_\Lambda > 1$, $S(x)$ is defined as $\sin(x)$ and $\kappa = 1 - \Omega_M - \Omega_\Lambda$; for $\Omega_M + \Omega_\Lambda < 1$, $S(x) = \sinh(x)$ and κ as above; and for $\Omega_M + \Omega_\Lambda = 1$, $S(x) = x$ and $\kappa = 1$.

The luminosity distance $d_L = d_C \cdot (1+z)$ can be computed as follows

$$d_C = d_H \int_0^z \frac{dz'}{E(z')} \tag{3.2}$$

with

$$D_H \equiv \frac{c}{H_0} = 3000\, h^{-1}\ \mathrm{Mpc} = 9.26 \times 10^{25}\, h^{-1}\ \mathrm{m} \tag{3.3}$$

with $\log\ d_H \approx 28.12$ and

$$E(z) \equiv \sqrt{\Omega_M\,(1+z)^3 + \Omega_k\,(1+z)^2 + \Omega_\Lambda} \tag{3.4}$$

The equation of Perlmutter et al. (1997) has been obtained by simply posing $\Omega_k + \Omega_\Lambda + \Omega_M = 1$, where Ω_k is the energy density associated with the curvature of space-time.

The *distance modulus* DM is defined by

$$DM \equiv 5\,\log\left(\frac{d_L}{10\ \mathrm{pc}}\right) \tag{3.5}$$

$$\mu = 5 \log d_L(H_0, \Omega_M, \Omega_k, \Omega_\Lambda, z) + 5, \tag{3.6}$$

(+25 if distances are measured in Mpc).

The Hubble diagram with the supernovæ is shown with the data that were available at the end of the 1990s is shown in Fig. 15. They allowed an inference of $\Omega_\Lambda > 0$, i.e., of the accelerated expansion of the Universe.

3.1.2 Concordance cosmology from supernovæ

Only few Supernovæ at $z \gtrsim 1$ had been discovered by year 2000. At that time the Hubble diagram with type Ia supernovæ showed a large scatter, although the supernova data points appeared systematically fainter than expected (Fig. 15). The observations sampled mainly the redshift interval where the effect of nonzero Λ yields an accelerated expansion (Perlmutter et al. 1997, 1999). Supernova surveys have produced and analysed data for ≈ 500 supernovæ (Conley et al. 2011), although the wide majority are still at $z \lesssim 1$. In addition the WMAP 9 yr combined results and the Planck probe results indicate that Ω_M and Ω_Λ

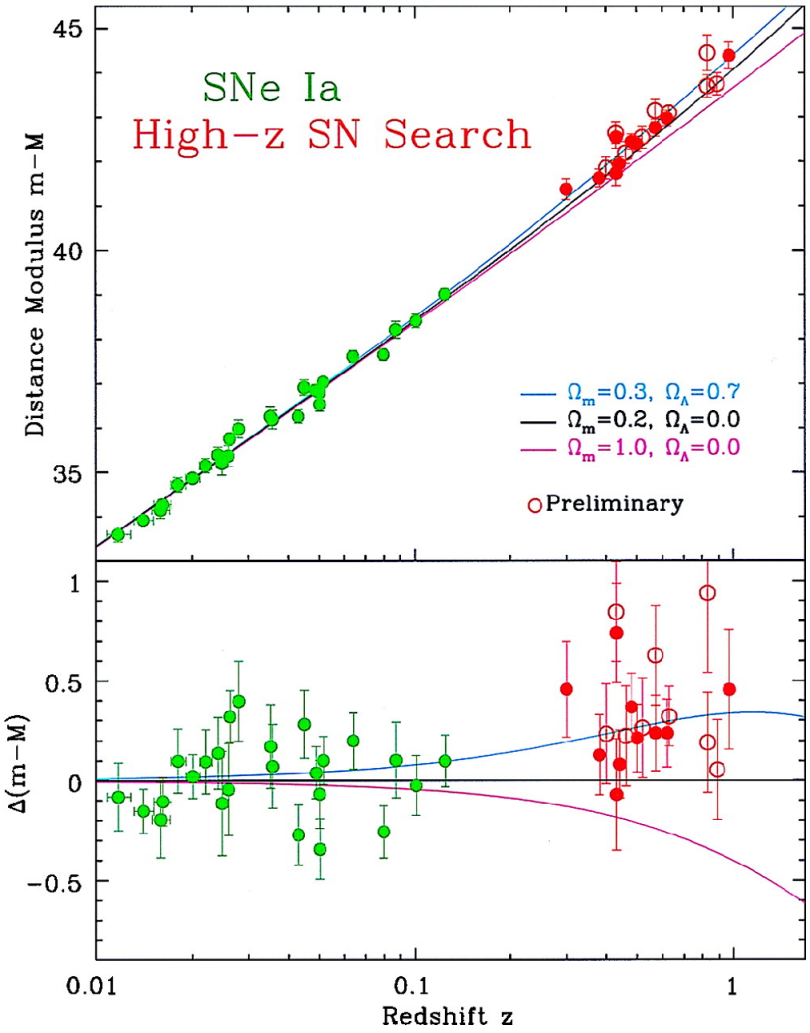

Figure 15: The Hubble diagram for SN Ia. The lines show the predictions for cosmologies with varying amounts of Ω_M and Ω_Λ. The observed points all lie above the line for a universe with zero Λ. The lower panel, with the slope caused by the inverse square law taken out, shows the difference between the predictions more clearly and shows why a model with $\Omega_\Lambda > 0$ is favored. Reproduced from Kirshner (1999).

are known with an accuracy of a few percent. Surveys are planned to improve the precision down to 1-percent level.

3.2 Quasars as distance indicators

Two properties of standard candles are met by quasars: they are easily recognizable and highly luminous. Quasars emit a fairly univocal spectrum, with prominent broad emission lines in the optical and UV range. And they can be very, very luminous: their absolute magnitude reaches $M_B \approx -30$, which corresponds to a luminosity 10,000 times the one of Messier 31, the Andromeda galaxy.

However, if type-1 quasars can be the most luminous sources in the universe that can be stable over periods of several years (as opposed to *Gamma Ray Bursts*), they can also be comparatively faint: the nucleus of NGC 4395 hosts the least luminous quasar known: its $M_{\rm B} \approx$ -10 is just 10 times the luminosity of a typical blue supergiant star. Quasars can have all luminosities in between the two extrema (which are a factor 10^8 apart), with a luminosity function that is open-ended at low luminosity. No class of quasars has a luminosity distribution peaked around a constant average value.

Fig. 16 shows three spectra of quasars of widely different redshift and luminosity, even if the comparison is restricted to a narrow range around the HI Balmer line Hβ. The spectra show clearly that a very luminous quasar can look like a bright, nearby Seyfert galaxy. There is no discontinuity in the luminosity distribution between AGN and quasars.

In addition, *Quasars are anisotropic sources.* Two main effects contribute to anisotropy: relativistic beaming in radio-loud sources, and obscuring material co-axial with the accretion disk in both radio-loud and radio-quiet AGN, as we have reviewed in Chapter 2.

The previous considerations highlight why quasars are difficult if one thinks of their potential use for measuring fundamental cosmological parameters like the Hubble constant H_0, $\Omega_{\rm M}$ and Ω_Λ. They are a class of sources whose luminosity is spread over an enormous range in luminosity, and whose spectral properties are fairly similar over a large range of redshift, basically from local $z \approx 0$ Seyfert 1 nuclei to the most distant quasars at $z > 6$. Nonetheless, quasars are so numerous that is highly desirable to look for parameters that we can easily measure and that tightly correlate with luminosity, if they exist.

If there is an intervening galaxy between us and the quasar, and especially if the galaxy is not perfectly aligned with the quasar along our line of sight, the galaxy acts as a gravitational lens yielding multiple, asymmetrically displaced images of the quasar. One measures different time delays for the displaced images due to the path-length difference between the quasar and the earth, and also the gravitational effect on light rays traveling in slightly different potential wells.It is possible to compute H_0. The H_0 value is usually below or in agreement Schechter (2005) with the value obtained from the Cepheids, $H_0 = 72 \pm 8$ km s^{-1} Mpc^{-1}. We will not discuss the method further since it does not deal with intrinsic properties of quasars.

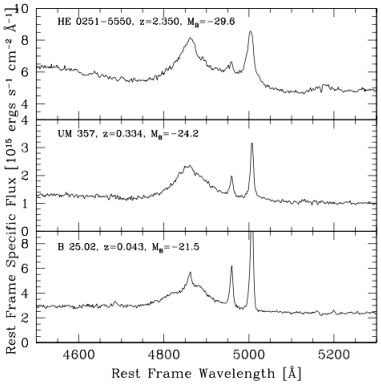

Figure 16: The spectra of three quasars of widely different luminosity and redshift, covering the broad hydrogen Balmer Hβ line and the narrow, forbidden [OIII]$\lambda\lambda$4959,5007 lines. HE 0251-5550 is ≈2,000 times more luminous than B 25.02. B 25.02 is a local Seyfert 1 galaxy, while HE 0251-5550 is a distant quasars. From D'Onofrio & Burigana (2009).

3.2.1 Luminosity correlations

J. Baldwin and co-workers noticed almost 40 years ago an inverse correlation between the equivalent width of the CIVλ1549 emission line and the apparent luminosity of bright quasars (Baldwin et al. 1978). In other words, the lines become less prominent over the underlying continuum with increasing luminosity. The effect was believed to be to be very strong and with a straightforward application to cosmology, with the equivalent width of CIVλ1549 decreasing proportionally to $L^{-\frac{2}{3}}$. The *Baldwin effect* as presently found in large samples is a weak and loose anti-correlation between specific luminosity and high-ionization lines equivalent width (Bian et al. 2012). Results until mid-1999 have led to a standard scenario in which the slope of the Baldwin relationship between logarithm of equivalent width of CIVλ1549 (the most widely studied high-ionization line) and luminosity is ≈ –0.15. The Baldwin effect occurs in all measurable high-ionization lines except NVλ1240, and the slope of the anticorrelation increases with the energy of the ionic species (Dietrich et al. 2002). These results have been basically confirmed by more recent studies based on large quasar samples (Bian et al. 2012). The anticorrelation of CIVλ1549 remains very weak. In addition, it has been suggested that the Baldwin correlation may mainly reflect the combination of a strong Eddington ratio dependence and selection effects Bachev et al. (2004). Sources with low low CIVλ1549 equivalent width which including NLSy1s are the ones radiating at higher Eddington ratio (Fig. 17).

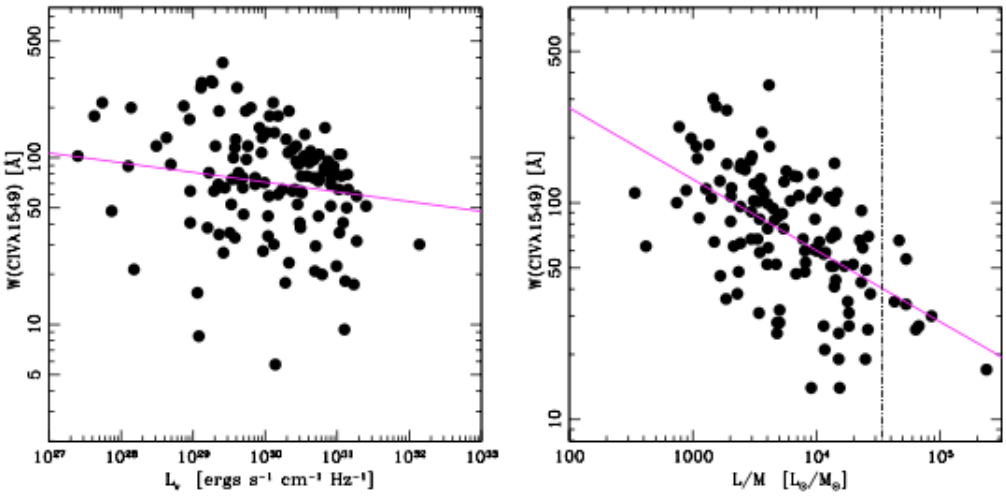

Figure 17: Left panel: the weakness of the Baldwin effect in a sample of low-z quasars for which measurements of the CIVλ1549 high ionization line come from archived HST observations (Sulentic et al. 2007). Abscissa is the specific luminosity; ordinate is the rest-frame equivalent width of CIVλ1549. Right panel: the Eddington ratio dependent "Baldwin effect", for quasars with black hole mass estimated from the Hβ line width. The abscissa is the luminosity to mass ratio expresses in solar units. $\log L/M \approx 4.53$ corresponds to unity Eddington ratio (dot-dashed vertical line). The inverse correlation with Eddington ratio is much stronger than the one with luminosity. From D'Onofrio & Burigana (2009).

3.2.2 New methods depeveloped in the last five years

New developments are paving the road to the use of quasars as distance indicators (Fig. fig:methods lists several methods that we will be discussed in this Chapter) . The MS organizes the diverse quasar properties and makes it possible to identify quasars in different accretion states. Even if major observational constraints indicate powerful high-ionization wind, part of the broad line emitting regions remains "virialized." In other words, a virialized low-ionization broad emission line region present even at the highest quasar luminosities, and coexists with high ionization winds (Sulentic et al. 2017).

The physical foundation of xA-based methods is the Eddington ratio "asymptotic" behavior expected from optically thick ADAFs for dimensionless accretion rates $\gg 1$.

3.2.3 The method of La Franca et al. (2014)

La Franca et al. (2014) propose a new method to predict the AGN luminosity based on the combination of the virial $M_{\rm BH}$ expression that requires the AGN luminosity and the broad line width and the anti-correlation between MBH and the X-ray variability amplitude.

The $M_{\rm BH}$ estimates are based on the virial relation $\log M_{BH} = \alpha \log L + \beta \log \delta v + \gamma$,

Sources	Parameters	Basic equation	Reference	Virial
extremely accreting quasars (xA)	Hard X-ray slope, velocity dispersion	$\mathcal{D}_\bullet = \frac{1}{\sqrt{4\pi}} \left[\frac{l_0 (1 + a \ln \dot{m}_{15}) f_{\rm BLR} R_0}{G \kappa_{\rm n}} \right]^{1/2(1-\alpha)} \frac{V_{\rm FWHM}^{1/(1-\alpha)}}{F_{5100}^{1/2}}$	Wang et al.2013	V
extremely accreting quasars (xA)	virial velocity dispersion: FWHM(Hβ) Eddington ratio = const	$L \propto FWHM(H\beta)^4$	Marziani & Sulentic 2014	V
general quasar populations	X-ray variability, velocity dispersion	$\log \frac{L}{\rm erg\,s^{-1}} + 4 \log \frac{\rm FWHM}{10^3\,km\,s^{-1}} = \alpha \log \sigma_{\rm rms}^2 + \beta,$	La Franca et al. 2014	V
mainly quasars at z<1	Reverberation mapping time delay τ	$\tau/\sqrt{F} \propto d_L$	Watson et al 2011, 2013; Czerny et al. 2013; Melia 2015	
general quasar populations	non linear relation between soft X and UV	$\log(F_X) = \Phi(F_{UV}, D_L)$ $= \beta' + \gamma \log(F_{UV}) + 2(\gamma - 1)\log(D_L),$	Risalti & Lusso 2016	

Figure 18: Overview of the methods proposed in recent years for the use of quasars as standard candles. P. Marziani, personal communication. See text for a detailed explanation.

with $\alpha \approx 0.5$, $\beta \approx 2$. Several studies have found a significant anti-correlation between MBH and X-ray variability $\log M_{BH} = k \log \sigma_{rms}^2 + w$. Combining the two equations, we obtain: $\log L = -2k \log \sigma_{rms}^2 - 4 \log \delta v + const$. In other words, the intrinsic AGN luminosity can be retrieved as a function of δ_v and of the X-ray variability given by σ_{rms}, the normalized excess variance estimator.

3.2.4 Standard rulers: the method of Watson et al. (2011)

Optical variability has been established as an identifying property of type-1 AGNs for more than three decades. AGN typically show continuum variations by 1-2 magnitudes with timescales ranging from days to years. Broad emission lines have also been found to vary (Ulrich et al. 1997). A key idea is to consider that emission line variations lag the continuum variations with delays ranging from a few days to months in luminous Seyfert 1 nuclei. The cross-correlation function between the continuum and the emission line light curve then measures a time lag $\Delta t_{\rm obs}$ due to the travel time needed by continuum photons to reach broad line emitting region (BLR). This means that the distance of the BLR from a supposedly point-like, central continuum source can be simply written as:

$$r_{\rm BLR} = \frac{c\Delta t_{\rm obs}}{1+z},$$

where the factor $(1+z)$ reduces the observed time lapse to the time lag in the rest frame of the quasar.

A linear size that can be used as a standard ruler is the distance between the broad line emitting gas and the central continuum source (hereafter the broad line region radius, $r_{\rm BLR}$). This distance has been measured via reverberation mapping for ≈ 60 active nuclei and quasars at $z \lesssim 1$ (Bentz et al. 2013) with programmes underway to measure $r_{\rm BLR}$ in more distant quasars (e.g., Kaspi et al. 2007; Trevese et al. 2007; Chelouche et al. 2012; Woo et al. 2013). Line luminosity arises from photoionization by an FUV continuum and lines respond to continuum luminosity changes with a time delay, $r_{\rm BLR} \approx c\tau$. The radius $r_{\rm BLR}$ is obtained by measuring the peak or centroid displacement of the cross-correlation function between the light curves of the continuum and a strong line. $r_{\rm BLR}$ is measured in a way that is redshift independent. If it were possible to measure the angular size of the BLR then a redshift independent value of the angular distance $d_{\rm A}$ would follow: $d_{\rm A}(H_0, \Omega_{\rm M}, \Omega_\Lambda) = c\tau/\theta''$ (Elvis & Karovska 2002). However, our ability to resolve the broad line region is still beyond reach of the most advanced optical interferometers (ESO VLTI, etc.): the angular size subtended by the broad line region in some of the nearest sources is no more than a few tenths of milliarcsecond. A second method employing the BLR size as a standard ruler is based on the expected dependence of $r_{\rm BLR}$ with luminosity, originally predicted on the basis of photoionization physics (Davidson 1972; Krolik & McKee 1978) and observationally confirmed from from reverberation data: $r_{\rm BLR} = c\tau \propto \sqrt{L}$ (Bentz et al. 2013, and references thererin; see also Kaspi et al. 2005). The ratio $\tau/\sqrt{\lambda f_\lambda}$ is proportional to $d_{\rm L}(H_0, \Omega_{\rm M}, \Omega_\Lambda)$ (Watson et al. 2011; Czerny et al. 2012). A challenge is to measure τ for a large number of objects.

3.2.5 Extreme Eddington radiators: Wang et al. (2013)

If the Eddington ratio is known ($L/L_{\rm Edd} \propto L/M_{\rm BH}$), then the bolometric luminosity can be derived if the mass $M_{\rm BH}$ is also known. Estimates of black hole mass have now been made for tens of thousands of quasars (Marziani & Sulentic 2012; Shen 2013) following the assumption that some emission lines are broadened by virial motion. Under the virial

assumption it is possible to compute $M_{\rm BH} = f_{\rm S} r_{\rm BLR} {\rm FWHM}^2/G$ (where $f_{\rm S}$ is a structure factor ≈ 1) and hence derive the bolometric luminosity L. In principle this approach can be applied to quasars of any Eddington ratio (Davis & Laor 2011) but, in practice, attempts have been focused on a minority of quasars that are believed to radiate close to an extreme luminosity associated with the Eddington limit.

The condition $L/L_{\rm Edd} \rightarrow 1$ (up to a few times the Eddington luminosity) is physically motivated. When the mass accretion rate becomes super-Eddington, emitted radiation is advected toward the black hole, so that the source luminosity increases only with the logarithm of accretion rate (Abramowicz et al. 1988; Mineshige et al. 2000). The accretion flow remains optically thick so that radiation pressure "fattens" it. The resulting "slim" accretion disk is expected to emit a steep soft and hard X-ray spectrum, with hard X-ray photon index (computed between 2 and 20 KeV) converging toward $\Gamma_{\rm hard} \approx 2.5$ and bolometric luminosity saturating to

$$L \approx \lambda_{\rm L} \left[1 + const. \ln \left(\frac{\dot{m}}{50} \right) \right] M_{\rm BH}, \tag{3.7}$$

where $\dot{m}$ is the dimensionless accretion rate (Mineshige et al. 2000), and $\lambda_{\rm L}$ is a constant related to the asymptotic $L/M_{\rm BH}$ ratio for $\dot{m} \rightarrow \infty$. This result, along with the expression for virial black hole mass, allowed Wang et al. (2013) to write a redshift independent formula for the quasar bolometric luminosity. Magnitude differences between the z independent estimates and the standard estimates based on redshift converge to 0 with a scatter that is $\approx$ 1. magnitude at 1 σ confidence level, if $2.3 \lesssim \Gamma_{\rm hard} \lesssim 2.5$. This method is based on the theoretical prediction of the existence of super-Eddington accretors whose hard X-ray spectrum shows a steep slope.

A challenge in this case is to find a sample that is large enough because only 12 suitable objects at $0 \lesssim z \lesssim 0.5$ have been found by Wang et al. (2013). In addition, we did not favor hard X-ray measures as key 4DE1 parameters (Sulentic et al. 2000a) because they showed weaker correlation with optical/UV line parameters than $\Gamma_{\rm soft}$. Current X-ray databases do not allow us to exploit the soft X-ray excess as a selector of Eddington candles. Instead we look to other UV parameters that are more closely correlated with 4DE1 parameters dependent on Eddington ratio.

3.2.6 Finding extreme Eddington radiators

Extreme sources (hereafter extreme Pop. A sources in 4DE1: or xA) do not show only a soft X-ray excess or a steep X-ray continuum but also the largest $R_{\rm Fe}$ values. This measure is already available for hundreds of low z quasars. A potential 4DE1 correlate involves the prominence of the resonance doublet of AlIIIλ1860 (Sulentic et al. 2007; Negrete et al. 2012). The appearance of the optical and UV spectrum of these sources is shown by Marziani et al. (2014). Avoiding any line width definition, the following two criteria are suitable for selecting high-$L/L_{\rm Edd}$ candidates over a wide z range: 1) $R_{\rm Fe} \gtrsim 1.0$; 2) I(AlIIIλ1860) $\gtrsim 0.5$ I(SiIII]λ1892) (Marziani & Sulentic 2014). These conditions are sufficient to isolate sources radiating close, or better said, *closest* to the Eddingon limit. They are satisfied by $\approx 10\%$ of a low-z sample based on the SDSS (Zamfir et al. 2010). The width of AlIIIλ1860, SiIII]λ1892, and Hβ are extremely well correlated (Negrete et al. 2013).

Sources belonging to spectral types A3 and A4 (i.e., satisfying the criterion $\rm R_{FeII} > 1$ are found to be the sources radiating at the highest Eddington ratio. They show a relatively small dispersion along a well-defined, extreme value $\mathcal{O}(1)$[1] (Marziani & Sulentic 2014). The xA selection criterion is consistent with the parameter $\propto$FWHM/σ+$\rm R_{FeII}$used to identify super-massive extremely accreting BHs (SEAMBHs Wang et al. 2013; Du et al. 2016). Since xA sources show Lorentzian profiles, the criterion based on $\rm R_{FeII}$ should be sufficient unless relatively broad profiles with FWHM$\gtrsim$4000 km/s are considered, a case still under scrutiny.

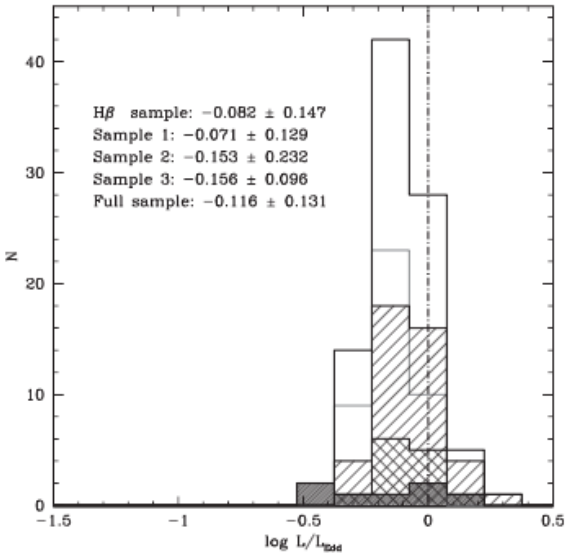

Figure 19: The distribution of Eddington ratio values for several samples selected following the diagnostic criteria of Marziani & Sulentic (2014).

[1]The exact values depend on the normalization assumed for MBH estimates and for the bolometric correction.

The a-posteriori distribution of Eddington ratio values for a sample selected according to the diagnostic criteria indeed shows a well-defined peak at $\rightarrow 1$ with small dispersion, ≈ 0.15 dex (Fig. 19). There is no claim that the distribution of Fig. 19 is peaked around a *true* (unbiased) Eddington ratio value, but this results does not depend on cosmology: changing values for the Ωs affects little the distribution dispersion.

3.2.7 The non-linear relation between $L_{\rm X}$ and $L_{\rm UV}$: the method of Risaliti & Lusso (2015)

The non-linear relation between quasar luminosities in different band can be explored to retrieve the intrinsic lumonisouity of a quasar. The method of Risaliti & Lusso (2015) is based on the non-linear relation between $L_{\rm X}$ and $L_{\rm UV}$: $\log(L_{\rm X}) = \beta + \gamma \log(L_{\rm UV})$, which can be rewritten as $\log(f_X) = \Phi(F_{\rm UV}, D_L) = \beta' + \gamma \log(F_{\rm UV}) + 2(\gamma - 1)\log(D_L)$, where β' depends on the slope and intercept (i.e. $\beta' = \beta + (\gamma - 1)\log(4\pi)$), $f_{\rm X}$ and f_{UV} are measured at rest-frame wavelengths, and D_L is the luminosity distance. The method provides relatively poor estimates for individual quasars, but can in principle be applied to very large samples. It is also unclear whether extinction due to dust may affect the results in a compromising way.

3.2.8 The method of Marziani & Sulentic (2014)

We describe the derivation of the virial luminosity equation closely following the original paper of Marziani & Sulentic (2014). The bolometric luminosity – black hole mass ratio of a source radiating at Eddington ratio $\lambda_{\rm Edd}$ can be written as: $\frac{L}{M} \approx 10^{4.53} \lambda_{\rm Edd} \left(\frac{L}{M_{\rm BH}}\right)_{\odot} \approx 10^{4.81} \lambda_{\rm Edd}$ erg s^{-1} g^{-1}, where $M_{\rm BH}$ is the black hole mass, and L the bolometric luminosity. Under the assumption of virial motion the bolometric luminosity is (setting $\xi \approx 10^{4.81}$ erg s^{-1} g^{-1}):

$$L \approx \xi \lambda_{\rm Edd} M \approx \xi \lambda_{\rm Edd} f_{\rm S} \frac{r_{\rm BLR} (\delta v)^2}{G}. \tag{3.8}$$

where $f_{\rm S}$ is the structure factor (Collin et al. 2006), δv a virial velocity dispersion estimator, G is the gravitational constant, and $r_{\rm BLR}$ the BLR radius. Under the assumption of spherical symmetry, the ionization parameter can be written as:

$$U = \frac{\int_{\nu_0}^{+\infty} \frac{L_\nu}{h\nu} d\nu}{4\pi n_{\rm H} c r_{\rm BLR}^2} \tag{3.9}$$

where L_ν is the specific luminosity per unit frequency, h is the Planck constant, ν_0 the Rydberg frequency, c the speed of light, and $\rm n_H$ the hydrogen number density. The parameter $r_{\rm BLR}$ is the radius of the BLR. There is a way to derive $r_{\rm BLR}$ if one has a good estimate of the product of $\rm n_H \times U$ (Negrete et al. 2013). Without loss of generality,

$$r_{\rm BLR} = \left[\frac{\int_{\nu_0}^{+\infty} \frac{L_\nu}{h\nu} d\nu}{4\pi U n_{\rm H} c} \right]^{1/2} = \left(\frac{\kappa L}{4\pi U n_{\rm H} c h \bar{\nu}_{\rm i}} \right)^{1/2} \tag{3.10}$$

where the ionizing luminosity is assumed to be $L_{\rm ion} = \kappa L$, with $\kappa \approx 0.5$. The number of ionizing photons is $\kappa L / h\bar{\nu}_{\rm i}$, where $\bar{\nu}_{\rm i}$ is the average frequency of the ionizing photons. Several workers in the past used Eq. 3.10 to estimate $r_{\rm BLR}$ (Padovani et al. 1990; Wandel et al. 1999; Negrete 2011; Negrete et al. 2013, 2014). Analysis of a subsample of reverberation mapped sources indicates that Eq. 3.10 provides estimates of $r_{\rm BLR}$ not significantly different from reverberation values (Negrete et al. 2013).

Inserting Eq. 3.10 into Eq. 3.8:

$$L \approx 7.8\ 10^{44} \frac{\lambda_{\rm Edd,1}^2 \kappa_{0.5} f_{\rm S,2}^2}{h\bar{\nu}_{\rm i,100\,eV}} \frac{1}{(n_{\rm H} U)_{10^{9.6}}} (\delta v)_{1000}^4 \ \ {\rm erg\ s^{-1}} \tag{3.11}$$

where the energy value has been normalized to 100 eV ($\bar{\nu}_{\rm i} \approx 2.42\,10^{16}$ Hz), the product $(n_{\rm H} U)$ to the "typical" value $10^{9.6}$ cm^{-3} (Padovani & Rafanelli 1988; Matsuoka et al. 2008; Negrete et al. 2012) and δv to 1000 km s^{-1}.

Eq. 3.11 (hereafter the "virial" luminosity equation) is formally valid for any $L/L_{\rm Edd}$; the key issue in the practical use of Eq. 3.11 is to have a sample of sources tightly clustering around an average $L/L_{\rm Edd}$ (whose value does not need to be 1, or to be *accurately* known). At present, we can identify sources with $\lambda_{\rm Edd} \rightarrow 1$, but it is still possible that an eventual analysis may employ different spectral types representative of much different $L/L_{\rm Edd}$ average values. In practice, an approach followed in this paper has been to consider Eq. 3.11 in the form $L \approx \mathcal{L}_0 \delta v^4$, where $\mathcal{L}_0$ has been set by the best guess of the quasar parameters with $\lambda_{\rm Edd} \rightarrow 1$. This will imply a value of h^{-1}, and to ignore source-by-source diversity.

Are xA sources the super-Eddington accretors postulated by Wang et al. (2013)? xA sources are relatively frequent at low-z, $\approx 10\%$ of optically selected samples. The estimates

of $L/L_{\rm Edd}$ are all below $L/L_{\rm Edd} \approx 2$, the value predicted for super-Eddington accretors. Both the super-Eddington accretors of Wang et al. (2013) and xA sources are sought looking at one extreme property. The extreme properties are correlated in the 4DE1 context, so that it is likely that super-Eddington accretors are included in the xA sample, but they may be a fraction of all xA sources.

3.2.9 The Hubble diagram from the virial equation

Following the notation of Marziani & Sulentic (2014),

$$\mu \approx 5 \cdot \left(\log \frac{c}{H_0} + \log \mathcal{F}(\Omega_{\rm M}, \Omega_k, \Omega_\Lambda, z) \right) - 5 \cdot \log f_{\rm 10pc} + 5 \cdot \log(1+z) \tag{3.12}$$

If we equate the equations above

$$\begin{aligned} 2.5[\log L(\delta v) - BC] - 2.5 \log(f_\lambda \lambda) - 5 \log f_{\rm 10pc} - 2.5 \log 4\pi + 5 \cdot \log(1+z) = \\ 5 \cdot \left(\log \frac{c}{H_0} + \log \mathcal{F}(\Omega_{\rm M}, \Omega_k, \Omega_\Lambda, z) \right) - 5 \cdot \log f_{\rm 10pc} + 5 \cdot \log(1+z) \end{aligned} \tag{3.13}$$

Simplifying:

$$2.5[\log L(\delta v) - BC] - 2.5 \log(f_\lambda \lambda) - 2.5 \log 4\pi = 5 \cdot \left(\log \frac{c}{H_0} + \log \mathcal{F}(\Omega_{\rm M}, \Omega_k, \Omega_\Lambda, z) \right) \tag{3.14}$$

$$\log \frac{[L(\delta v) - BC]}{4\pi (f_\lambda \lambda)} = 2 \cdot \left(\log \frac{c}{H_0} \mathcal{F}(\Omega_{\rm M}, \Omega_k, \Omega_\Lambda, z) \right) \tag{3.15}$$

$$[L(\delta v) - BC] = 4\pi \left(\frac{c}{H_0} \mathcal{F}(\Omega_{\rm M}, \Omega_k, \Omega_\Lambda, z) \right)^2 (f_\lambda \lambda) \tag{3.16}$$

In principle our distance modulus computed from the virial equation is:

$$\mu = 2.5[\log L(\delta v) - BC] - 2.5 \log(f_\lambda \lambda) - 100.19 + 5 \cdot \log(1+z) \tag{3.17}$$

where the constant -100.19 is $-2.5 \log(4\pi f_{\rm 10pc})$, where $f_{\rm 10pc} \approx 3.08 \cdot 10^{19}$ i.e., the distance of 10pc expressed in cm.

Note that $(f_\lambda \lambda)$ refers to the rest frame fluxes (the term $(1+z)^2$ appears in both terms

of the equations, for the virial luminosity and for the distance modulus where the luminosity distance was used). We recover the expression used by Marziani & Sulentic (2014).

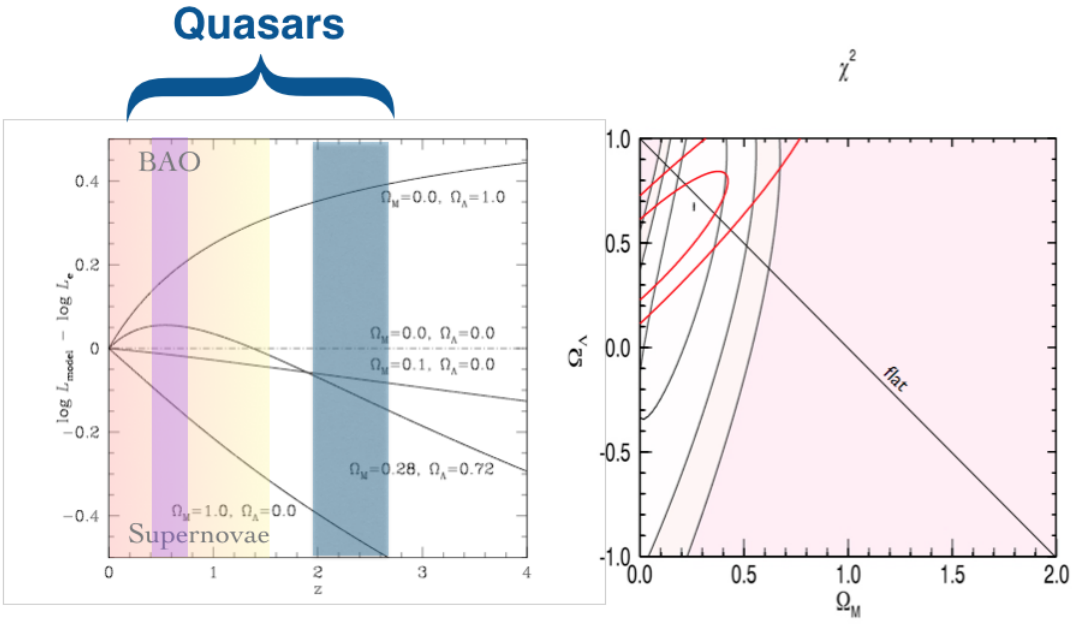

Figure 20: Left: $\Delta \log L$ for various cosmological models as a function of z with respect to an empty Universe. Quasars in the pale blue redshift range are in a range where the effect Ω_M dominates over the acceleration. Right: comparison between the constraints set by the supernova photometric survey (Campbell et al. 2013) (red contour lines) and a mock sample of 1000 quasars with rms = 0.3 (shaded contours). Confidence intervals are at 1, 2 σ for supernovæ and 1, 2, 3 σ for the quasar mock sample. Quasars have the potential to impose tighter constrain on Ω_M by virtue of their coverage of $z \gtrsim 1$. Only statistical errors are included in both cases. Right panel from Marziani & Sulentic (2013).

3.2.10 Prospects for quasar methods

There is an advantage due to the ability of quasar data to cover almost uniformly the range between 0 and 4. Supernovæ have been discovered mainly at $z \lesssim 1$, and Planck and WMAP deal after all with features detected at the surface of last scattering when the Universe became transparent to radiation, at $z \sim 1000$. Quasars can sample cosmic epochs when the negative pressure of dark energy was dominating, as well as earlier epochs when the Universe expansion was still dominated by the effect of matter ($z \gtrsim 1$, as shown in the left panel of Fig. 20). If 400 xA sources with rms ≈0.3 dex can be found then constraints on Ω_M will be meaningful. Fig. 20 shows the expectations for a 400-strong quasar mock sample simulated with uniform rms = 0.3 over the redshift range 0.2 – 3.0. Quasars will yield similar constraints on Ω_M as supernovæ since they are able to chart cosmic epochs when

matter dominated cosmic expansion. In both cases, only statistical errors were considered.

The comparison between the constraints set by the supernova photometric survey described by Campbell et al. (2013) (red lines) and an hypothetical mock sample of 400 quasars with rms = 0.3 that assumes concordance cosmology (shaded contours) in also shown in the right panel of Fig. 20. Confidence intervals are at 1 and 2 σ for supernovæ and 1, 2, 3 σ for the quasar mock sample. The flat geometry loci $\Omega_{\rm M} + \Omega_\Lambda = 1$ are also shown. Note the potential ability of the quasar sample to better constrain $\Omega_{\rm M}$. Only statistical errors are included in both cases.

In Fig. 21 we show the Hubble diagram obtained from the use of the virial equation applied to several quasar samples. Even if the dispersion is very high $\sigma_\mu \approx 1$ mag, the diagram provides a proof of the conceptual validity of the virial L estimates. In Fig. 21 the filled lines represents a lsq fit to the residuals as a function of z. Its slope ($b \approx -0.035 \pm 0.130$) is not significantly different from 0, indicating good statistical agreement between luminosities derived from concordance cosmological parameters and from the virial equation. Red circles indicate outliers whose profile appears composite at a second inspection, suggesting the presence of a line broadening component not associated with virial motions. The result shown *assumes* a constant value of the ratio $\lambda f_\lambda(5100)/\lambda f_\lambda(1800)$ from an average SED.

We are still far from the precision of absolute magnitudes of type Ia supernovæ whose dispersion is now estimated ≈ 0.15 mag (Folatelli et al. 2010; Hook 2013). The dispersion in Eddington candles is also much larger than the dispersion in the $r_{\rm BLR} - L$ relation, ≈ 0.13 dex that has been proposed by Watson et al. (2011) as a valuable cosmological ruler. Even if the dispersion in bolometric luminosity of the Eddington standard candles is disarmingly large (but it is likely that the rms can be significantly reduced as it happened for supernovæ; Jacoby et al. 1992, and references therein), they might be useful if one exploits the possibility of building large samples uniformly covering a wide redshift range.

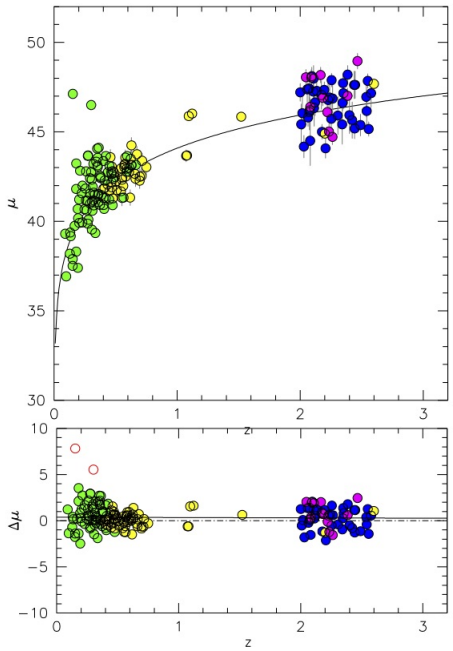

Figure 21: Hubble diagram obtained from the analysis of the MS14 data (yellow: Hβ, navy blue: AlIIIλ1860 and SiIII]λ1892) supplemented by new Hβ measurements from the SDSS (green) and from GTC observations (magenta). The lower panel shows the distance modulus residuals with respect to concordance cosmology.

Chapter 4

Line profiles and broad line region (BLR)

4.1 Line profile shapes

All spectral lines have a finite width and a particular profile. It is generally defined as a function of energy added to the observed background or the continuum (Pradhan & Nahar 2015). Line broadening mechanisms vary widely depending on the physical context. At most basic level, the natural line width is related to Heisenberg's uncertainty principle. This is related to the finite lifetimes of energy levels. The characteristic line profile for radiation damping is a Lorentzian function. A second factor is the temperature of the emitting gas that leads to Doppler broadening due to the thermal motion of ions. It can be shown that for a Maxwellian distribution of particles at a given temperature the line shape due to Doppler broadening is a Gaussian function. In the context of the BLR, the line broadening associated with the thermal motion of the emitting ionic species is too low to account for the observed line widths. A third factor is the particle density, involving collisions among electrons, and ionic species. The line profile due to collisional broadening is Lorentzian. The classical collisional broadening however refer to densities that are higher than the ones encountered even in the densest parts of the BLR.

Finally, in cases where several types of broadening mechanisms manifest themselves, given by Gaussian and Lorentzian functions, the total line profile is obtained by a convolution over both functions resulting in a Voigt profile.

In the context of the BLR, the main broadening mechanism is associated with Doppler effect due to the motion of the line emitting gas. Scattering mechanisms such as electron scattering have been considered (Laor 2006) especially for the extended line wings sometimes observed in Lyα, but they are usually not considered the main broadening mechanism. A special case is gravitational redshift. It is naturally expected to be present if the line emitting regions extend down toward ~ 100 gravitational radii. This concerns mainly Pop. B sources where redward asymmetries consistent with gravitational redshift are observed (Corbin 1995; Bon et al. 2015).

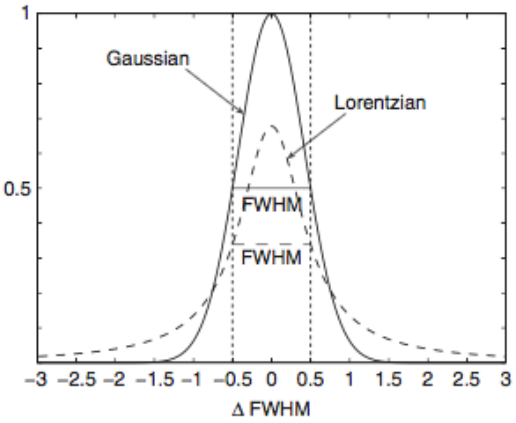

Figure 22: Comparison between Lorentzian, and Gaussian profiles.

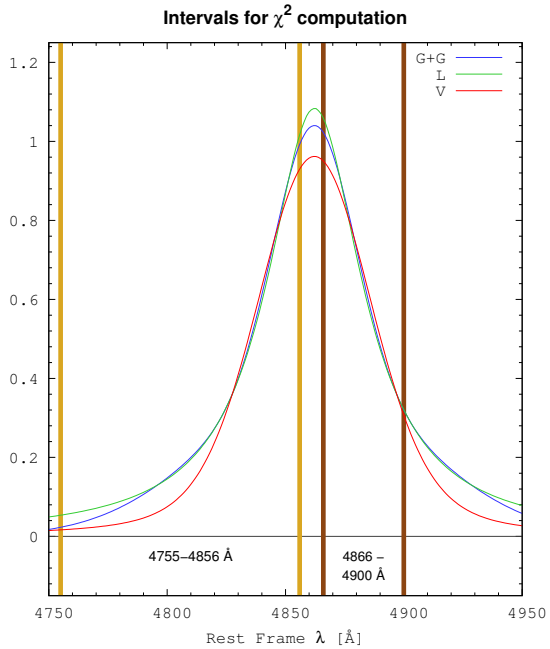

Figure 23: Comparison between Lorentzian, double Gaussian, and Voigt Profile.

4.2 Gaussian, Lorentzian, and Voigt emission profiles

The Gaussian profile can be written

$$G(\lambda) = \frac{1}{\sqrt{2\pi}\sigma} e^{-\frac{(\lambda-\lambda_0)^2}{2\sigma^2}} \tag{4.1}$$

where σ is the velocity dispersion, and λ_0 is the peak wavelength of the line profile. The FWHM is $2\sqrt{2\ln 2}$.

The Lorentzian profile can be written

$$L(\lambda) = \frac{1}{\pi\gamma} \frac{\gamma^2}{\left(\frac{(\lambda-\lambda_0)^2}{\gamma^2}\right) + 1} \tag{4.2}$$

where the FWHM $= 2\gamma$. Fig. 22 compares Gaussian and Lorentzian shapes. The σ parameter (i.e., the dispersion of the distribution) is not defined.

The Voigt profile is the convolution of a Lorentzian with a Gaussian and is defined by:

$$V(\lambda) = \int_{-\infty}^{+\infty} G(\lambda')L(\lambda' - \lambda)d\lambda' \tag{4.3}$$

There is no primitive associated with the Voigt function, so that its values have to be computed numerically or by a rational approximate expression. Fig. 23 compares Lorentzian, double Gaussian, and Voigt profiles.

In the context of BLR, the parameter FWHM/σ is of special importance. Fig. 24 shows the behavior of the the parameter FWHM/σ as a function of FWHM, for Hβ. Pop. A and Pop. B sources show as systematic difference in the parameter FWHM/σ. FWHM/σ for Pop. B is more consistent with a Gaussian profile (FWHM/$\sigma \approx$2.35). On the converse FWHM/σ is significantly lower, as expected for a more Lorentzian-like profile.

4.3 Profiles and BLR structure

Fig. 25 shows a sketch of disk/outflow models that are consistent with the constraints provided by the observations of LILs and HILs. The sketches of Fig. 26 distinguish quasars accreting at low and high rate respectively (c.f. Marinucci et al. 2012; Marziani et al. 2014). The main theoretical prediction is that we expect an inner accretion disk region assimilable to a slim disk (Abramowicz et al. 1988; Szuszkiewicz et al. 1996; Frank et al. 2002). In the

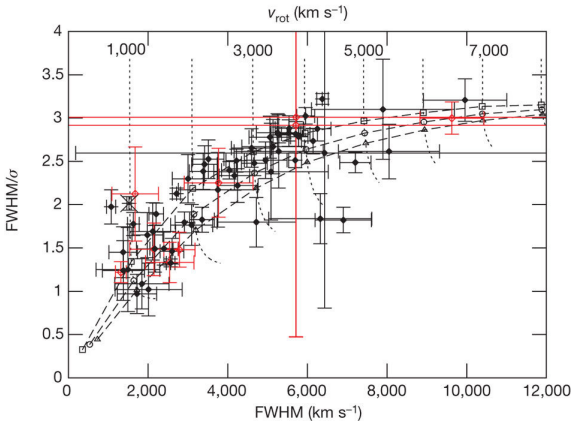

Figure 24: The behavior of the the parameter FWHM/σ as a function of FWHM, for Hβ, as shown by Kollatschny & Zetzl (2011).

case of disk dominated sources, the outflow/wind component usually give rises to blueward asymmetries and it is not dominating the broad profiles even of HILs. In the case of wind dominated sources, traces of outflows are detected even in low-ionizaton emission lines (for example in MgIIλ2800, Marziani et al. 2013b,a). In CIVλ1549 the blue shifted emission associated with the outflows can be dominating the flux of the line.

In Pop. A sources it is tempting to speculate that LILs may be favored with respect to HILs by the shielding of the hottest continuum due to the slim disk geometry. However, the question remains whether the ionized outflow we see in CIVλ1549 is associated with the central cone defined by the walls of the slim disk (which may be much steeper than the ones deducted in the cartoon, Sądowski et al. 2014). In Pop. A, the CIV shifts are largest but the CIV EW is lowest (Pop. A includes weak lined quasars, Diamond-Stanic et al. 2009; Shemmer et al. 2010), which may imply that the gas is over-ionized or, alternatively, that the FUV continuum is absorbed/weakened, as in the case of emission from the shielded part of the disk between the slim structure and the torus.

In the case of a flat-disk (Pop. B right-panel), the problem of disk wind over-ionization may be solved by the failed wind scenario (Murray et al. 1995; Marinucci et al. 2012): inner gas may offers an effective screen and only shielded gas is efficiently accelerated. Models of disk-wind systems are successful in reproducing the profiles of Balmer lines (Flohic et al. 2012). To explain the redward asymmetries often observed in Pop. B, either Balmer lines are emitted in an infalling scenario (which require large column density to withstand radiation forces) or the accretion disk itself could be emitter. In the latter case the redward asymmetry could be ascribed in full to transverse and gravitational redshift (Bon et al. 2009, 2015).

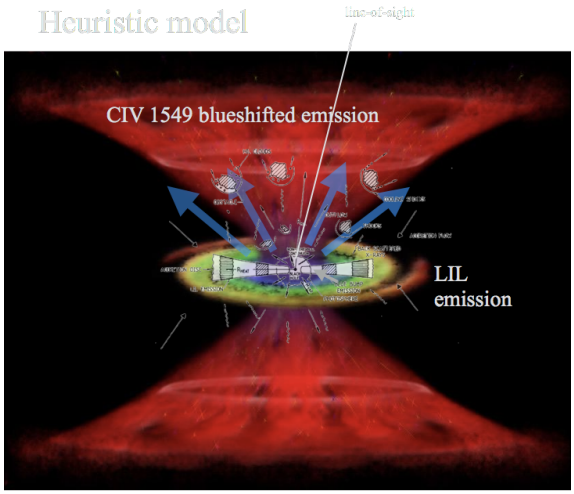

Figure 25: Disk/outflow models that are consistent with the observations. Two sketches are superimposed: the black-and-white refers to the model of Collin-Souffrin et al. (1988), in which HILs are emitted by clouds in radial motion above and below the accretion disk, over the color image of disk+ wind model of Elvis (2000).

Roles of magnetic fields and of black hole spin are not considered although presumably important, black hole spin because of its effect on the inner accretion disk temperature, and magnetic fields because they may provide an acceleration mechanism for disk wind (Emmering et al. 1992).

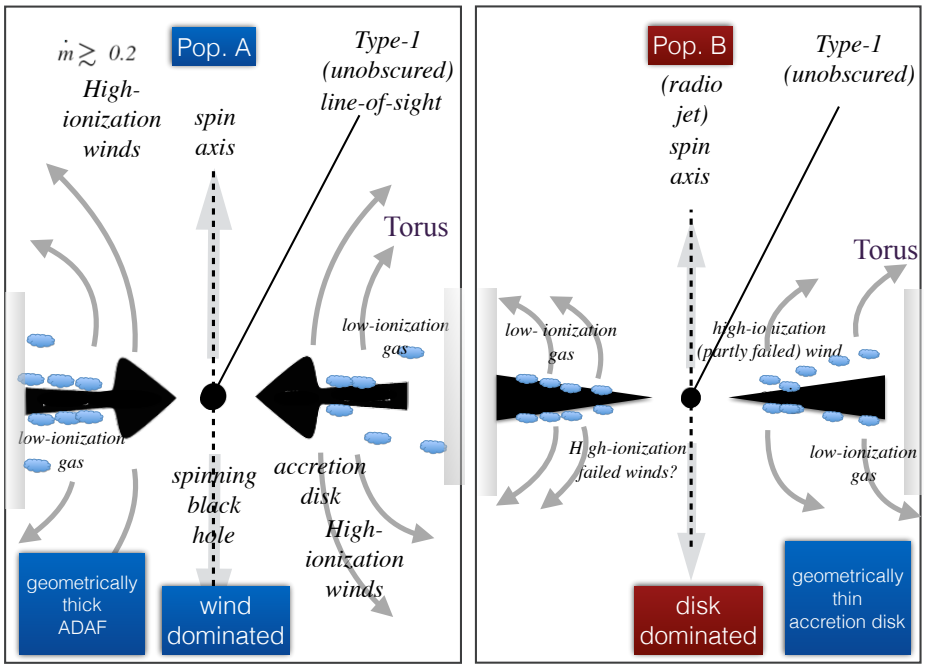

Figure 26: Different structure for Pop. A and B (right), with a slim and a flat disk respectively. The sketch is not drawn to scale and the relation between line emitting regions (shown here as clouds) and accretion disk structure is still debated. Some of the differences in the left and right side of each panel might highlight different possibilities. See §4.3 for a more detailed explanation.

4.4 Widely discussed models

The basic model involving accretion on a super-massive black hole is now almost universally accepted. In Tab. 4.1 we report some structures that have been discussed in the past, and are still being discussed. The Table has been adapted from Sulentic et al. (2000a). In the last few years there have been intriguing detections of periodic signals and periodic line profile changes that have been interpreted as due to a binary black hole (Bon et al. 2017, and references therein). The classical cloud model has been disfavored in view of the problems with cloud numbers and stability, but is often consider because of the lack of alternative models. Emission from the accretion disk is considered as a viable possibility for LILs. Emission in a bipolar outflow or wind is of high ionization and has been supported by the ubiquitous detection of large blueshifts in CIVλ1549.

Table 4.1: PROS AND CONS OF CURRENT BLR MODELS

MODEL	PROS	CONS
BINARY BH	Existence of double-peaked sources and objects like NGC 5548 that show two independent RM components in wings of H$\beta_{\rm BC}$	Long-term monitoring of Arp 102B and 3C 390.3 does not show predicted v_r variations Ruled out by spectropolarimetry of several double-peakers.
CLOUDS	Locally Optimized Clouds (LOC) account for BLR stratification. "Bouncing clouds" account for stochastic red/blue shifts/asymmetries. RM results for some Pop B sources support a spherically symmetric system of anisotropically illuminated clouds.	Smooth profiles require an extremely large (10^{7-8}) number of clouds in two Pop A sources Clouds are not stable if in pressure equilibrium with a confining medium Systematic blueshift of HIL profiles in pop. A sources
DISKS	Keplerian motion is compatible with RM results for Pop. A. objects. Relativistic Keplerian AD explain wide separation double peakers (mostly Pop B and RL objects). AD provide a smooth medium which meets the requirements of very high resolution Keck spectra. AD provide high n_e and N_c medium for production of FeII$_{\rm opt}$ and other LIL such as CaII. Single-peaked lines possible if emission extends to large radii and/or if AD is seen almost face-on. –	General diagreement with observed profiles. in line shift–asymmetry parameter space. Double peakers show largest FWHM and are rare. Double-peaked lines appear suddenly in some sources: NGC 1097, Pictor A and M 81. Double peakers almost entirely Pop B and RL sources AGN, which are the ones where FeII$_{\rm opt}$is the weakest. Line polarization is low, $\parallel$ to disk axis, (except in two extreme pop. A) with no dependence on λ. Double-peakers show centrally peaked H$\alpha_{\rm BC}$ in polarized light.
WINDS/ BICONES	Evidence for radial outflow from CIV in Pop. A sources Radiation-driven/hydromagnetic winds are compatible with observation in Pop A sources Shapes and widths of scattered lines + optical polarization vector $\parallel$ radio axis favors *a biconical* BLR + thick torus. Biconical outflow can fit profile shape and variability in some double-peakers if radio axis oriented close to line of sight.	– Inconsistent with some reverberation results Biconical outflow models in RL requires that the receding part of the flow is also seen. Double peakers are double-lobed radio sources.

Chapter 5

Balmer emission analysis along *4DE1*

5.1 Sample

For the studies in the Fe II prominence range $0 < R_{\rm Fe\ II} < 1$, our sample is 680 quasars strong and selected by Marziani et al. (2013b, hereafter M13) in the SDSS Data Release 7 (DR7). The sources are cataloged as type 1 active galactic nuclei in the redshift range 0.4 to 0.75 and with magnitudes brighter than $g \approx 18.5$. Also M13 set the rest frame by measuring the wavelengths of three of the most prominent narrow lines ([OII] λ3727, Hβ and [OIII] λ5007. An average of the three lines in each spectrum was computed by M13 in order to account for residual systematic shifts, in addition to the ones provided by the SDSS. A clipping of individual measurements deviating due to poor data or intrinsic blueshift of the [OIII] took part of this procedure.

The highly accreting (xA) quasars with $R_{\rm Fe\ II} > 1$ are part of a sample employed by Marziani et al. (2017). The sample is 77 strong and it includes SDSS low-luminosity sources at low redshift. These authors develop a preliminary Hubble diagram with this sample together with samples from SDSS DR6 and DR7 by Marziani & Sulentic (2014) and high redshift observations from Gran Telescopio Canarias.

5.2 Composite spectra

The first sample to be analyzed was $0 < R_{\rm Fe\ II} < 1$. As a starting point, we assigned objects to spectral bins by the estimation of FWHM(Hβ) using IRAF *splot*. Prior to this measurement, we did a subtraction of the narrow component from Hβ using a Gaussian model. For the $R_{\rm FeII}$ component of the optical plane we employed the spectral assignment done by M13. In the range $0 < R_{FeII} < 0.5$, the bins were defined in order of FWHM and are labeled A1, B1, B1+, B1++ and B1+++ with ΔFWHM= 4000 km/s for each bin, by Sulentic et al. (2002, S02). Table 5.1 shows the distribution of the objects in each bin of the E1 sequence by S02 and the composite spectra bins used in this study.

We restricted the M13 sample following two criteria:

1) Radio-quiet (non-jetted) quasars. The prevalence of RL quasars is not constant along the E1 sequence. The RL distribution depends on the bin we are considering, increasing towards larger FWHM (Sulentic et al. 2000).

2) For A1 bin, we made a separation between sources with peculiar Fe II emission which is lower than the expected for this bin and they were discarded to build the composite spectra. These sources probably correspond to population B sources observed face-on.

From the FWHM(Hβ) estimation we proceed to construct composite spectra for bins of 1000 km/s because our aim is to test the different functions that can model Hβ emission in a systematic way through the smallest FWHM bins our data allows us to use, that is ~ 10 spectra per bin. If there are not enough spectra for a bin of width 1000 km/s then we expand the bin[1] width to Δ FWHM= 2000 km/s or 4000 km/s as in the case of the bin B1++ with FHWM(Hβ) 14 000 - 16 000 km s^{-1} and the widest bin B1+++. Nevertheless, there are three exceptions that we use less than 10 spectra, those can be seen in table 5.1, even if they have high signal to noise ratio we do not discard the possibility to fit a composite with sources of very width FWHM(Hβ).

[1]The notation employed in this study for the bins of ΔFWHM = 1000 km s^{-1} or higher is: Spectral Type + FWHM(Hβ) *lower limit* - FWHM(Hβ) *upper limit*. for instance, bin B1++ with FHWM(Hβ) 14 000 - 16 000 km s^{-1} is denoted as B1++ 14-16.

Table 5.1: Number of objects assigned to each type and bin to build the composite spectra.

Type	N	Bin	N	RL[a]	CS[b]
		1000-2000	8	1	4
A1[c]	76	2000-3000	26	6	13
		3000-4000	42	6	28
		4000-5000	31	4	27
B1	159	5000-6000	39	12	27
		6000-7000	38	2	36
		7000-8000	51	9	42
		8000-9000	54	12	42
B1+	156	9000-10000	44	7	37
		10000-11000	32	7	25
		11000-12000	26	3	23
		12000-13000	21	3	18
B1++	39	13000-14000	11	3	8
		14000-16000	7	2	5
B1+++	14	16000-20000	14	4	10

[a]Radio-loud quasar, discarded for the composite spectra.
[b]Number to build the composite spectra.
[c]16 spectra with peculiar Fe II emission, discarded for the composite spectra.

For building the composite, we use the IRAF task *scombine* to compute an average and a median spectrum for each bin. There is an option of threshold rejection step as a parameter of *scombine*. Threshold rejection may be used to exclude very bad pixel values or as a way of masking images. The first case is useful to exclude very bright cosmic rays. The sigma clipping algorithm computes at each output pixel the median or average excluding the higher and lower values out of certain confidence level. Values deviating by more than a specified sigma threshold are rejected. One variation of this procedure is the average sigma clipping which assumes a sigma about the median or mean proportional to the square root of the median or mean in each pixel. We did not include any threshold rejection: an average sigma clipping produced a strong distortion in the [OIII] narrow lines on the composite spectra we built for the bins between A1 1-2 and B1+++.

Figure 27 shows the average composite spectra in the sequence Δ FWHM = 1000 km/s together with their RMS noise. We use the IRAF task *sarith* to operate arithmetically the individual spectra in order to compute the average±RMS spectra that allow us to visualize

any large variation the composite could present due to extremes values in individual spectra.

5.3 *Specfit* line fitting

The IRAF task *specfit* allows for continuum, Fe II and narrow line fitting employing a χ^2 minimization technique. We fitted the median composite spectra because it preserves the shape of the lines better than the average (arithmetic mean). Given that the number of objects assigned to the bins are relatively low, it is reasonable to use median composite spectra (Bachev. et al. 2004) because an average of ~ 10 objects will be greatly influenced by strong unexpected features of individual spectra. Prior to use *specfit*, we converted the fits file of the composite spectra to an IRAF image using the task *rfits*. The step size in wavelength pixels was then set to unity with the task *dispcor* using the parameter *dw=1.000*. This is important to the determination of the degrees of freedom (*df*) in the fitting procedure.

For each 1000 km/s bin, we set the continuum and the Fe II emission before the line fitting. The parameters of these components are: intensity, shift and width for Fe II emission and intercept at the origin and exponent of the power law for the continuum. These components must not change while we consider different profiles of Hβ. For instance, in the case of bin A1 1-2 to B1-8-9 we fitted three wavelengths intervals: 4200-4220, 4440-4740, 5080-5500 Å. The first range gives a good reference for the continuum emission because we do not consider any feature in this range close to Hγ line. Figure 28 shows the continuum level and the Fe II emission for the first 7 bins, from 1000-2000 km s^{-1} to 7000-8000 km s^{-1}.

The next step is the fit of the narrow component of Hβ, because its wavelength is set to be fixed given that it is the location of the quasar rest frame. This fit is performed individually for each composite spectra using the task *splot*. Another constraint on the narrow component is FWHM(Hβ_{NC}) $\approx$ FWHM([OIII] λ5007). Additionally, the noise rms is measured. The noise RMS is needed to compute the χ^2_ν of the model. With *splot* we use the command m to perform the RMS noise measurement in a featureless part of the spectrum around 5550 Å.

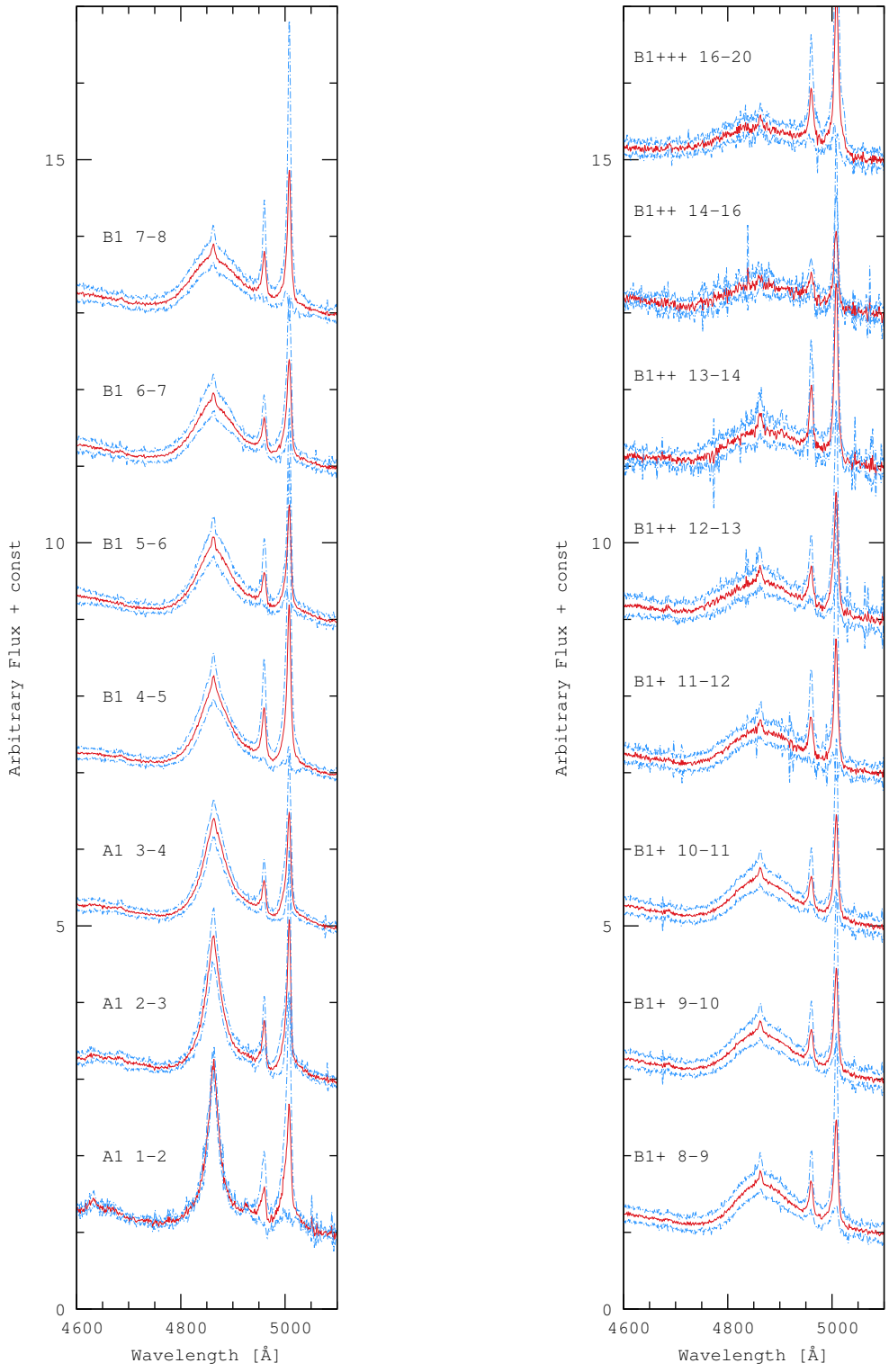

Figure 27: Composite average spectra (red color) as a function of FHHM(Hβ) with $0 < R_{FeII} < 0.5$ displayed on bins of 1000 km s^{-1} and their noise RMS spectra (light blue color) added and subtracted. The notation "A1 1-2" denotes the spectral type in the original sequence and the bin velocity interval of 1000 and 2000 km s^{-1}. The wavelength range is 4600-5100 Å and the spectrum is centered on the Hβ line (broadest profile). The narrow lines are [OIII] $\lambda\lambda$ 4959, 5007 and the Hβ narrow component.

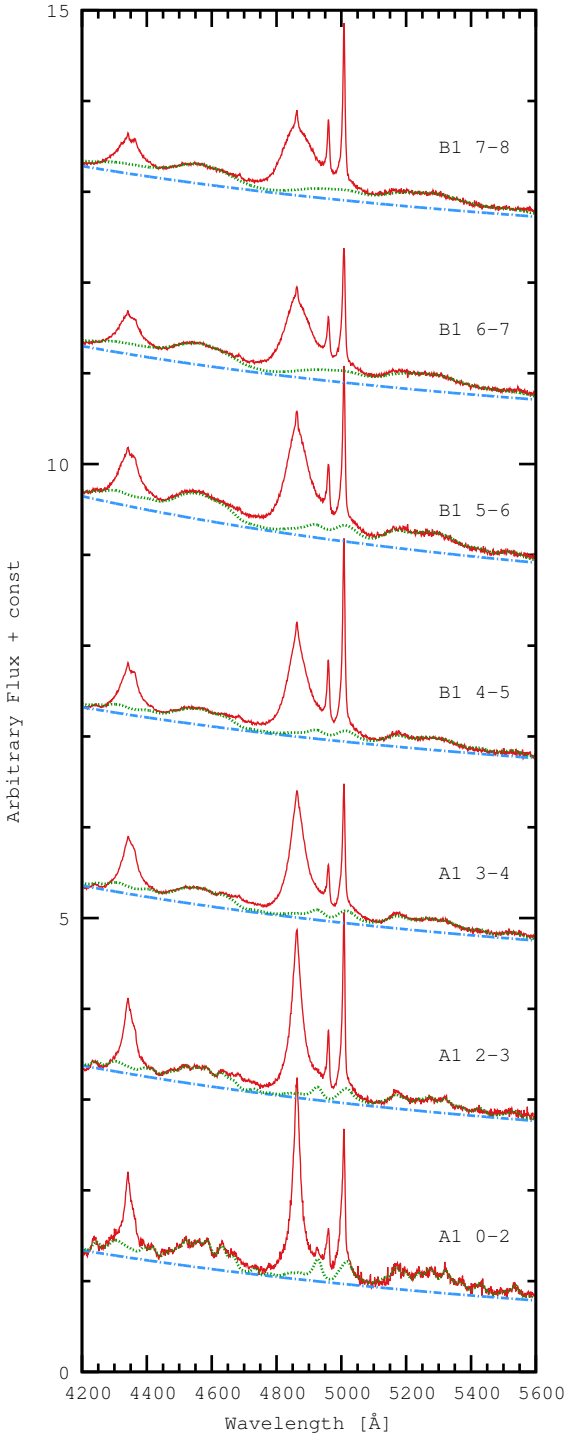

Figure 28: Setting of the continuum emission (blue dot-dashed line) and Fe II emission (green dotted line) over composite median spectra on bins of 1000 km s^{-1}. These assignments are the same for every bin independently of the function that models the Hβ emission and the other considered lines. This guarantees that every fit is done under the same conditions.

The range to be fitted with a multicomponent model is 4500-5600 Å. The main components for the line fitting are:

- Hβ broad component
- Hβ narrow component
- [OIII] $\lambda\lambda$ 4959, 5007
- HeI $\lambda\lambda$4471, 5016
- HeII λ4886
- HeII broad component
- Two blueshifted semi-broad components of [OIII] $\lambda\lambda$ 4959,5007.

Other lines that are not always present (first two) or may not affect considerable the fitting are:

- Hβ redshifted very broad component
- Hβ blueshifted associated emission to [OIII] (Boroson 2005)
- [N I] around 5150-5200 Å
- [Fe VI] around 5150-5200 Å
- [Fe VII] around 5150-5200 Å

Some comments can be made about the listed components on their physical interpretation and the constraints we considered to make the analysis. For example, one of the first evidences of the very-broad line region (VBLR) is the line HeII λ4686 (Peterson & Ferland, 1986). This line presented an increase in intensity accompanying the optical continuum suggesting that a region with highly ionized gas closer to the center than the BLR. The large width of the line could represent an inflow towards the center, i.e, a possible evidence of accretion onto the SMBH.

The case of [OIII] emission with a blueshifted component is very interesting because it reflects two regions with distinct kinematical and physical properties. The narrow component comes from the low-density NLR affected mainly by the stellar content in the bulge and

the blueshifted component has its origin in a more inner region including a wind/outflow influenced by the gravity of the SMBH (Bian et al. 2005). The width of [OIII] line is correlated with Eddington ratio and this is an evidence of the wind presence an inner NLR (Boroson, 2005). Another component, usually found in A1 bin, is HeI $\lambda\lambda$ for which there is a constraint in the width: the FWHM is the same as the HeI λ5876. In this case we measured with *splot* the width of the line HeI λ5876 to assign a fixed width to the HeI emission in the range we considered.

The lines (components) and their parameters are input values for specfit in a data base file. The parameters of each line are usually four. For the Gaussian profile, the flux, the centroid of the line, the FWHM in km s^{-1} and skewness (fixed value of 1). The Lorentzian profile has the same first three parameters and the fourth one is the exponent of the ($x-$centroid) in the denominator of the function (this value is fixed at 2). For the Voigt profile, we created a *userline* component which has four parameters: normalization, linear shift in wavelength, redshift (set fixed to 0) and a "key" parameter related with the width of the function. We usually set 13-25 free parameters for a whole model with 11 to 16 components, given that some of them are dependent on each other or other are fixed as the case of rest-frame wavelengths.

Previous studies found that at FWHM $\leq$ 4000 km s^{-1} the broad component is fitted by a Lorentzian function (Sulentic et al. 2002). We use the Lorentzian (L model) function from the bin 1000-2000 km s^{-1} to 4000-5000 km s^{-1}. On the other hand B profiles require the sum of two Gaussians (G+G model): an unshifted Gaussian core and a redshifted Gaussian base associated with a very broad component. The doubled- Gaussian function models the bins from 3000-4000 km/s to the broadest bin B+++, 16,000-20,0000 km/s. The Voigt function (V model), which is the function we want to test as an alternative to Gaussian and Lorentzian, is used to model all the velocity bins from 1000−2000 km/s to 16,000−20,0000 km/s. Also, we consider the model of a Voigt function and Lorentzian function with an additional redshifted Gaussian (V+G and L+G model, respectively) for the bins in the border between Population A/B. With this our aim is to test how the transition between the two populations is represented in the Hβ profile with the minimum interval ΔFWHM(β).

In order to decide which fit is the more appropriate for the model we compute a χ^2_ν value at a specific intervals relevant to the Hβ profile. These intervals can vary along the sequence depending of the influence of [OIII] features and the narrow component of Hβ.

For example, for bin A1 1-2 are 4760-4860 (left core and wing Hβ profile), 4865-4915 (right part of the core Hβ) and 5040-5120 (right wing Hβ after the line [OIII] λ5007). The number of degrees of freedom ν is the number of pixels in the region within the mentioned intervals minus the number of free parameters in the multicomponent line model (input database for Specfit).

The models are compared performing an F-test. The F-test consists in a comparison between two F values. The first F is the value of the χ^2_ν ratio of two models:

$$F = \frac{\chi^2_\nu \text{ (Model 2)}}{\chi^2_\nu \text{ (Model 1)}} \tag{5.1}$$

where conventionally the larger χ^2_ν goes on the numerator. The second F value is the value of the F-distribution that depends on the confidence level we want to assign and the number of degrees of freedom in each model: $F(\text{confidence level}, df_{\text{Model 1}}, df_{\text{Model 2}})$. We are considering confidence level of 1-σ and 2-σ, specially the last one to discriminate between two models. With this confidence level, if the value of equation 5.1 is greater than the second F from the F-distribution, we can conclude that the model 1 is a better fit than the model 2. Table A.1 displays the values for χ^2_ν and F-test for relevant models employing the first two wavelength intervals for mentioned above.

5.4 A1 and B1 populations

This section includes the results of the statistical analysis of the five models employed as they were described above. Table A.1 and the other tables in the Appendix gives an overview of the results for a χ^2_ν computed over two intervals in the fitted wavelength ranges (4500-5600 Å). The table is followed by the plots of the models confronted with the composite spectra. We include in the plots every component employed to construct the final model.

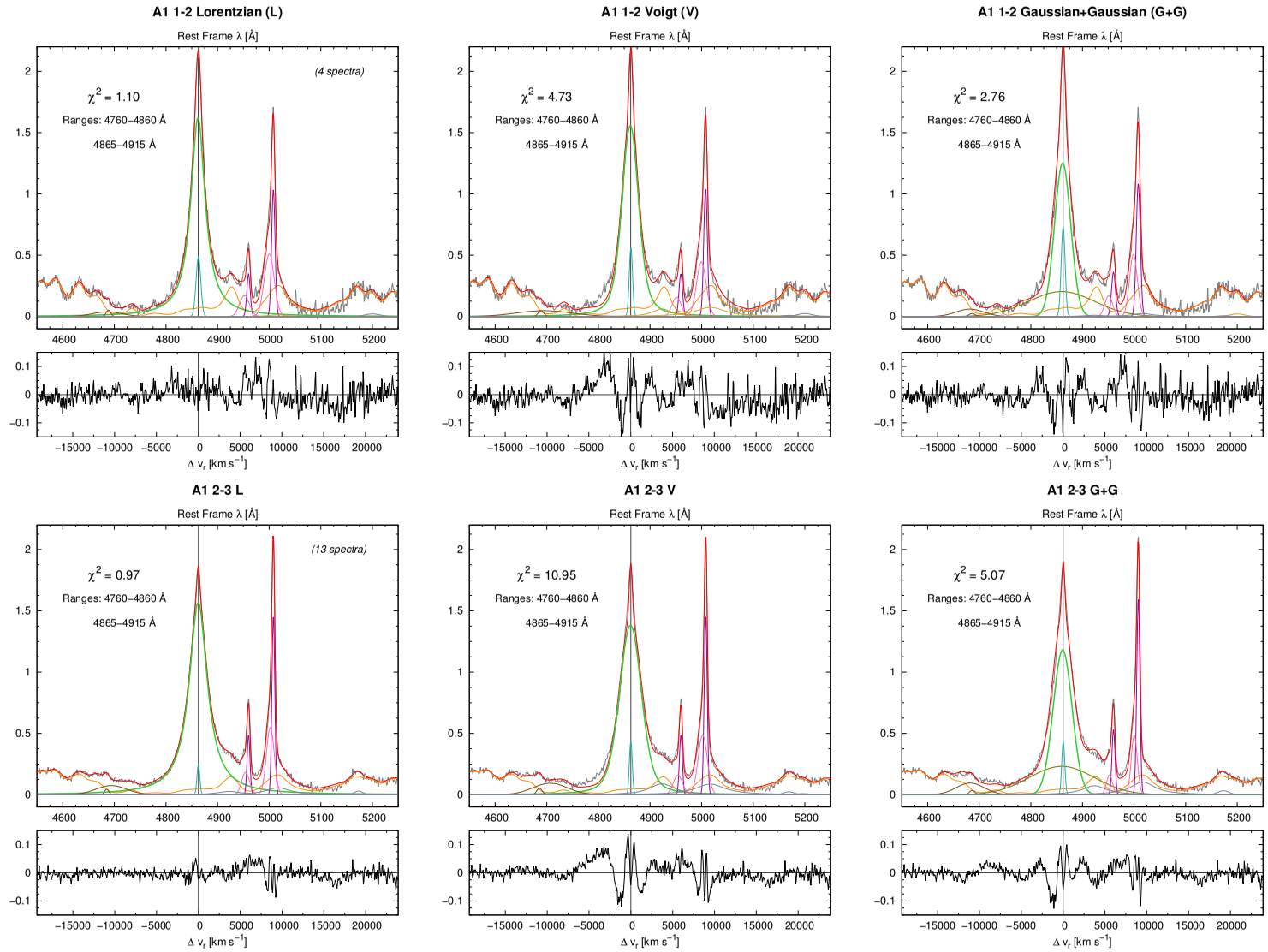

Figure 29: *Upper panel*, continuum subtracted spectra and fitting results for the bin A1 1000-2000 km s^{-1}. The horizontal scale is the rest-frame wavelength (Å) or velocity shift with the origin indicating rest-frame wavelength of the quasar measured on the narrow component (NC) of Hβ. *Lower panel*, fitting results for the bin A1 2000-3000 km s^{-1}. Each plot shows the evaluated χ^2_ν and the wavelength intervals considered in the computation.

From Table A.1 we can highlight several results:

1) We confirm the Lorentzian model is the most appropriate for all the bins in the A1 group with an acceptable accuracy, even in some cases at 3-σ confidence level.

2) For the B1(+,++.+++) there is a degeneracy between the two models that include a BC either as Gaussian or Voigt profile. As general conclusion, we cannot really ensure a preferential model for the wide bins in the range $0 < R_{\mathrm{Fe\ II}} < 0.5$. This statement is true for the majority of the bins because we are not able to differentiate them above 2-σ or even 1-σ confidence level. The suggestion to future work is to build composite spectra with higher signal to noise ratio in order to discriminate between the models V+G and G+G.

3) For B1 bins the Gaussian plus Gaussian (G+G) model seems slightly better than the model Voigt+Gaussian (V+G) with 2-σ confidence level in the best case in for the FWHM(Hβ) bins 4-5 and 5-6, in other words, at the border between Population A and B.

4) From the points 2 and 3, we reassert the discontinuity at FWHM(Hβ) = 4000 km s^{-1}, where the profile shows a relatively drastic change between a single Lorentzian BC to a two component model with a VBC shifted towards the red (~ 4900 Å).

Figure 29 presents the fit and the residuals for the models tested on the bin A1 1000-2000 km s^{-1}. This is the bin with lowest signal to noise ratio (~ 30, with *splot*) because it only includes 8 spectra. On the other hand, the bin B1 7000-8000 km s^{-1} include 42 spectra and the signal to noise ratio is quite high (~ 70) as it is the usual value for the other composite spectra we built in this iron prominence interval. Figure 30 shows the fit and the residuals for the five models (L, V, G+G, V+G and L+G) and their residuals and their χ^2_ν values. It is evident that the double Gaussian model is the best suited for this bin, however, we cannot validate this conclusion to the level of the Lorentzian profile as it is made in the A1 spectral type.

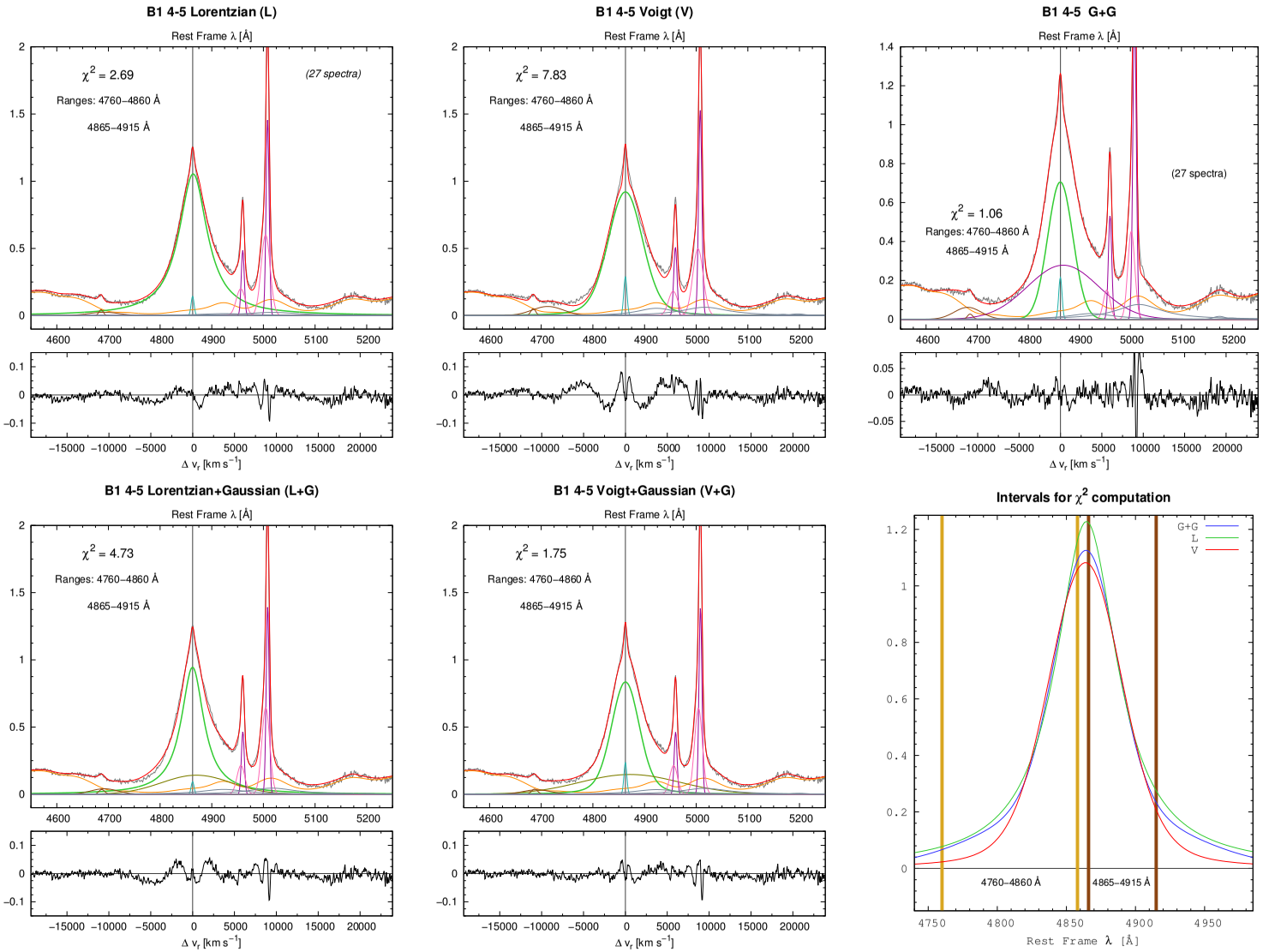

Figure 30: *Upper panel*, continuum subtracted spectra and fitting results for the bin B1 4000-5000 km s^{-1}. The horizontal scale is the rest-frame wavelength (Å) or velocity shift with the origin indicating rest-frame wavelength of the quasar measured on the narrow component (NC) of Hβ. *Lower panel*, fitting results for the bin B1 4000-5000 km s^{-1}. Each plot shows the evaluated χ^2_ν and the wavelength intervals considered in the computation. The last plot (bottom-right corner) depicts the wavelength intervals employed in the χ^2_ν computation over the different profiles of Hβ BC.

5.5 A2 and B2 populations

Fig. 31 Compares different iron prominence spectra. The upper panels compare the best model (Lorentzian) of the bin A1 2-3 and A2-2-3. The lower panel compare B1 4-5 and B2 4-5. At variance with the A spectral types, the double Gaussian represent very well the composite spectra of B1 and B2.

5.6 xA sources: A3, B3, A4, B4 populations

Some technical details that we employed in the analysis of the composite in this bins were.

- Host galaxy contamination and substracted with the model of Bruzual et al.
- Small correction in rest frame wavelength, solved by shifting respecto to the narrow component of Hβ.

We can appreciate from the residuals why the Lorentzian model is the best for the narrower profiles (Fig. 32). As shown in the Figures in the Appendix, for spectral types B3 and B4 the lines are clearly no more Lorentzian, although they retain a symmetric shape (Fig. 33).

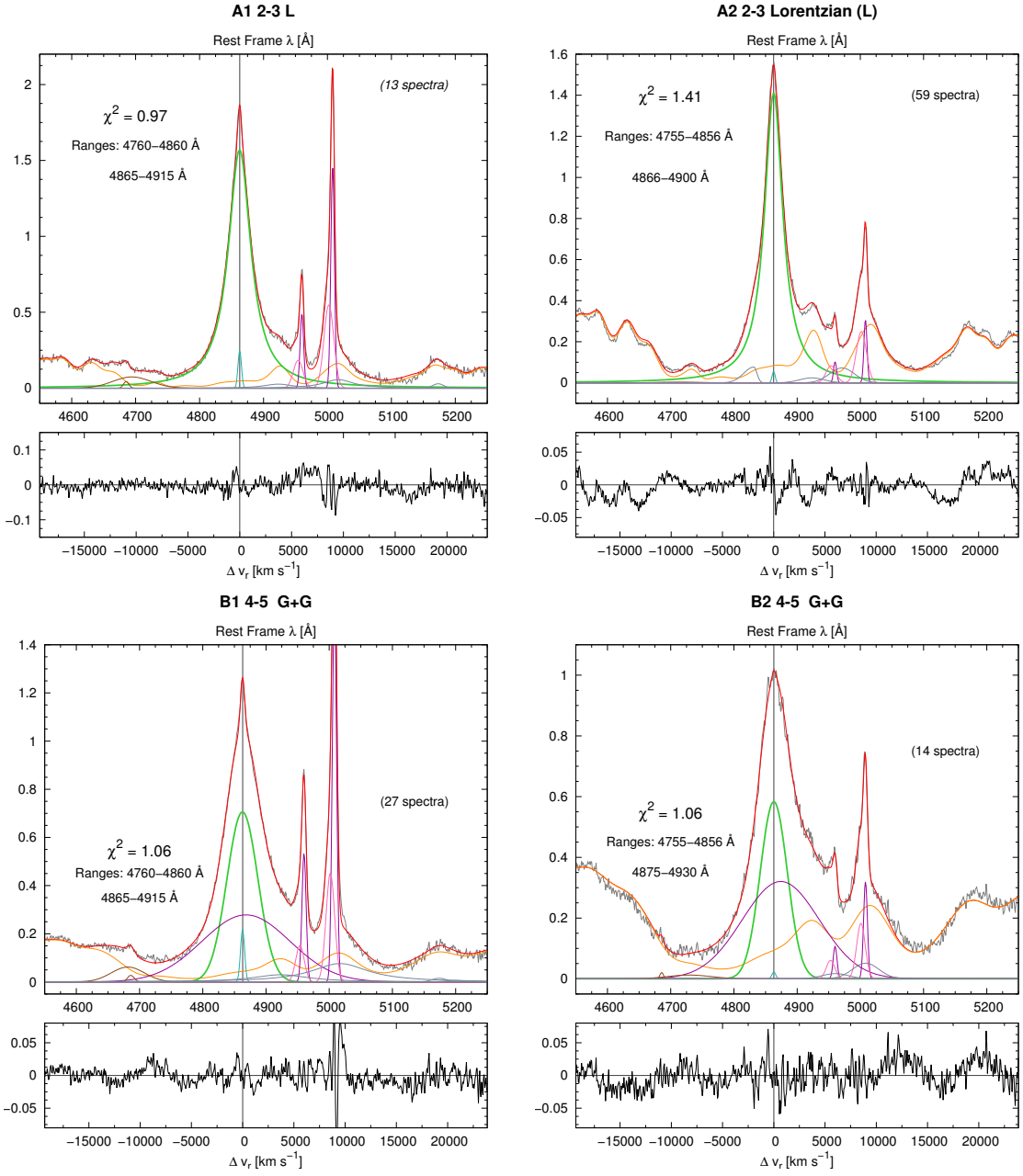

Figure 31: The upper panel compares the best model (Lorentzian) of the bin A1 2-3 and A2-2-3, the figures show the number of the spectra used for building the composite. The lower panel compare B1 4-5 and B2 4-5, in other words, show how the double Gaussian represent very well the composite spectra.

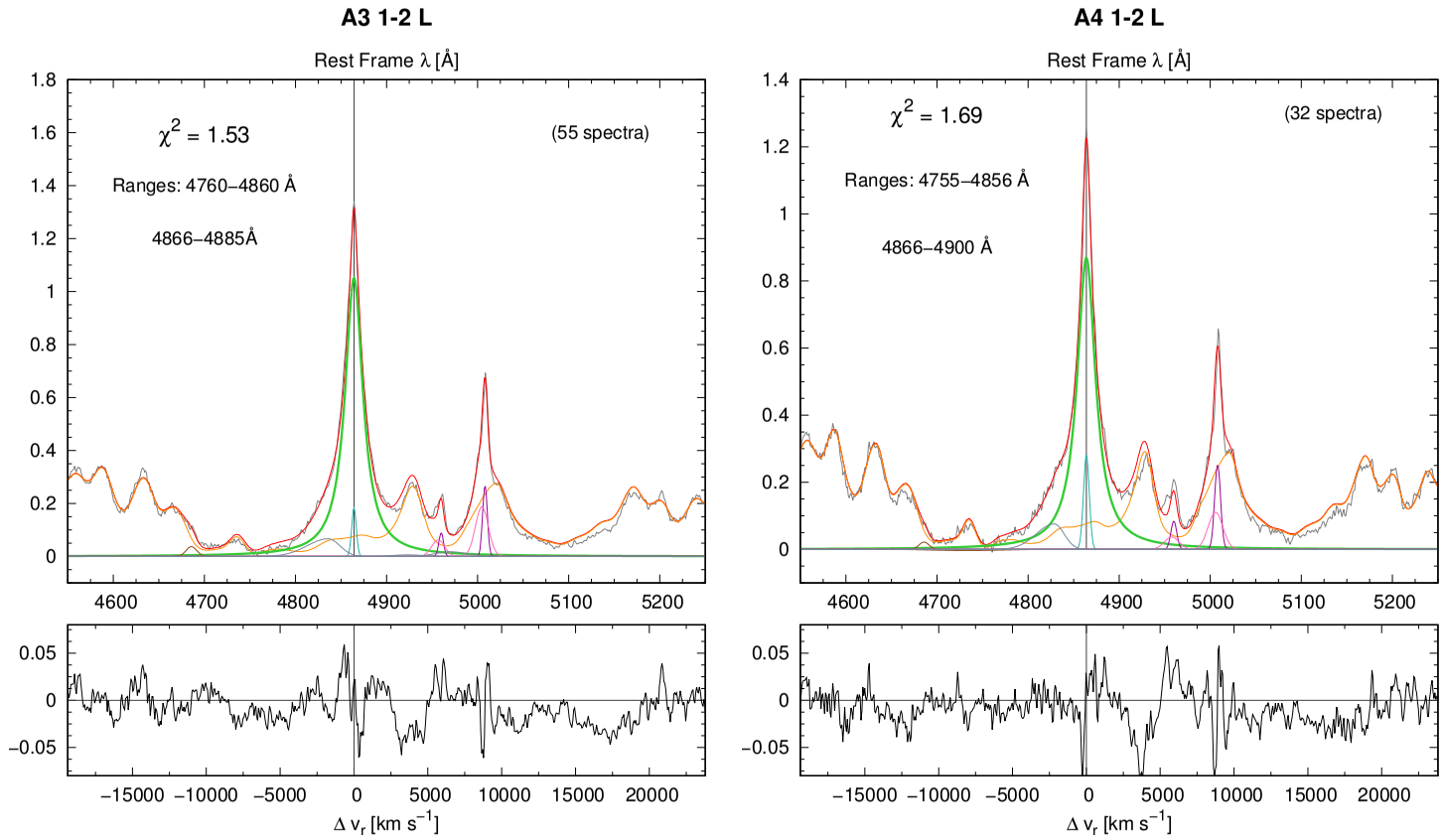

Figure 32: The bins with highest S/N ratio in the xA sources are presented. After testing all different models we can conclude that the Lorentzian is the most appropiate See the residuals on each plot. The comparison of the chi-square values are available in the Appendix.

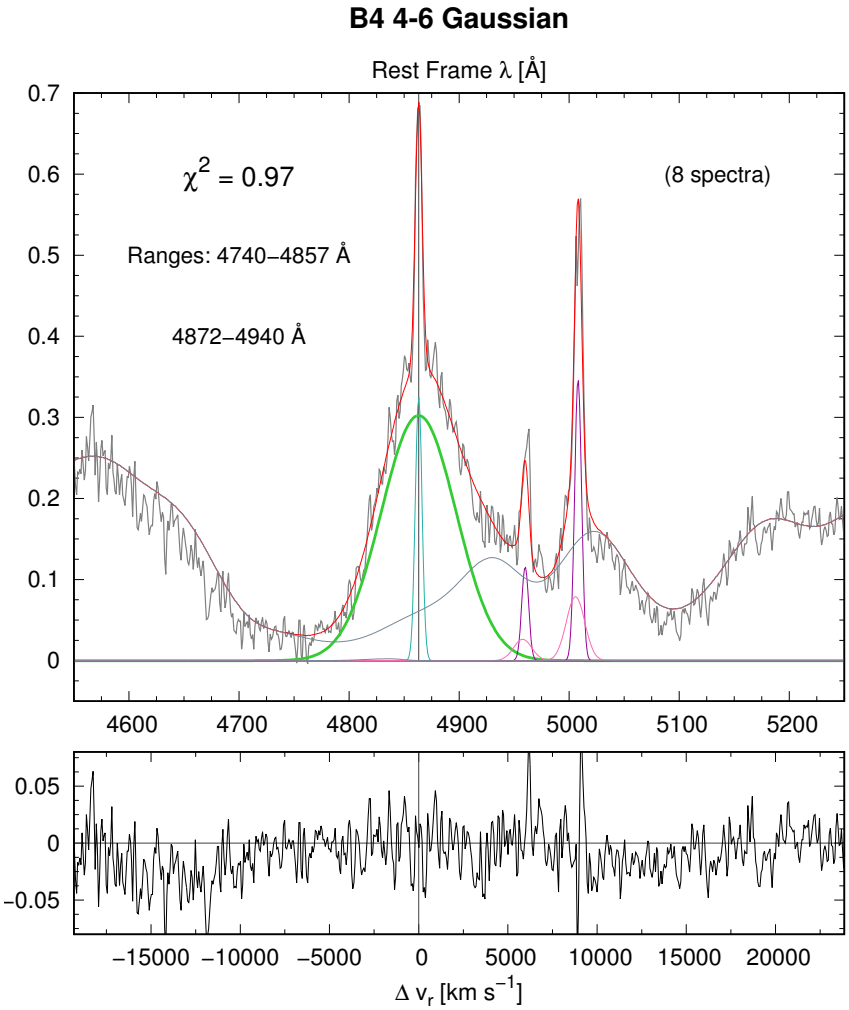

Figure 33: The bin B4 4000-6000 km s^{-1} is very particular when we compare it to the others: the profile seems to be a single red Gaussian, as may be expected. This kind of sources may be a good indicator of orientation effects (Marziani et al. 2001).

5.7 Concluding remarks on reduced spectral bins

What kind of confirmation did we arrive with a reduced bin with ΔFWHM(Hβ)? We reaffirm the A/B populations transition on the Hβ from Lorentzian to a double gaussian. Contrary to what Kollatschny & Zetzl (2011) state, there is a clear and marked transition from FWHMβ =3000-4000 km s^{-1} to FWHMβ= 4000 to 5000 km s^{-1}. Lorentzian profile is the best model to represent narrow xA accretors.

Chapter 6

xA accretors and Luminosity estimation

In this Chapter we will briefly consider a preliminary application of the virial luminosity equation (Eq. 3.11 in Chapter 3), for an eventual application in a cosmological context. To this aim, we will

1. restriction ourselves to xA sources;

2. use the sample of xA sources of Negrete et al. 2017, in preparation.

6.1 The Hβ profile in xA accretors

The Hβ line profile has been analyzed following several different methods. The Appendix A provides a summary of the goodness of fits in the Tables and shows the results of the fits and of the residuals. For each fit, the normalized χ^2, the fitting range, and the number of spectra used for the composite are reported.

6.1.1 Virial broadening in Hβ profile

The main source of broadening in the Hβ profile is expected to be virial. However, from the considerations made in the previous chapter, we expect that LIL emission occurs in a highly flattened configuration. If this is the case, then we expect a strong dependence of the line width on the angle between the symmetry axis of the structure and the line-of-sight.

6.1.2 Blueshifted emission in xA accretors

In the most extreme quasars, the FWHM is artificially widened due to the presence of two components in Hβ. In these objects, FeII is extremely strong, and/or a very intense blueshifted component of Hβ appears. Profile fittings requires the addition of a blue shifted component which is also expected to provide non-virial additional broadening to the Hβ line. Fig. 34 shows the interpretation of the Hβ broad profile.

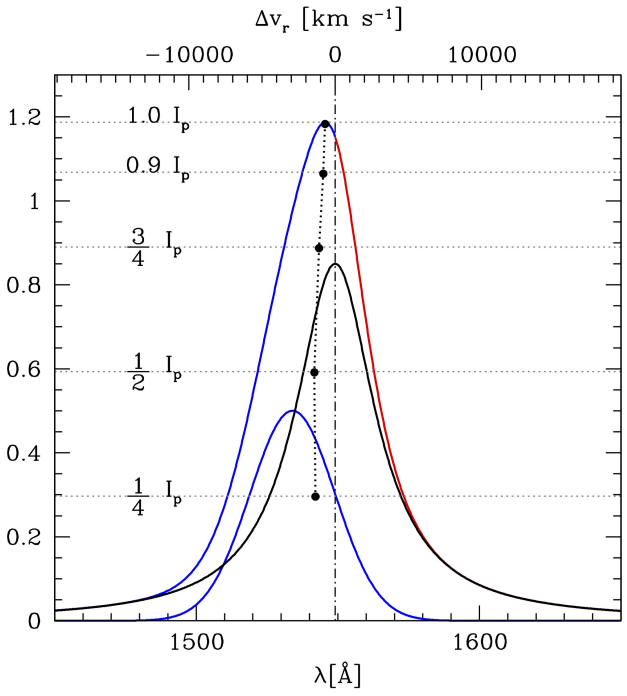

Figure 34: Interpretation of line profiles, for Pop A. Fractional intensity levels where line centroids are measured are identified. Mock profiles are shown to represent the bare broad profile of any of the strongest emission lines of quasars. The left one is built on 2 components, as appropriate for Pop. A, which are the BC and a blue shifted excess BLUE. The blue shifted component is strong in HILs and weak in LILs.

6.2 Luminosity estimation

We follow here the approach followed in this paper has been to consider Eq. 3.11 in the form $L \approx \mathcal{L}_0 \delta v^4$, where $\mathcal{L}_0$ has been set by the best guess of the quasar parameters with $\lambda_{\rm Edd} \rightarrow 1$. This will imply a value of h^{-1}, and to ignore source-by-source diversity.

We then consider the luminosity computed following the standard approach based on redshift and knowledge of the cosmological constant. As mentioned in Chapter 3, the luminosity distance $d_L = d_C \cdot (1+z)$ can be computed as follows

$$d_{\rm L} = d_{\rm H} \int_0^z \frac{dz'}{E(z')} \cdot (1+z) \tag{6.1}$$

$$L(z) = 4\pi d_{\rm L}^2 f_\lambda \lambda \tag{6.2}$$

where $f_\lambda \lambda$ is the flux in the observed reference frame.

6.2.1 Comparison with the sample of Negrete et al. 2017, in preparation

Here we take advantage of the work of Negrete et al. 2017 who kindly made available their sample, and their full set of `specfit` results for our thesis work. In order to have a good representation of a low redshift extreme quasar sample, Negrete et al. used as a basis the Sloan Digital Sky Survey Data Release 7 [1].

The quasar sample presented by Shen et al. (2011), consists in 105,783 spectra taken from the SDSS DR7 data base. For a detailed analysis of the quasars with high accretion rates, we need to select only those spectra with good quality that meet the criteria described by the E1 parameter space. Initially Negrete et al. used the following filters:

1. Negrete et al. selected quasars with $z \lesssim 0.8$ to cover the range around Hβ and include the FeII blends around 4570 and 5260Å. As a first approximation, we use the z provided by the SDSS. With this criteria, they selected 19,451 spectra. We detected 103 spectra with an erroneous z identification which were eliminated, also for being noisy.

2. For the spectra selected in the previous point, Negrete et al. performed automatic measurements using the IRAF task *splot*, to estimate the signal-to-noise ratio (S/N) around 5100Å. We took three windows of 50Å to avoid effects of local noise. Those with S/N$\lesssim$ 15 (76.5% of this sub sample), are practically pure noise. Spectra with S/N between 15 and 20 are still very bad, and we can vaguely guess where the emission lines would be. Therefore, they can not be used since the measurements would have big errors. In this way, we find that only those spectra with S/N $\gtrsim$ 20 have the minimum quality necessary to make reliable measurements. This represents only 14.1% of the objects of the sample of point 1, i.e. 2,734 spectra. This illustrates how important is to consider only good quality spectra, especially when performing automatic measurements. However, even considering only such spectra, the automatic measurements can introduce up to 30% additional error. For this reason, when working with

[1] http://skyserver.sdss.org/dr7

databases where the vast majority of data are very noisy, one might introduce errors as large and even larger than 80%.

3. The principal criteria that we use to isolate extreme quasars is that their $R_{FeII} \gtrsim 1$. In order to determine this ratio, Negrete et al. performed automatic measurements on the objects selected as described in point 2. First we normalized all the spectra by the value of their continuum at 5100 Å. Subsequently, in order to estimate R_{FeII}, Negrete et al. measured roughly the EW of FeII and Hβ in the ranges 4435-4686 and 4776-4946Å respectively (Boroson & Green 1992). Negrete et al. selected 468 objects with $R_{FeII} \gtrsim 1$. At this point, we further rejected 134 more spectra that are either noisy or intermediate type (Sy 1.5), i.e., the Hβ broad component (Hβ_{BC}) is weak compared to its narrow component, which usually is very intense.

The final selection is a sample consist of 334 spectra, subdivided in spectral bin according to Sulentic et al. (2002). We used the median values of the luminosity in the finer bin subdivision employed in our work.

6.2.2 Virial and redshift-based luminosity: a first comparison

The results of the luminosity computations along with the number of sources are reported in Table 6.1

Table 6.1: Luminosity comparison

N	Bin	FWHM	L_{vir}	$L(z)$
16	"A3-0-1"	500	44.500	45.4612
55	"A3-1-2"	1500	45.559	45.7474
41	"A3-2-3"	2500	46.256	45.93
8	"A3-3-4"	3500	46.666	45.75
9	"B3-4-5"	4500	47.31	45.697
8	"B3-5-6"	5500	47.78	45.659
9	"B3-6-8"	7000	47.24	46.772
11	"A4-0-1"	500	44.84	45.46
32	"A4-1-2"	1500	45.61	45.74
20	"A4-2-3"	2500	45.96	45.93
8	"B4-4-6"	5000	47.67	45.65

Fig. 35 shows a comparison between the computation of the virial luminosity and the

median values computed from the individual sources in the bins as a function of FWHM, for the A3/B3 bins. The central bin FWHM as well as the number of sources and the luminosity values are reported in Table 6.1. The $L_{\rm vir}$ has been computed from the best fitting model as reported in the Appendix.

Fig. 36 shows the same trends, but for the A4/B4 bins.

We infer two main results:

1. The spectral bins with the largest numbers (between 1000 and 3000 km s^{-1}) show a very good agreement between the two L estimates, both for the 3 and the 4 group of spectral bins.

2. there is a systematic trend: at low FWHM, the $L_{\rm vir}$ is much lower than $L(z)$, while it becomes significantly larger above 3000 km s^{-1}.

These trends confirm the validity of the $L_{\rm vir}$ estimates for the 2/3 of the sources. The discrepancy is most likely to orientation effects: the width of the Hβ is expected to be roughly proportion to $\sin\theta$, where θ is the angle between the symmetry axis of the structure and the line-of-sight (Collin et al. 2006).

These considerations are preliminary. The results will be amply discussed in further work that will consider the change in profile shape between the A and B FWHM ranges.

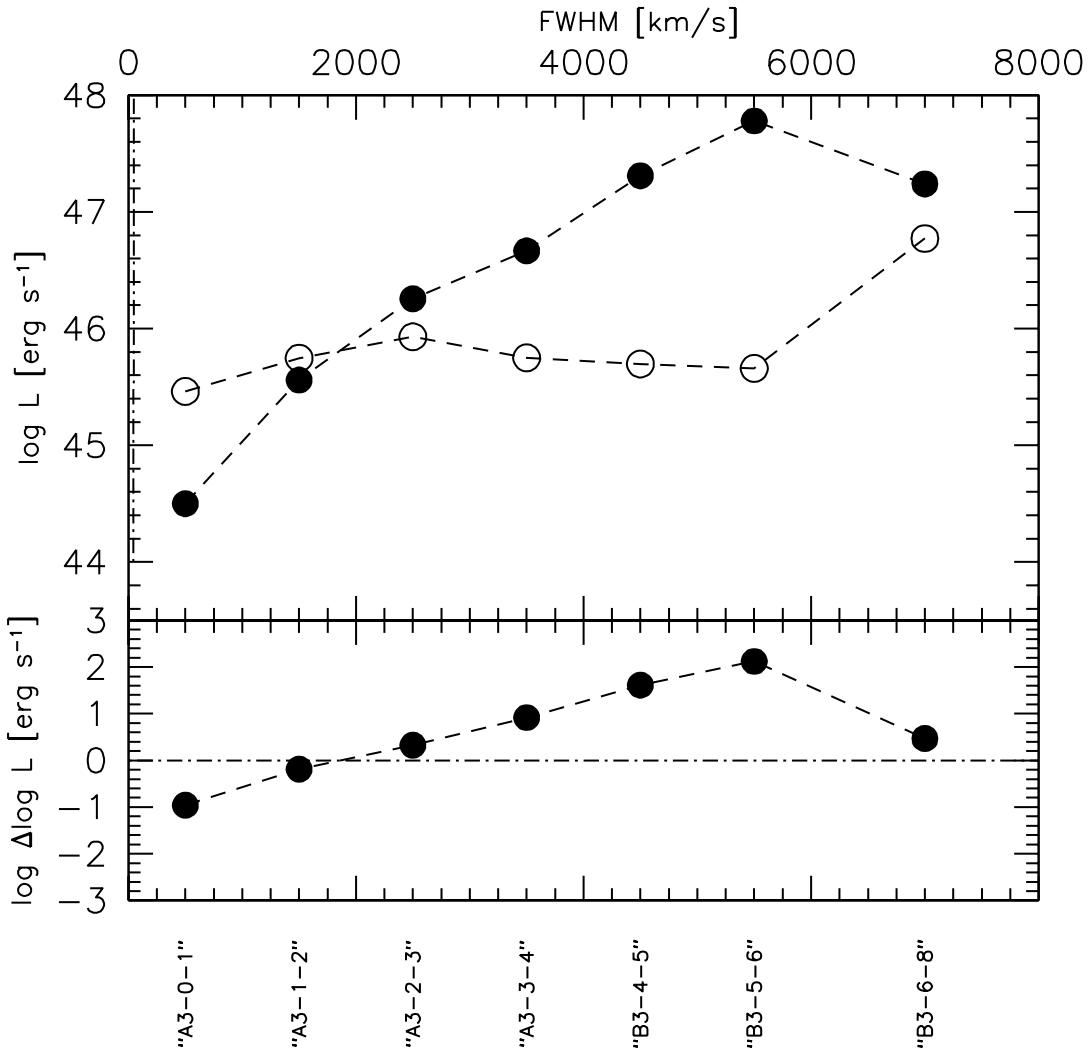

Figure 35: Comparison between virial and redshift-based luminosity for the A3-B3 spectral types, as a function of FWHM.

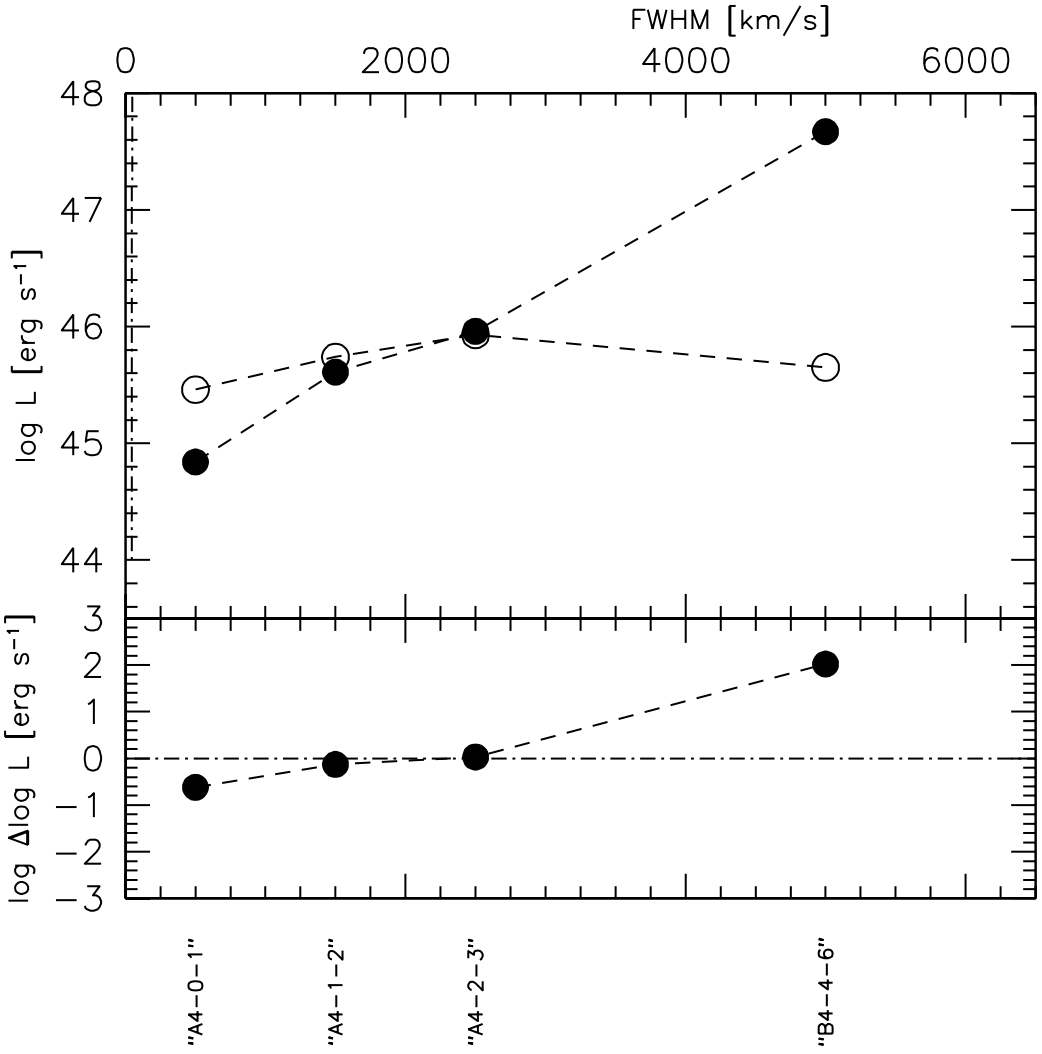

Figure 36: Comparison between virial and redshift-based luminosity for the A4-B4 spectral types, as a function of FWHM.

Chapter 7

General conclusions

This thesis has first summarized the basic properties of AGN, focusing on type-1 AGN, then narrowing to focus to the extreme Population A or extremely accreting sources. We have considered several recent developments:

- the ability to organize quasar diversity following the Eigenvector 1 correlations (Chapter 2);
- the ability to recognize sources that are highly accreting because of their unique properties;
- the methods that want to exploit these sources for the computations of the cosmological parameters (Chapter 3);
- the interpretation of the broad-line spectra in terms of a disk+wind system, that is consistent with the observational data (Chapter 4).

Starting from this, we obtained the following results:

- The analysis of the Hβ profile shape along the MS of quasars, with several model profiles applied to composite spectra in the spectral types defined by Sulentic et al. (2002), with a finer subdivision in terms of line widths.
- The narrowest profiles show a Lorentzian shape.
- A clear change occurs around FWHM H$\beta\approx$ 4000 km s^{-1} and not at 2000 km s^{-1}, in correspondence of the separation between NLSy1s and broader AGN. This confirms

the early suggestion of Sulentic et al. (2002) and Marziani et al. (2003b), as well as the most recent one by Cracco et al. (2016).

- Broader profiles show a redward asymmetry and best models that involve a Voigt profile or a Gaussian representative of the BC + a redshifted Gaussian representative of the VBC, probably associated with the innermost part of the Balmer line emitting regions. This result can be interpreted in terms of a virialized system.

- A blue shifted component is detected in several spectral types, most notably A3 and A4. This blueshifted excess is weak but is likely to be associated with the much stronger blueshifts observed in narrow- and broad HILs.

- If the virial luminosity equation is applied to xA sources, we have preliminarily analyzed the virial luminosity estimate using the FWHM from our best fitting model. This emphasizes that for an eventual cosmological application an orientation correction should be applied to the FWHM values.

Future work could extend the comparison between luminosity estimates from the virial equation and luminosity estimates from concordance cosmology. Systematic differences are likely to give information on orientation of quasars, and may also reveal a difference in individual luminosity estimates associated with the parameters entering the virial luminosity equation of Chapter 3.

Appendix A

Appendix

A.1 χ^2_ν and F-test results

Table A.1: χ^2_ν values and F values for bins located at $0.0 < R_{\rm Fe\ II} < 0.5$.

	Model→	L	V	G+G	V+G	L+G	RMS	#	F	F	F	F	Best	CL
							$\times 10^3$	CS	(V,L)	(G+G,L)	(V,G+G)	(G+G,V+G)	Model	(σ)
(1)	(2)	(3)	(4)	(5)	(6)	(7)	(8)	(9)	(10)	(11)	(12)	(13)	(14)	(15)
Type	**Bin↓**													
	1-2	1.10	4.73	2.76	—	—	33	4	4.29	2.50	1.71	—	L	3
A1	2-3	0.97	10.95	5.07	—	—	19	13	11.3	5.22	2.16	—	L	3
	3-4	1.45	9.13	2.06	2.39	4.44	13	28	6.28	1.41	4.44	1.16	L	1
	4-5	2.69	7.83	1.06	1.75	4.73	14	27	2.91	2.54	7.39	1.65	G+G	2
B1	5-6	—	2.99	1.01	1.04	—	13	27	—	—	2.96	1.03	G+G	0
	6-7	—	1.79	1.04	0.90	—	13	36	—	—	1.73	1.15	V+G	1
	7-8	—	1.48	1.44	0.89	—	13	42	—	—	1.03	1.62	V+G	2
	8-9	—	1.37	1.21	1.12	—	12	42	—	—	1.13	1.08	V+G	0
B1+	9-10	—	1.31	1.20	1.27	—	13	37	—	—	1.09	1.06	G+G	0
	10-11	—	1.57	1.47	1.43	—	14	25	—	—	1.07	1.03	V+G	0
	11-12	—	1.66	1.60	1.56	—	17	23	—	—	1.04	1.03	G+G	0
	12-13	—	1.07	1.29	1.09	—	24	18	—	—	1.21	1.18	V+G	1
B1++	13-14	—	1.55	1.39	1.36	—	24	8	—	—	1.11	1.02	V+G	0
	14-16	—	1.22	1.32	1.25	—	38	5	—	—	1.08	1.05	V+G	0
B1+++	16-20	—	1.02	1.02	1.05	—	28	10	—	—	1.00	1.02	G+G	0

Table A.2: χ^2_ν values and F values for bins located at $0.0 < R_{\rm Fe\ II} < 0.5$ with extended interval on computation.

	Model→	L	V	G+G	V+G	L+G	RMS	#	F	F	F	F	Best	CL
							$\times 10^3$	CS	(V,L)	(G+G,L)	(V,G+G)	(G+G,V+G)	Model	(σ)
(1)	(2)	(3)	(4)	(5)	(6)	(7)	(8)	(9)	(10)	(11)	(12)	(13)	(14)	(15)
Type	**Bin↓**													
	1-2	1.25	3.75	2.20	—	—	33	4	3.01	1.76	1.71	—	L	3
A1	2-3	0.88	7.06	3.70	—	—	19	13	8.0	4.19	1.91	—	L	3
	3-4	1.17	5.88	1.49	1.67	3.03	13	28	5.03	1.28	3.94	1.12	L	1
	4-5	2.07	5.08	0.97	1.43	3.22	14	27	2.45	2.13	5.22	1.47	G+G	2
B1	5-6	—	2.21	0.87	0.93	—	13	27	—	—	2.55	1.07	G+G	1
	6-7	—	1.65	1.15	1.23	—	13	36	—	—	1.43	1.07	G+G	1
	7-8	—	1.44	1.32	0.94	—	13	42	—	—	1.09	1.41	V+G	2
	8-9	—	1.32	1.20	1.11	—	12	42	—	—	1.10	1.08	V+G	1
B1+	9-10	—	1.13	0.97	1.04	—	13	37	—	—	1.16	1.07	G+G	1
	10-11	—	1.57	1.31	1.26	—	14	25	—	—	1.20	1.04	G+G	0
	11-12	—	1.36	1.29	1.32	—	17	23	—	—	1.05	1.02	V+G	0
	12-13	—	0.93	1.04	0.90	—	24	18	—	—	1.12	1.15	G+G	1
B1++	13-14	—	1.24	1.03	1.01	—	24	8	—	—	1.20	1.02	G+G	0
	14-16	—	1.15	1.13	1.12	—	38	5	—	—	1.02	1.01	G+G	0
B1+++	16-20	—	1.05	1.03	1.04	—	28	10	—	—	1.02	1.01	V+G	0

Table A.3: χ^2_ν values and F values for bins located at $0.5 < R_{\rm Fe\ II} < 1.0$.

	Model→	L	V	G+G	V+G	L+G	RMS	#	F	F	F	F	Best	CL
							$\times 10^3$	CS	(V,L)	(G+G,L)	(V,G+G)	(G+G,V+G)	Model	(σ)
(1)	(2)	(3)	(4)	(5)	(6)	(7)	(8)	(9)	(10)	(11)	(12)	(13)	(14)	(15)
Type	**Bin↓**													
	1-2	1.12	3.14	1.59	—	—	29	7	2.80	1.42	1.97	—	L	2
A2	2-3	1.41	7.49	4.9	—	—	12	59	5.3	3.48	1.53	—	L	3
	3-4	2.29	5.99	1.27	2.64	4.44	9.9	70	2.62	1.82	4.72	2.08	G+G	2
	4-5	1.11	3.07	1.06	1.34	1.06	20	14	2.77	1.05	2.90	1.26	G+G	1
B2	5-6	—	1.95	2.29	2.34	—	23	10	—	—	1.18	1.02	G+G	0
	6-7	—	2.71	1.37	1.36	—	27	6	—	—	1.98	1.01	V+G	0

Table A.4: χ^2_ν values and F values for bins located at $1.0 < R_{\rm Fe\ II} < 1.5$.

	Model→	L	V	G+G	V+G	L+G	RMS	#	F	F	F	F	Best	CL
							$\times 10^3$	CS	(V,L)	(G+G,L)	(V,G+G)	(G+G,V+G)	Model	(σ)
(1)	(2)	(3)	(4)	(5)	(6)	(7)	(8)	(9)	(10)	(11)	(12)	(13)	(14)	(15)
Type	**Bin↓**													
	0-1	1.85	1.92	3.86	—	—	26	16	1.04	2.09	2.00	–	L	0
A3	1-2	1.53	3.14	4.69	—	—	20	55	2.05	3.07	1.67	—	L	3
	2-3	1.65	1.10	1.21	—	—	21	41	1.67	1.38	1.10	—	V	1
	3-4	0.92	1.44	0.94	0.85	1.01	24	8	1.57	1.02	1.53	1.11	V+G	1
	4-5	1.40	0.90	0.89	0.81	1.28	23	9	1.56	1.56	1.01	1.10	V+G	1
B3	5-6	—	1.39	1.19	1.31	—	20	8	—		1.17	1.10	G+G	1
	6-8	—	1.45	1.193	1.194	—	20	9	—		1.22	1.00	G+G	0

Table A.5: χ^2_ν values and F values for bins located at $1.5 < R_{\rm Fe\ II} < 2.0$.

	Model→	L	V	G+G	V+G	L+G	RMS	#	F	F	F	F	Best	CL
							$\times 10^3$	CS	(V,L)	(G+G,L)	(V,G+G)	(G+G,V+G)	Model	(σ)
(1)	(2)	(3)	(4)	(5)	(6)	(7)	(8)	(9)	(10)	(11)	(12)	(13)	(14)	(15)
Type	**Bin↓**													
	0-1	1.66	1.44	3.22	—	—	23	11	1.15	1.93	2.22	–	V	1
A4	1-2	1.69	2.88	2.08	—	—	18	32	1.67	1.23	1.38	—	L	2
	2-3	1.27	1.03	1.63	—	—	18	20	1.23	1.29	1.59	—	V	1
	3-4	—	—	—	—	—	—	3	—	—	—	—	—	—
B4	4-6	2.20	0.99	0.97	—	—	29	8	1.15	1.94	2.22	–	G+G	0

A.2 Plots of the fitting results (Full display)

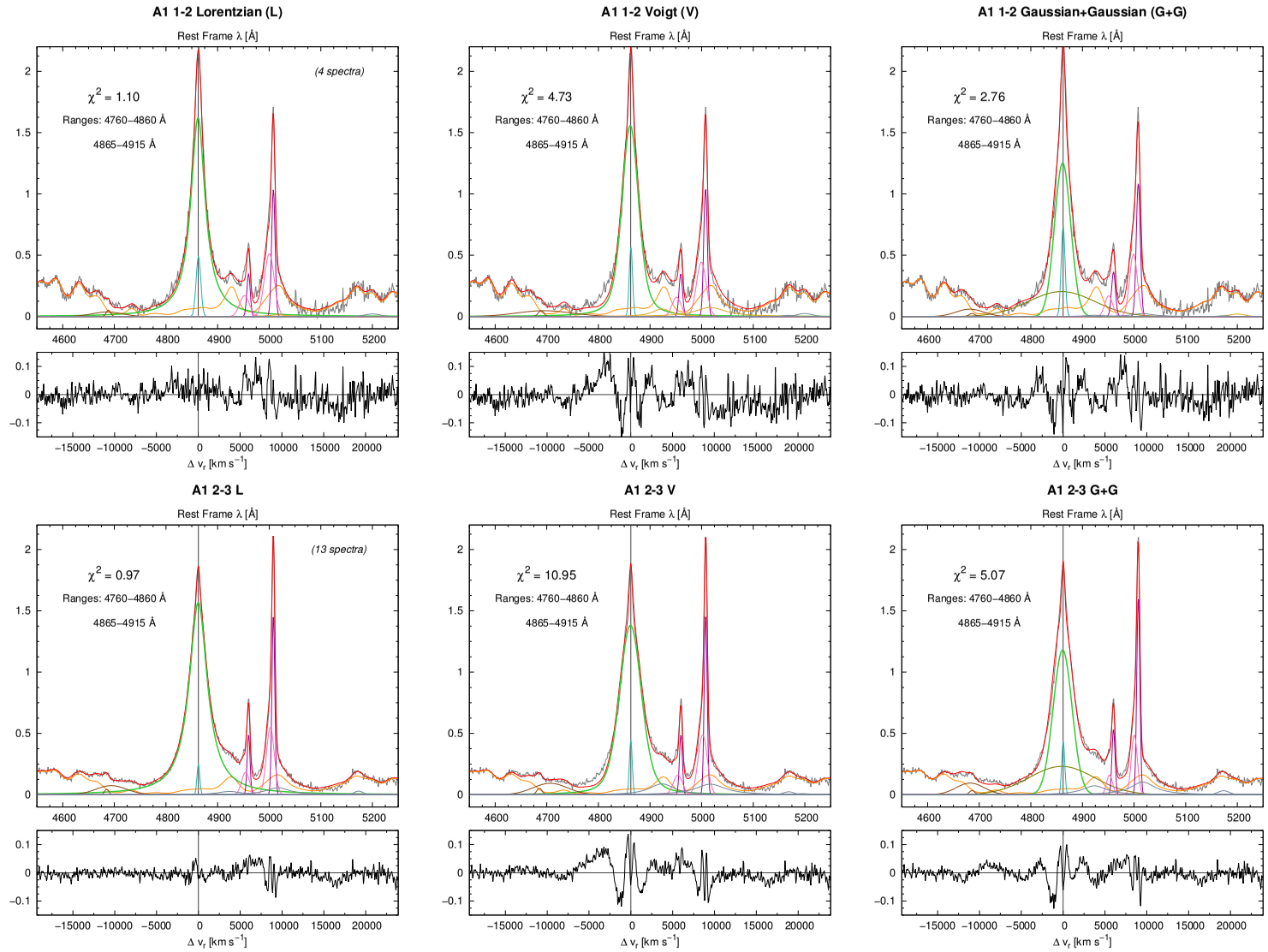

Figure 37: *Upper panel*, continuum subtracted spectra and fitting results for the bin A1 1000-2000 km s^{-1}. The horizontal scale is the rest-frame wavelength (Å) or velocity shift with the origin indicating rest-frame wavelength of the quasar measured on the narrow component (NC) of Hβ. *Lower panel*, fitting results for the bin A1 2000-3000 km s^{-1}. Each plot shows the evaluated χ^2_ν and the wavelength intervals considered in the computation.

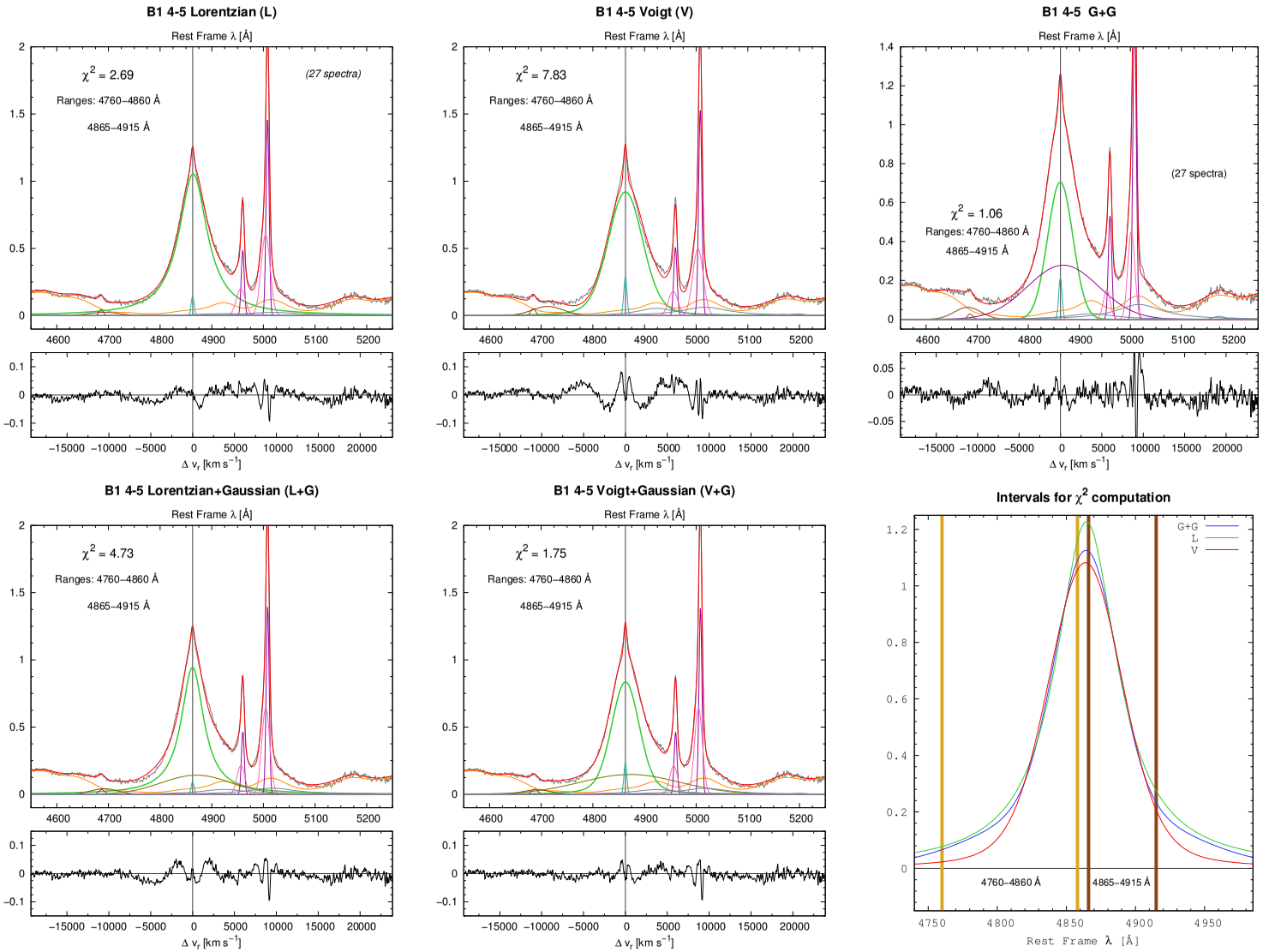

Figure 38: *Upper panel*, continuum subtracted spectra and fitting results for the bin B1 4000-5000 km s^{-1}. The horizontal scale is the rest-frame wavelength (Å) or velocity shift with the origin indicating rest-frame wavelength of the quasar measured on the narrow component (NC) of Hβ. *Lower panel*, fitting results for the bin B1 4000-5000 km s^{-1}. Each plot shows the evaluated χ^2_ν and the wavelength intervals considered in the computation. The last plot (bottom-right corner) depicts the wavelength intervals employed in the χ^2_ν computation over the different profiles of Hβ BC.

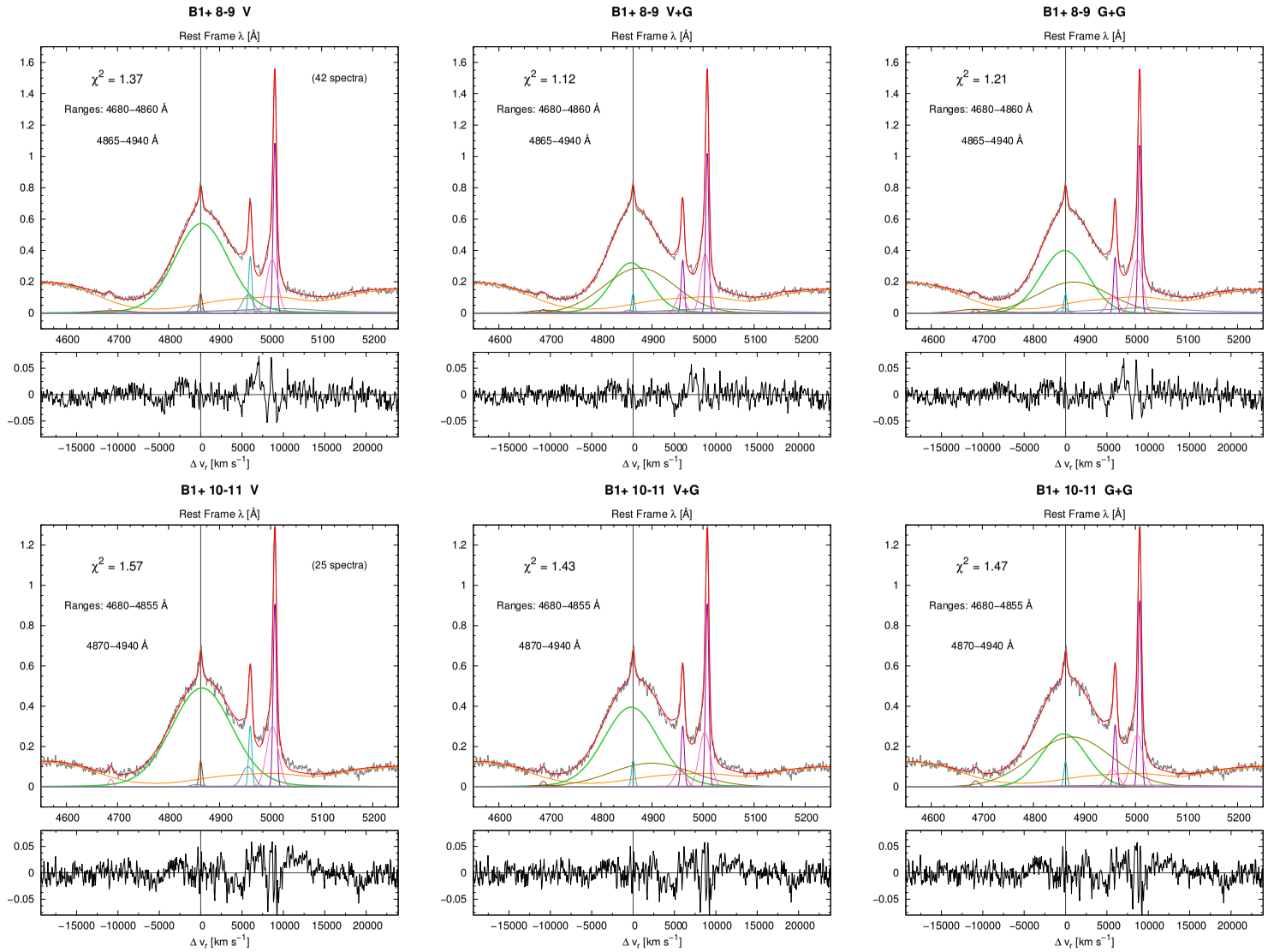

Figure 39: *Upper panel*, continuum subtracted spectra and fitting results for the bin B1+ 8000-9000 km s^{-1}. The horizontal scale is the rest-frame wavelength (Å) or velocity shift with the origin indicating rest-frame wavelength of the quasar measured on the narrow component (NC) of Hβ. *Lower panel*, fitting results for the bin B1+ 10,000-11,000 km s^{-1}. Each plot shows the evaluated χ^2_ν and the wavelength intervals considered in the computation. The last plot (bottom-right corner) depicts the wavelength intervals employed in the χ^2_ν computation over the different profiles of Hβ BC.

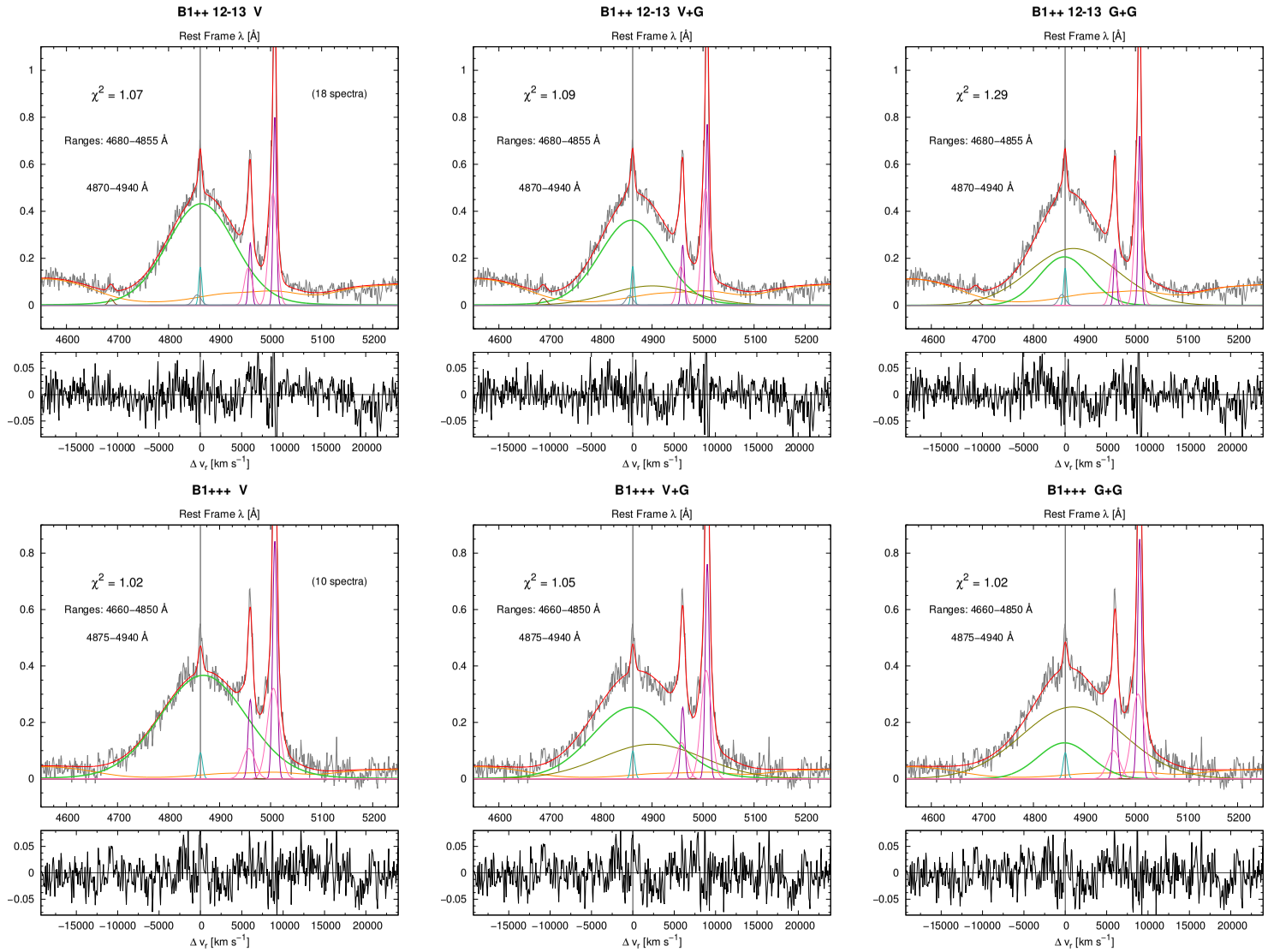

Figure 40: *Upper panel*, continuum subtracted spectra and fitting results for the bin B1+ 12,000-13,000 km s^{-1}. The horizontal scale is the rest-frame wavelength (Å) or velocity shift with the origin indicating rest-frame wavelength of the quasar measured on the narrow component (NC) of Hβ. *Lower panel*, fitting results for the bin B1+++. Each plot shows the evaluated χ^2_ν and the wavelength intervals considered in the computation.

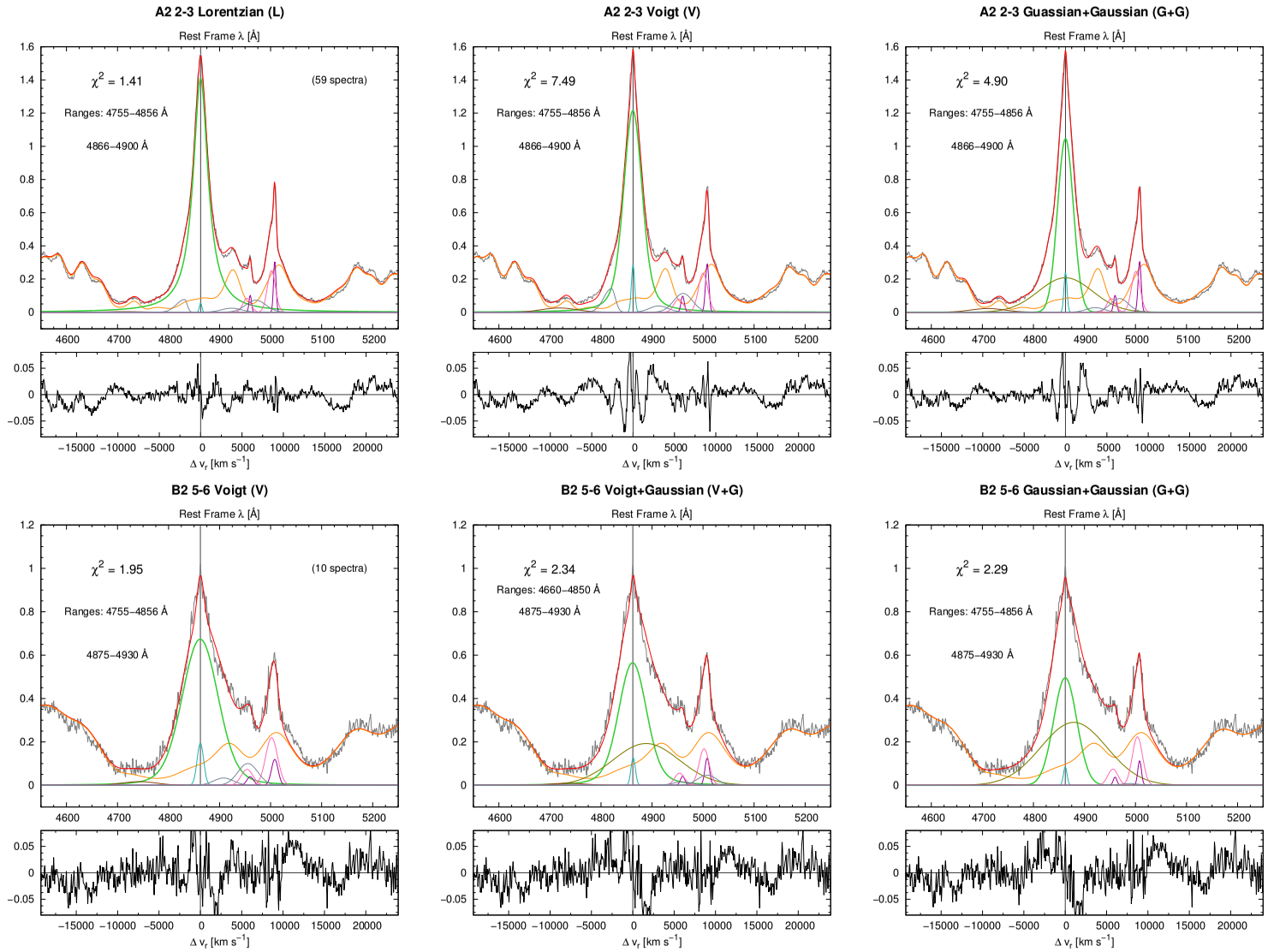

Figure 41: *Upper panel*, continuum subtracted spectra and fitting results for the bin A2 2,000-3,000 km s^{-1}. The horizontal scale is the rest-frame wavelength (Å) or velocity shift with the origin indicating rest-frame wavelength of the quasar measured on the narrow component (NC) of Hβ. *Lower panel*, fitting results for the bin B2 5-6. Each plot shows the evaluated χ^2_ν and the wavelength intervals considered in the computation.

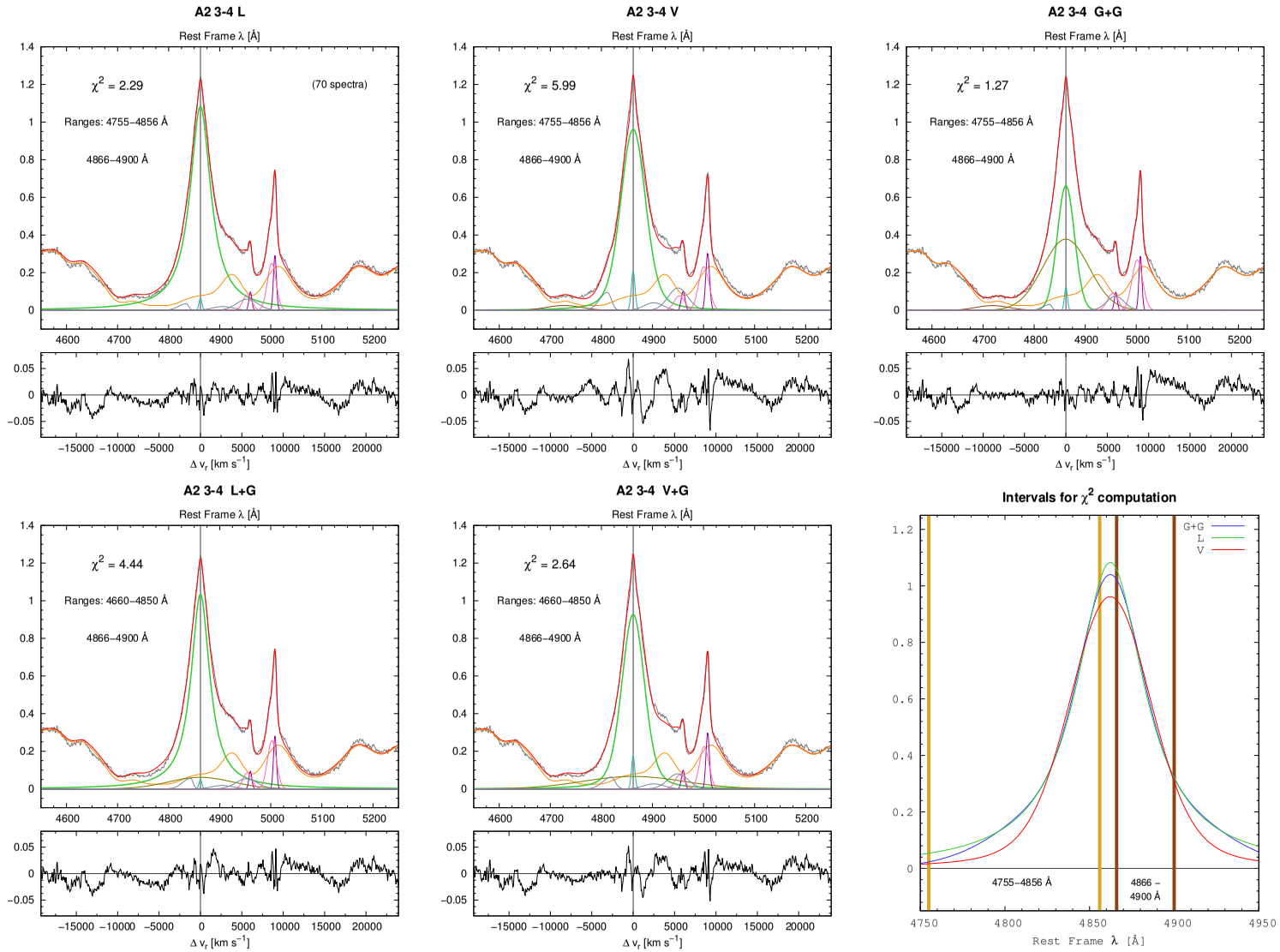

Figure 42: *Upper panel*, continuum subtracted spectra and fitting results for the bin A2 3000-4000 km s^{-1}. The horizontal scale is the rest-frame wavelength (Å) or velocity shift with the origin indicating rest-frame wavelength of the quasar measured on the narrow component (NC) of Hβ. *Lower panel*, fitting results for the bin A2 3000-4000 km s^{-1}. Each plot shows the evaluated χ^2_ν and the wavelength intervals considered in the computation. The last plot (bottom-right corner) depicts the wavelength intervals employed in the χ^2_ν computation over the different profiles of Hβ BC.

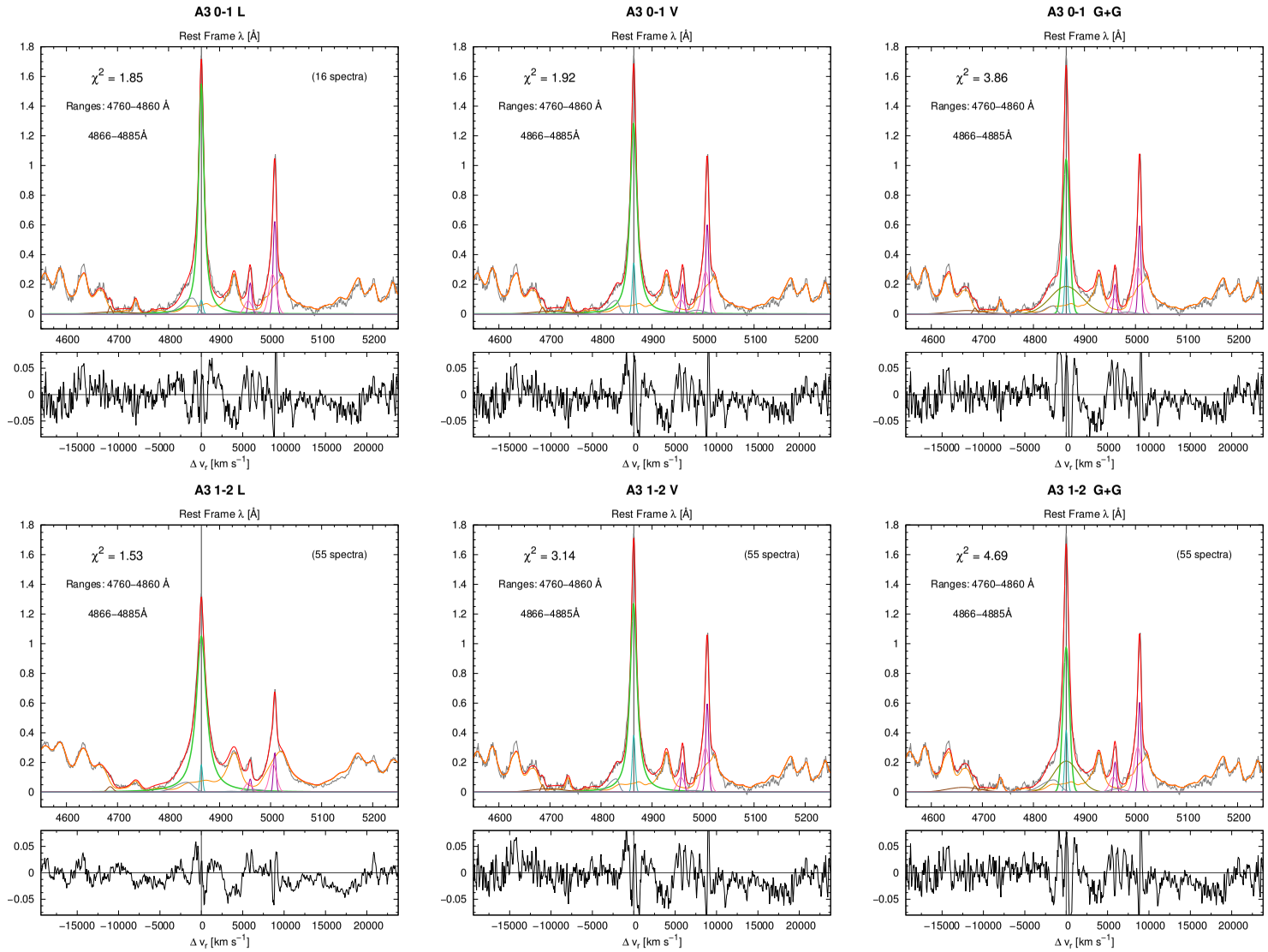

Figure 43: *Upper panel*, continuum subtracted spectra and fitting results for the bin A3 0-1000 km s^{-1}. The horizontal scale is the rest-frame wavelength (Å) or velocity shift with the origin indicating rest-frame wavelength of the quasar measured on the narrow component (NC) of Hβ. *Lower panel*, fitting results for the bin A2 3000-4000 km s^{-1}. Each plot shows the evaluated χ^2_ν and the wavelength intervals considered in the computation. The last plot (bottom-right corner) depicts the wavelength intervals employed in the χ^2_ν computation over the different profiles of Hβ BC.

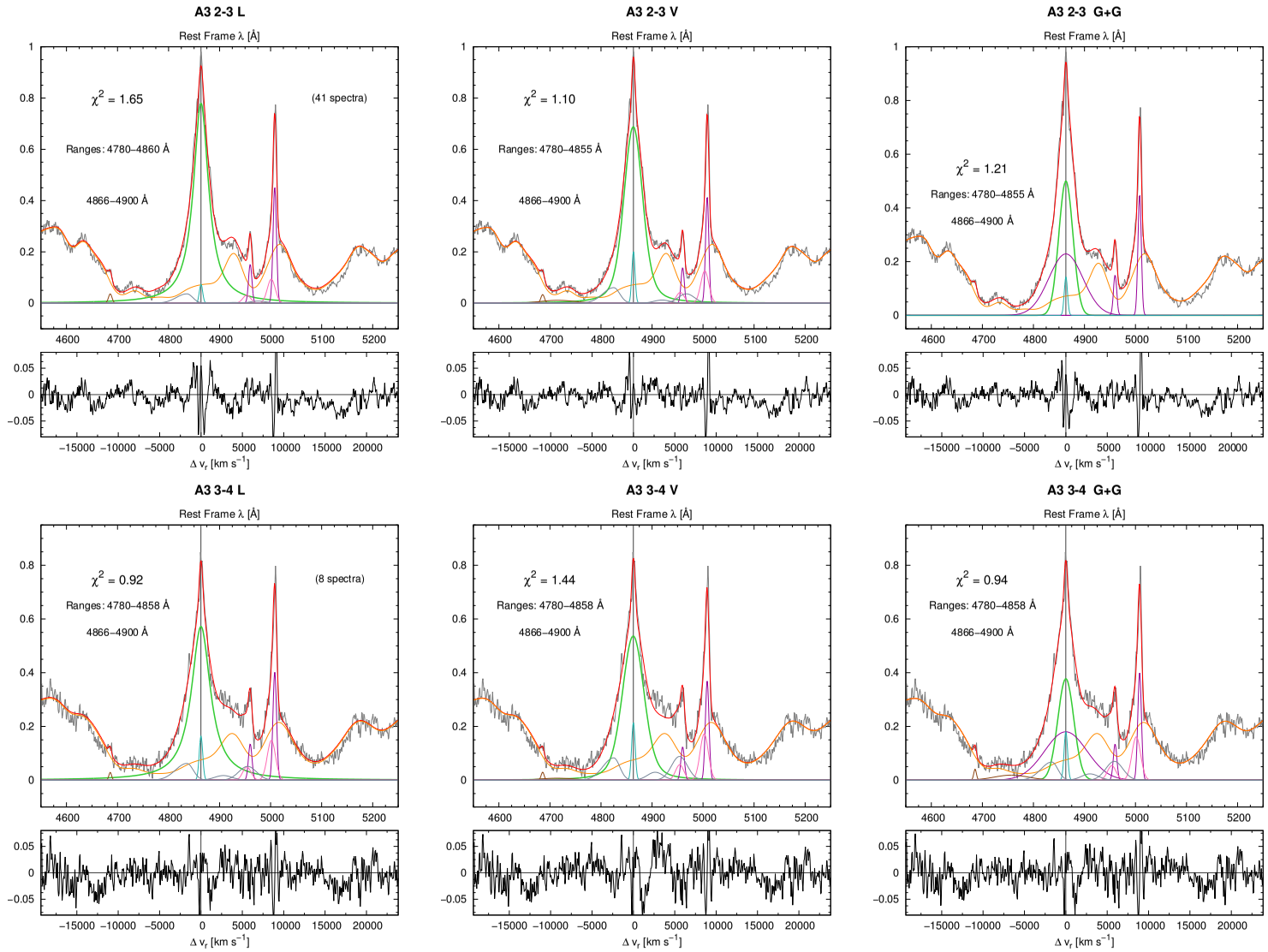

Figure 44: *Upper panel*, continuum subtracted spectra and fitting results for the bin A3 2000-3000 km s^{-1}. The horizontal scale is the rest-frame wavelength (Å) or velocity shift with the origin indicating rest-frame wavelength of the quasar measured on the narrow component (NC) of Hβ. *Lower panel*, fitting results for the bin A3 3000-4000 km s^{-1}. Each plot shows the evaluated χ^2_ν and the wavelength intervals considered in the computation.

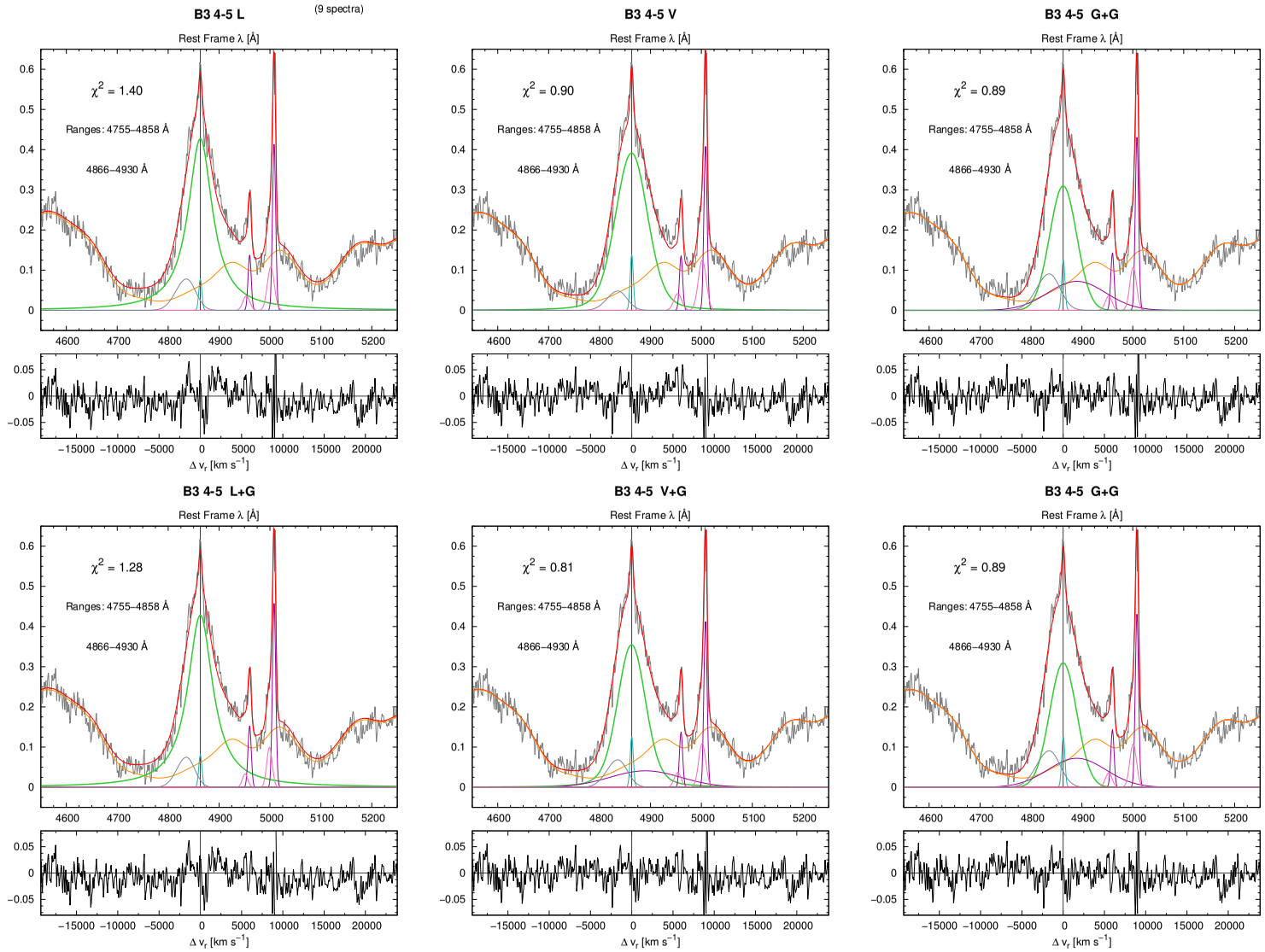

Figure 45: *Upper panel*, continuum subtracted spectra and fitting results for the bin B3 4000-5000 km s^{-1}. The horizontal scale is the rest-frame wavelength (Å) or velocity shift with the origin indicating rest-frame wavelength of the quasar measured on the narrow component (NC) of Hβ. *Lower panel*, fitting results for the bin B3 4000-5000 km s^{-1} for models with VBC. Each plot shows the evaluated χ^2_ν and the wavelength intervals considered in the computation.

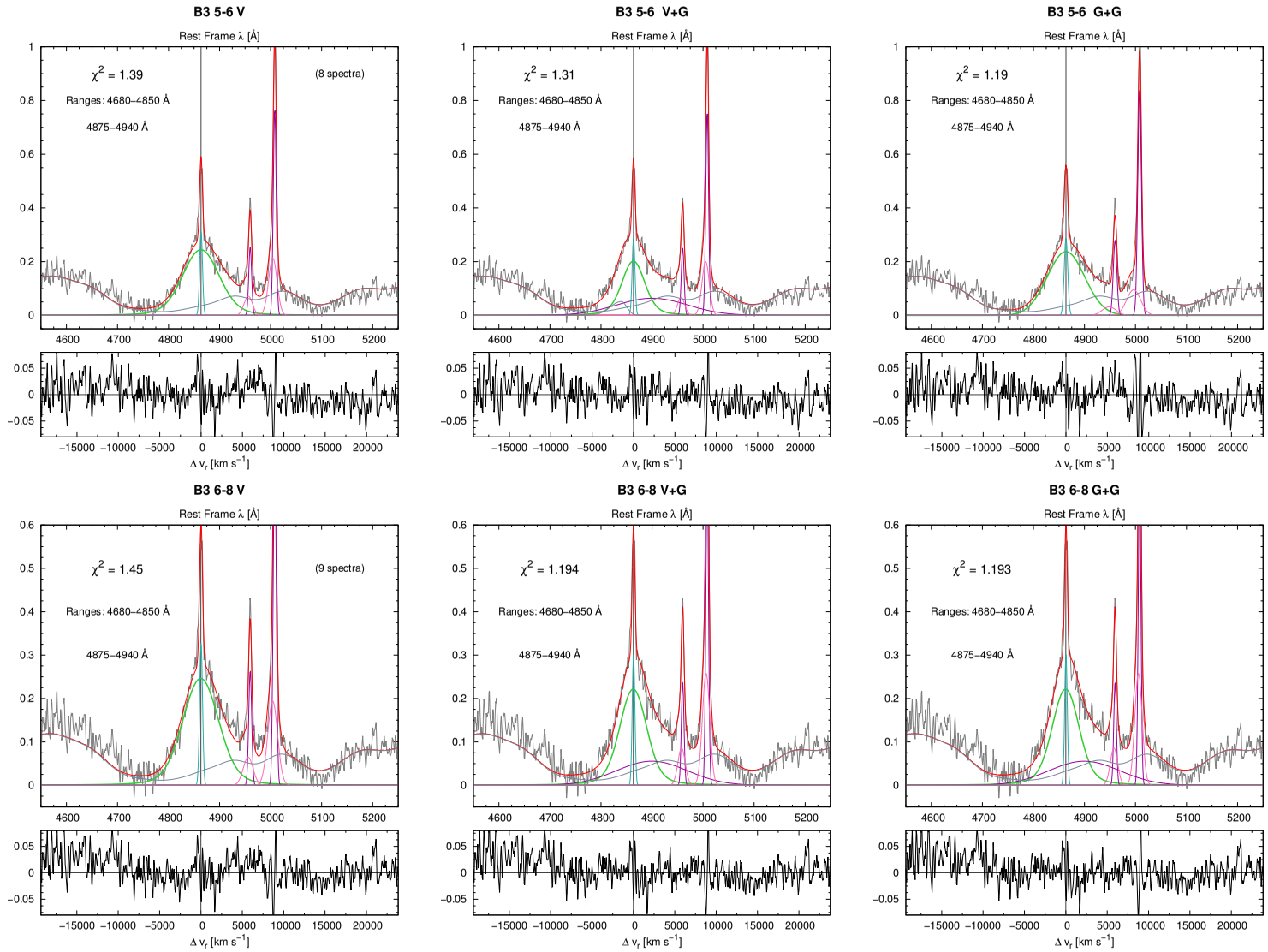

Figure 46: *Upper panel*, continuum subtracted spectra and fitting results for the bin B3 5000-6000 km s^{-1}. The horizontal scale is the rest-frame wavelength (Å) or velocity shift with the origin indicating rest-frame wavelength of the quasar measured on the narrow component (NC) of Hβ. *Lower panel*, fitting results for the bin B3 6000-8000 km s^{-1}. Each plot shows the evaluated χ^2_ν and the wavelength intervals considered in the computation.

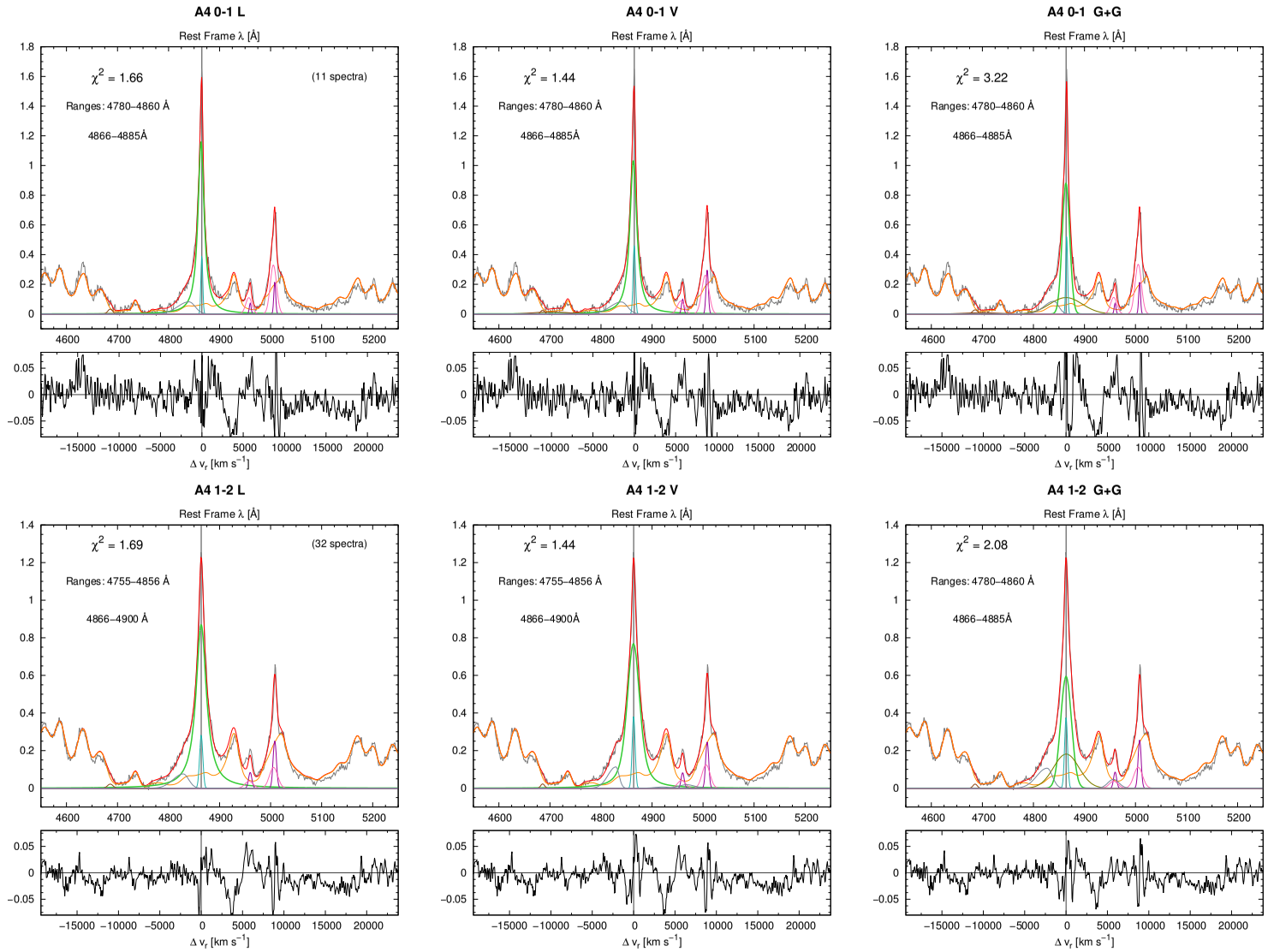

Figure 47: *Upper panel*, continuum subtracted spectra and fitting results for the bin A4 0-1000 km s^{-1}. The horizontal scale is the rest-frame wavelength (Å) or velocity shift with the origin indicating rest-frame wavelength of the quasar measured on the narrow component (NC) of Hβ. *Lower panel*, fitting results for the bin A4 1000-2000 km s^{-1}. Each plot shows the evaluated χ^2_ν and the wavelength intervals considered in the computation.

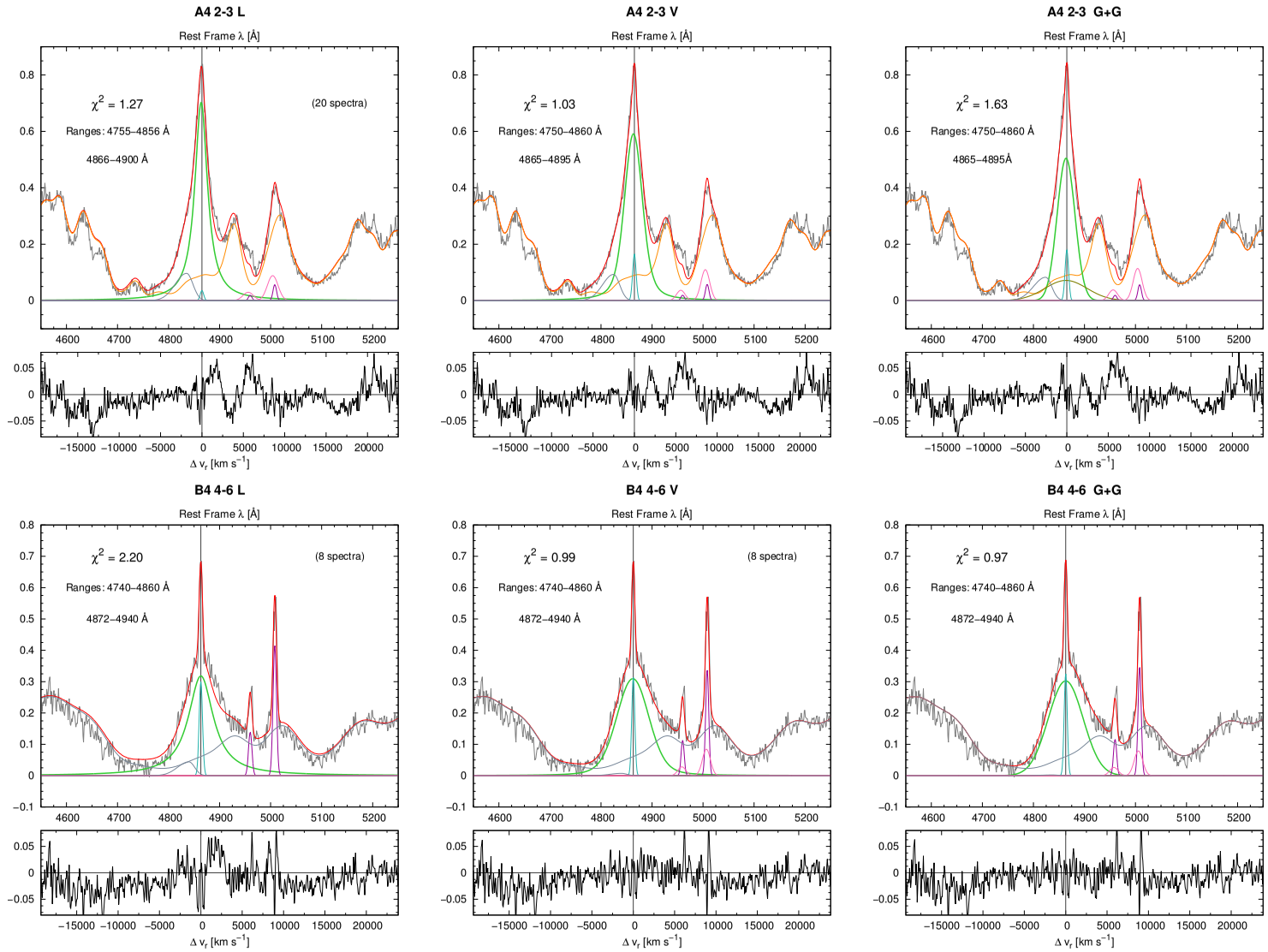

Figure 48: *Upper panel*, continuum subtracted spectra and fitting results for the bin A4 2000-3000 km s^{-1}. The horizontal scale is the rest-frame wavelength (Å) or velocity shift with the origin indicating rest-frame wavelength of the quasar measured on the narrow component (NC) of Hβ. *Lower panel*, fitting results for the bin B4 4000-6000 km s^{-1}. Each plot shows the evaluated χ^2_ν and the wavelength intervals considered in the computation.

List of Figures

List of Tables